Numerical investigation of caisson foundations in sand under combined monotonic loadings for offshore wind turbines

Zhuang Jin

UNIVERSITE BRETAGNE SCIENCES LOIRE POUR L'INGENIEUR

CENTRALE NANTES

THESE DE DOCTORAT DE

L'ÉCOLE CENTRALE DE NANTES
COMUE UNIVERSITE BRETAGNE LOIRE

ECOLE DOCTORALE N° 602
Sciences pour l'Ingénieur
Spécialité : Génie Civil

Par
Zhuang JIN

Numerical investigation of caisson foundations in sand under combined monotonic loadings for offshore wind turbines

Thèse présentée et soutenue à Nantes, le 14/01/2019
Unité de recherche : Institut de Recherche en Génie Civil et Mécanique (GeM)-UMR CNRS 6183

Rapporteurs avant soutenance :

Stéphane GRANGE	Professeur, INSA de Lyon
Mahdia HATTAB	Professeur, Université de Lorraine

Composition du Jury :

Président :	Olivier MILLET	Professeur, Université La Rochelle
Examinateurs :	Olivier MILLET	Professeur, Université La Rochelle
	Frédéric COLLIN	Chargé de Cours, Université de Liège
	Zheng LI	Chargé de Recherche, IFSTTAR
Dir. de thèse :	Panagiotis KOTRONIS	Professeur, Ecole Centrale de Nantes
Co-dir. de thèse :	Zhen-yu YIN	Maitre de Conférences,HDR The Hong Kong Polytechnic University Ecole Centrale de Nantes (adjunct professor)

UNIVERSITE BRETAGNE SCIENCES LOIRE POUR L'INGENIEUR

CENTRALE NANTES

Titre : **Étude numérique des fondations caisson dans du sable sous chargements monotones combinés pour des éoliennes en mer**

Mots clés : *Enveloppe de rupture; diagramme de capacité portante; sable; caisson; élément finis; état critique; macro-élément*

Résumé : Cette thèse de doctorat porte sur la réponse des fondations caisson dans du sable pour les éoliennes en mer soumises à des chargements monotones et cycliques combinés. Le processus de défaillance et l'enveloppe de rupture (diagramme de capacité portante) d'une fondation en caisson dans du sable soumise à des chargements monotones combinés sont premièrement étudiés à l'aide du modèle constitutif de Mohr-Coulomb. La méthode Lagrangian-Smoothed Particle Hydrodynamics Combinée (CLSPH) est adoptée pour prendre en compte les grandes déformations et les limites de l'approche sont mises en évidence. Une loi constitutive basée sur la notion de l'état critique pour le sable récemment mis au point (SIMSAND) est ensuite introduite et utilisée avec la méthode CLSPH. Des tests d'effondrement du sol dans un canal rectangulaire et d'une colonne granulaire en prenant en compte différentes géométries sont simulés afin de valider l'approche en termes de morphologie de dépôt final, des profils d'écoulement et de zones non perturbées.

La méthode CLSPH et le modèle SIMSAND sont ensuite utilisés pour étudier le diagramme de capacité portante des fondations caisson dans du sable. Différents paramètres ayant une incidence sur la forme et la taille de l'enveloppe de rupture sont pris en compte, tels que la densité et la rigidité du sol, la résistance au frottement, la rupture des grains, la géométrie et les dimensions de la fondation. Une formule analytique est introduite pour décrire la surface de rupture 3D capable à reproduire les résultats numériques. Sur la base de la formule analytique proposée, un macro-élément pour des fondations caisson dans du sable soumises à des chargements monotones et cycliques est finalement développé dans le cadre de l'hypoplasticité. L'outil numérique proposé est validé avec des résultats expérimentaux.

Title : **Numerical investigation of caisson foundations in sand under combined monotonic loadings for offshore wind turbines**

Keywords : *Failure envelope; capacity diagram; sand; caisson; finite elements; critical state; macro-element*

Abstract : This PhD thesis deals with the response of caisson foundations in sand for offshore wind turbines submitted to combined monotonic and cyclic loadings. First, the failure process and failure envelope (or bearing capacity diagram) of a caisson foundation in sand under combined monotonic loadings is investigated using the conventional Mohr-Coulomb constitutive model. A Combined Lagrangian-Smoothed Particle Hydrodynamics (CLSPH) method is adopted to consider large deformations and the limitations of the approach are highlighted. A recently developed critical state model for sand (SIMSAND) is then introduced and combined with the CLSPH method. Rectangular channel soil collapse tests and granular column collapse tests considering different aspect ratios are simulated to validate the approach in terms of final deposit morphologies, flow profiles and undisturbed areas.

The CLSPH method and the SIMSAND model are then used to investigate the bearing capacity diagram of the caisson foundation in sand. Different parameters affecting the shape and size of the failure envelope are considered, as soil density and stiffness, friction strength, grain breakage, geometry and aspect ratio of the foundation. An analytical formula is introduced to describe the 3D failure surface reproducing the numerical results. Based on the proposed analytical formula, a macro-element for the caisson foundation in sand submitted to monotonic and cyclic loadings is finally developed within the framework of hypoplasticity. Validation is provided through comparison with experimental results.

Acknowledgements

The author would like to express his deepest thanks to all the people who he worked with during the Ph.D period. Without their help, the research could not be accomplished so smoothly.

Firstly, I would like to give my thanks to China Scholarship Council (CSC). Thanks for providing me the funding during my study and life in France.

Prof. Panagiotis KOTRONIS is my supervisor during the Ph.D study. I am greatly obliged to his continuous help and strong support throughout this research. He did do a lot of effort in improving my knowledge and academic ability in field of geotechnical engineering. His wealth of ideas has enriched this dissertation and highly appreciated.

Prof. Zhenyu YIN is also my supervisor of my Ph.D research. I am extremely grateful to his help these three years, not only in research but also in life. Due to his large experience and knowledge in the field of constitutive modeling and numerical method, he contributed many good ideas for my research. With his efforts and encouragements, my research could be successfully proceeded.

The two supervisors of mine provided me great freedom to let me dive into the sea of research and think freely. Words are not enough to express my gratitude.

I would like to appreciate Mrs. HICHER (Shimu) for her effort to encourage me on learning the language and French culture. She is just like a mentor and a family member. With her fascinating personalities, she made my study and life at Nantes enjoyable and unforgettable.

I also want to express my sincere thanks to Dr Zheng LI and Dr Yinfu JIN. The knowledge and skill I obtained on Finite Element Method, Macroelement modeling and optimization algorithm should owe much to their advice and help.

My thanks are also dedicated to my dear colleagues in ECN: Dr. Qian ZHAO, Dr. Menghuan GUO, Dr. Chaofa ZHAO, Dr. Jiangxin LIU, Dr. Ran ZHU, Jie YANG, Huan WANG. Please forgive me if I omitted someone. Without their companion, the study and life in Nantes could be a little boring and frustrating. Special thanks to Jie YANG who plays tennis with me all the time. Frequent

physical practices help me to have a good health on my research. Sincere thanks to my good neighbor Wenjin CAO, we share a lot of cherished memories these three years.

Last but not least, I want to thank Sci-hub for making a huge amount of literature accessible to me. Without this fantastic website I would have been unable to learn many interesting and important ideas from the research papers written by others. :-)

Finally, kisses to my parents for their selfless loves and supports during my study in France these three years. You are the most important people in my life who give me the greatest motivation to pursue the science and the true meaning of life.

Table of Contents

List of Figures

List of Tables

Abstract

This PhD thesis deals with the response of caisson foundations in sand for offshore wind turbines submitted to combined monotonic and cyclic loadings. First, the failure process and failure envelope (or bearing capacity diagram) of a caisson foundation in sand under combined monotonic loadings is investigated using the conventional Mohr-Coulomb constitutive model. A Combined Lagrangian-Smoothed Particle Hydrodynamics (CLSPH) method is adopted to consider large deformations and the limitations of the approach are highlighted. A recently developed critical state model for sand (SIMSAND) is then introduced and combined with the CLSPH method. Rectangular channel soil collapse tests and granular column collapse tests considering different aspect ratios are simulated to validate the approach in terms of final deposit morphologies, flow profiles and undisturbed areas. The CLSPH method and the SIMSAND model are then used to investigate the bearing capacity diagram of the caisson foundation in sand. Different parameters affecting the shape and size of the failure envelope are considered, as soil density and stiffness, friction strength, grain breakage, geometry and aspect ratio of the foundation. An analytical formula is introduced to describe the 3D failure surface reproducing the numerical results. Based on the proposed analytical formula, a macro-element for the caisson foundation in sand submitted to monotonic and cyclic loadings is finally developed within the framework of hypoplasticity. Validation is provided through comparison with experimental results.

Keywords: Failure envelope; capacity diagram; sand; caisson; finite elements; critical state; macro-element

Résumé

Cette thèse de doctorat porte sur la réponse des fondations caisson dans du sable pour les éoliennes en mer soumises à des chargements monotones et cycliquescombinés. Le processus de défaillance et l'enveloppe de rupture (diagramme de capacité portante) d'une fondation en caisson dans du sable soumise à des chargements monotones combinés sont premièrement étudiés à l'aide du modèle constitutif de Mohr-Coulomb. La méthode Lagrangian-Smoothed Particle Hydrodynamics Combinée (CLSPH) est adoptée pour prendre en compte les grandes déformations et les limites de l'approche sont mises en évidence. Une loi constitutive basée sur la notion de l'état critique pour le sable récemment mis au point (SIMSAND) est ensuite introduite et utilisée avec la méthode CLSPH. Des tests d'effondrement du sol dans un canal rectangulaire et d'une colonne granulaire en prenant en compte différentes géométries sont simulés afin de valider l'approche en termes de morphologie de dépôt final, des profils d'écoulement et de zones non perturbées. La méthode CLSPH et le modèle SIMSAND sont ensuite utilisés pour étudier le diagramme de capacité portante des fondations caisson dans du sable. Différents paramètres ayant une incidence sur la forme et la taille de l'enveloppe de rupture sont pris en compte, tels que la densité et la rigidité du sol, la résistance au frottement, la rupture des grains, la géométrie et les dimensions de la fondation. Une formule analytique est introduite pour décrire la surface de rupture 3D capable à reproduire les résultats numériques. Sur la base de la formule analytique proposée, un macro-élément pour des fondations caisson dans du sable soumises à des chargements monotones et cycliques est finalement développé dans le cadre de l'hypoplasticité. L'outil numérique proposé est validé avec des résultats expérimentaux.

Mots-clés : Enveloppe de rupture; diagramme de capacité portante; sable; caisson; élément finis; état critique; macro-élément

General introduction

A caisson is a closed-top steel tube, which lowered to the seafloor allows bottom sediments to penetrate under its own weight. When pushed to full depth with suction force produced by pumping water out of its interior, the caisson foundation is also called suction bucket foundation. The main advantages of caissons are the convenient method of installation, their repeatedly use and the fact that they may mobilize a significant amount of passive suction during uplift. Recently, caissons have been widely used for different types of constructions, such as gravity platform jackets, jack-ups, offshore wind turbines, subsea systems and seabed protection structures. For an optimum design, understanding the nonlinear behavior of caisson foundations and developing specific fast and robust numerical tools is therefore necessary. The thesis is divided into six chapters outlined as follows:

Chapter 1 contains a literature review. Existing experimental and numerical studies on the behaviour of caisson foundations subjected to complex loadings are presented. Although the bearing capacity characteristics have been numerically extensively studied, several limitations however still remain. It is important to use a numerical method that accurately reproduces large deformations during extreme loading conditions (such as during the caisson installation phase). Furthermore, advanced constitutive models are necessary to obtain reliable responses under combined loadings.

In chapter 2, the failure process and failure mode of a caisson foundation in sand are investigated by numerical modelling using the Mohr-Coulomb constitutive law. As the evolving failure happens under large deformations, a Combined Lagrangian - Smoothed Particle Hydrodynamics method (CLSPH) is adopted. The method is first calibrated and validated by simulating a sand cone penetration test (CPT). Then, an experimental campaign of a caisson in the same sand is used to validate the numerical model. Caisson foundations with different dimensions submitted to representative combined loading paths are then simulated and the influence of their dimensions to the failure process and failure mode is investigated.

In chapter 3, a critical state constitutive law (SIMSAND) accounting for soil density effects is adopted and implemented combined with the CLSPH method. Rectangular channel soil collapse and granular column collapse tests with different aspect ratios are simulated to validate the numerical tool in terms of final deposit morphologies, flowing profiles and undisturbed areas. Additional simulations for different void ratios are conducted to investigate the effect of soil density on the final deposit morphology and to further validate the CLSPH – SIMSAND model.

In chapter 4, the validated CLSPH – SIMSAND model is used to model the failure envelope (the bearing capacity diagram) of a caisson foundation in sand. The soil parameters of the SIMSAND model are calibrated using a series of triaxial tests on Baskarp sand. Validation is provided with Baskarp sand cone penetration tests. A series of model tests of a caisson foundation in Baskarp sand and field tests are also simulated. An important number of finite element numerical calculations are then performed to reproduce the behavior of a caisson foundation subjected to complex loading combinations. In order to investigate the failure envelope in the *H-M-V* space (i.e. horizontal force H, bending moment M, vertical force *V*), the radial displacement method is chosen. Several factors are considered affecting the shape and size of the failure envelope as soil density, friction strength, soil stiffness, grain breakage effect, geometry size and aspect ratio. The coupling relationship among geometry size, aspect ratio and characteristic parameters of the failure envelope is considered and quantified with an equation. Finally, an analytical formula presenting good consistency with the numerical results is introduced to describe the 3D failure surface of a caisson foundation in sand submitted to combined loadings.

Chapter 5 proposes a novel macroelement to reproduce the response of a caisson foundation in sand under complex monotonic and cyclic loadings. Developed in the framework of continuum hypoplasticity, the macroelement simulates the cyclic response using a displacement-like vector internal variable. The calibration procedure is detailed and finally a series of monotonic and cyclic tests show the performance of this novel numerical tool.

Chapter 6 presents the general conclusions and perspectives of this work.

Introduction générale

Un caisson est un tube en acier à sommet fermé qui, descendu jusqu'au fond de la mer, permet aux sédiments du fond de pénétrer sous son propre poids. Lorsque poussée à fond avec la force d'aspiration produite par le pompage de l'eau, la fondation de caisson est également appelée caisson à succion. Les principaux avantages des caissons sont leur méthode d'installation pratique, leur utilisation répétée et le fait qu'ils peuvent mobiliser une quantité importante d'aspiration passive pendant le soulèvement. Récemment, les caissons ont été largement utilisés pour différents types de construction, tels que les fondations gravitaires, les ponts élévateurs, les éoliennes offshore, les systèmes sous-marins et les structures de protection des fonds marins. Pour une conception optimale, il est donc nécessaire de comprendre le comportement non linéaire des fondations de caissons et de développer des outils numériques spécifiques rapides et robustes. La thèse est divisée en six chapitres décrits comme suit :

Le chapitre 1 contient une revue de la littérature. Des études expérimentales et numériques existantes sur le comportement de fondations en caisson soumises à des chargements complexes sont présentées. Bien que les caractéristiques de capacité portante aient été étudiées numériquement de manière approfondie, il subsiste néanmoins plusieurs limitations. Il est important d'utiliser une méthode numérique qui reproduit avec précision les grandes déformations lors de conditions de chargement extrêmes (comme lors de la phase d'installation du caisson). De plus, des modèles constitutifs avancés sont nécessaires pour obtenir des réponses fiables sous des chargements combinés.

Au chapitre 2, le processus de rupture et le mode de rupture d'une fondation en caisson en sable sont étudiés par modélisation numérique à l'aide de la loi de comportement de Mohr-Coulomb. Comme la rupture évolutive se produit sous de grandes déformations, la méthode Lagrangian - Smoothed Particle Hydrodynamics method (CLSPH) est adoptée. La méthode est d'abord calibrée et validée en simulant un test de pénétration au cône de sable (CPT). Ensuite, une campagne expérimentale d'un caisson dans le même sable est utilisée pour valider le modèle numérique. Des fondations de caissons de différentes dimensions soumises à des chemins de chargement combinés représentatifs sont ensuite simulées et l’influence de leurs dimensions sur le processus et le mode de rupture est étudiée.

Au chapitre 3, une loi constitutive basée sur la notion de l’état critique (SIMSAND) prenant en compte les effets de la densité du sol, est adoptée et mis en œuvre avec méthode CLSPH. Des tests

d’effondrement des canaux rectangulaires et de colonnes granulaires avec différentes dimensions sont simulés pour valider l’outil numérique en termes de morphologie de dépôt finale, de l’écoulement et de zones non perturbées. Des simulations supplémentaires pour différents taux de vide sont réalisées afin d'étudier l'effet de la densité du sol sur la morphologie du dépôt final et de valider davantage le modèle CLSPH-SIMSAND.

Au chapitre 4, le modèle CLSPH - SIMSAND validé est utilisé pour modéliser l'enveloppe de rupture (le diagramme de capacité portante) d'une fondation en caisson dans du sable. Les paramètres de sol du modèle SIMSAND sont calibrés à l'aide d'une série d'essais triaxiaux sur le sable de Baskarp. La validation est fournie avec des tests de pénétration au cône de sable Baskarp. Une série d'essais sur modèle d'une fondation de caisson dans du sable de Baskarp et des essais sur le terrain sont également simulés. Un nombre important de calculs numériques par éléments finis est ensuite effectué pour reproduire le comportement d’une fondation en caisson soumise à des combinaisons de chargement complexes. Pour étudier l'enveloppe de rupture dans l'espace H-M-V (c'est-à-dire la force horizontale H, le moment de flexion M, la force verticale V), la méthode du déplacement radial est choisie. Plusieurs facteurs sont considérés comme ayant une incidence sur la forme et la taille de l'enveloppe de rupture, tels que la densité du sol, la résistance au frottement, la rigidité du sol, la rupture des grains, la géométrie et le rapport des dimensions. Le couplage entre la géométrie, le rapport des dimensions et les paramètres caractéristiques de l’enveloppe de rupture est considéré et quantifié à l’aide d’une équation. Enfin, une formule analytique présentant une bonne cohérence avec les résultats numériques est introduite pour décrire la surface de rupture 3D d'une fondation en caisson dans du sable soumis à des chargements combinés.

Le chapitre 5 propose un nouvel macroélément permettant de reproduire la réponse d’une fondation à caisson dans du sable soumis à des chargements complexes monotones et cycliques. Développé dans le cadre de l'hypoplasticité, le macroélément simule la réponse cyclique à l'aide d'une variable interne vectorielle de type déplacement. La procédure de calibration est détaillée et enfin une série de tests monotones et cycliques montrent les performances de ce nouvel outil numérique.

Le chapitre 6 présente les conclusions générales et les perspectives de ce travail.

Chapter 1 Literature review

1.1 Introduction

Energy crises, air pollution and the greenhouse effect have increasingly become noteworthy environmental issues. To solve these problems, offshore wind energy, among other possibilities such as solar and tidal energy, is attracting ever more attention. Moreover, wind energy has been the first commercial renewable energy to be developed in a major way. In general, a large-diameter monopile and gravity-based foundation act as foundations for offshore wind turbines (Sørensen and Sørensen 2010). Gravity-based foundations are preferable only if the depth of seabed is within 5m, while pile foundations are typically used in a water depth of less than 20m. Moreover, the two types of foundations cannot be removed easily when they reach the end of their service lives. Suction caisson foundations, however, can solve these problems effectively.

A caisson is a closed-top steel tube, which is first lowered to the seafloor, allowing bottom sediments to penetrate under its own weight, and then pushed to full depth with suction force produced by pumping water out of its interior. The main advantages of caissons include suitability in various seabed depths, convenient method of installation, repeated use and the fact that they may mobilize a significant amount of passive suction during uplift (Zhang et al. 2013). Caisson foundations are usually subjected to vertical loading with long-period horizontal loading or cyclic loading components including horizontal loadings and moments. The vertical loading V, the horizontal loading H and the moment M can be transferred to the foundation through the footing beneath the building. Such a loading mode is defined as a combined loading mode as shown in Figure 1.1.

For an optimum design, understanding the performance of caisson foundations is necessary. At the present time, much literature has been published regarding the investigation of the response of foundations subjected to general combined monotonic/cyclic loadings. In this chapter, existing experimental and numerical studies for investigating the bearing capacity characteristics of caisson foundations are reviewed. It is noteworthy that the literature survey mainly focuses on the investigation of caisson foundations in sand, the research topic of this dissertation.

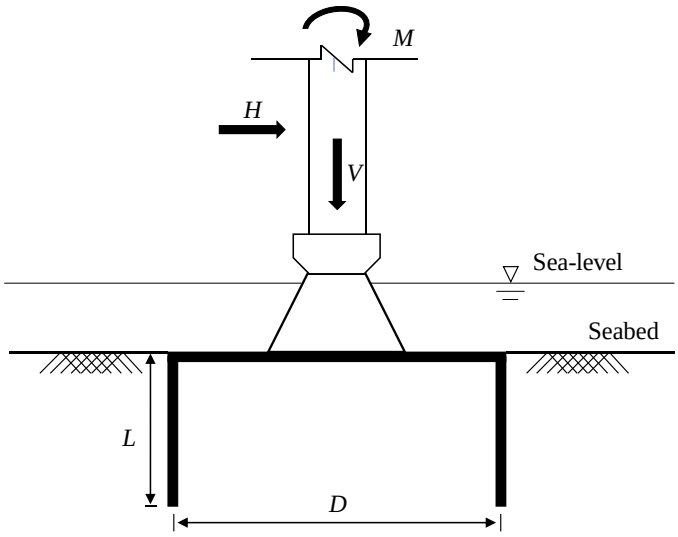

Figure 1.1 Schematic plot of a caisson foundation for offshore wind turbines

1.2 Experimental studies on caisson foundations

In this section, a short literature review is presented to discuss experimental studies on caisson foundations in sand. The contents are divided into three groups: field tests (or in-situ tests), conventional laboratory tests and centrifuge tests.

1.2.1 Prototype and reduced-scale field tests

Several studies have published data from large-scale and reduced scale field tests of caisson foundations (Hogervorst 1980; Tjelta et al. 1986; Tjelta 1994; Houlsby et al. 2006; Kelly et al. 2006). Table 1.1 presents an outline of the related field tests. The main research purpose was to obtain a good understanding of the site conditions.

Table 1.1 Historical sequence of recorded scale field testing of caisson foundations in sand

Site	Soil	Caisson size		Reference
		Diameter (m)	Depth (m)	
The North sea	Sand over clay	3.8	5-10	Hogervorst (1980)
The North sea	Layers of sand and clay	6.5	22	Tjelta et al. (1986)
The North sea	Sand	12	6	Tjelta (1994)
Frederikshavn	Sand	2	2	Houlsby et al. (2005)
Luce Bay	Sand	3	1.5	Houlsby et al. (2006)
		1.5	1	

Hogervorst (1980) carried out a field test in the North Sea considering the suction pile (see Figure 1.2(a)) at different inshore locations, two with sandy soils and one with hard clay (see Figure 1.2(b)). Piles of 3.8m diameter and between 5 and 10m length were tested in order to determine their installation characteristics, lateral and axial load capacities. After comparative studies, it was concluded that in shallow water, a suction pile was competitive even with embedment anchors. The suction anchor pile can thus be expected to offer distinct advantages over conventionally driven-in or drilled-in piles.

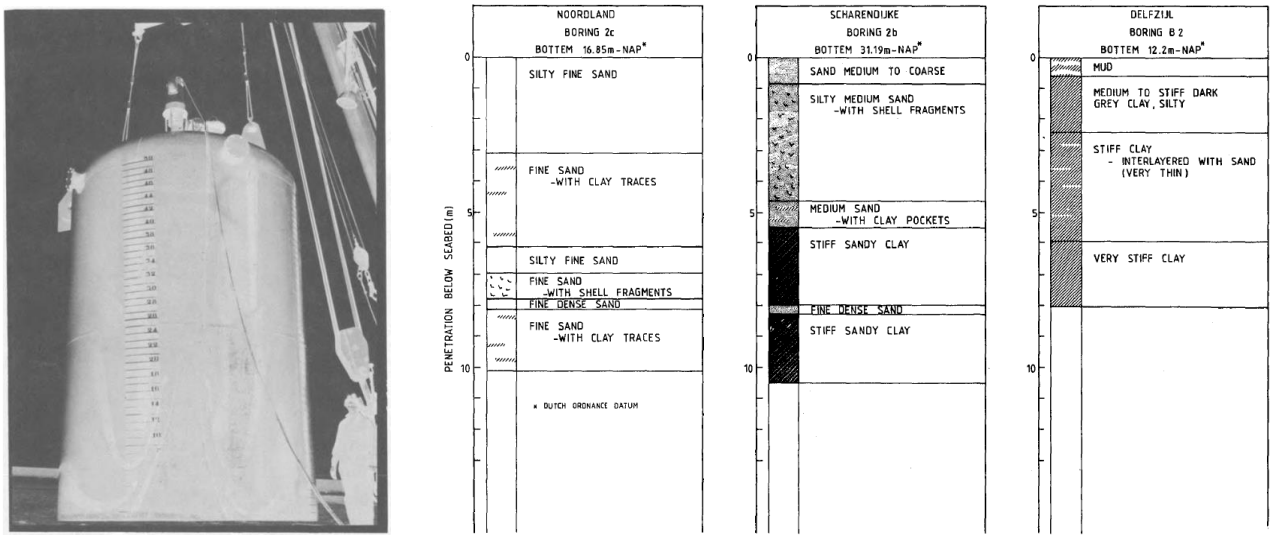

(a) (b)

Figure 1.2 (a) Suction anchor pile (b) Soil profiles of test sites

Tjelta et al. (1986) conducted field tests in 1985 in the North Sea of a detailed design of the Gullfaks C gravity base structure (see Figure 1.3(a)). It was necessary to determine the feasibility of using self-weight and suction to install the 22-meter skirt foundation into layered soil (see Figure 1.3 (b)). Tests were conducted successfully and included checking changes in permeability and resistance, the effects of soil organization on installation, several cycle loading tests and a new water injection system to reduce tip resistance. Test results confirmed the possibility of installing a large skirt structure that provided a 22-meter skirt for the Gullfaks C gravity infrastructure.

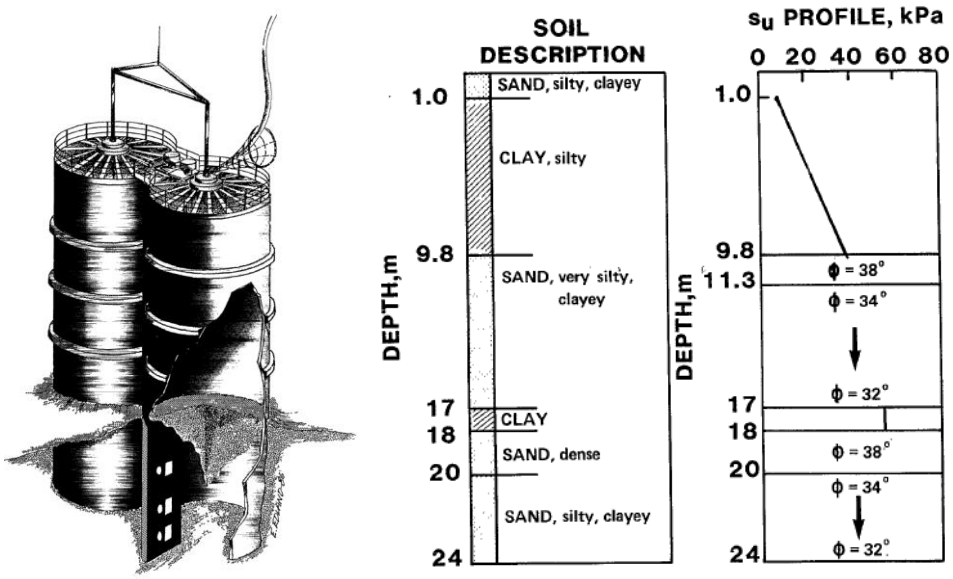

(a) (b)

Figure 1.3 (a) General view of the tested structure (b) Summary of soil conditions

Tjelta (1994) conducted field tests in 1994 for the Europipe 16/11-E riser platform (see Figure 1.4(a)) in the North Sea. The foundation consisted of a 12m diameter and 6m depth bucket at each of the 4 corner legs. The availability of uplift capacity in sand (see Figure 1.4(b)) and the possibility of skirt penetrated to a specified depth were considered. The results indicated that the penetration of steel skirt in dense sand was feasible with only small weight when using suction. Additionally, pull-out capacity was not critical for design.

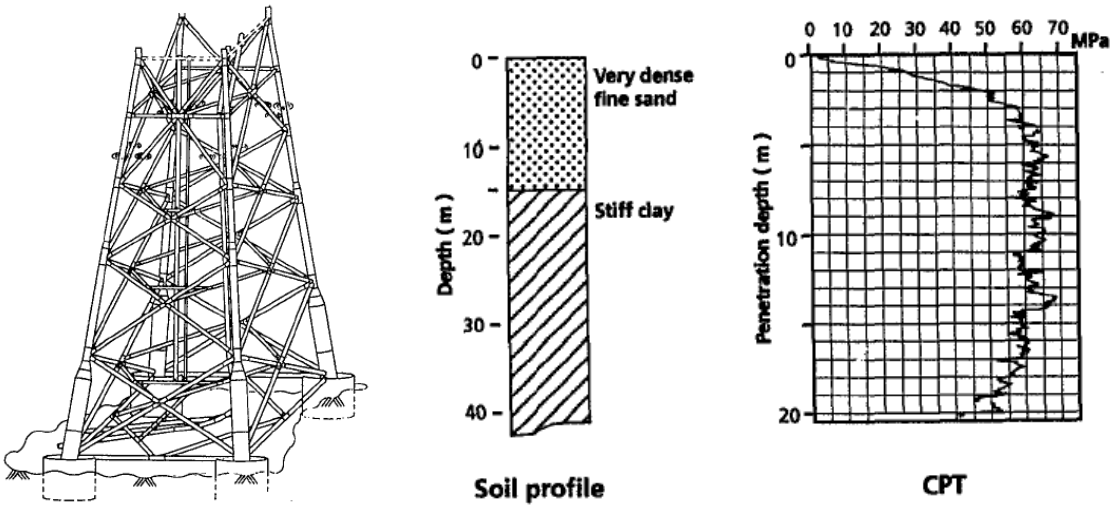

(a) (b)

Figure 1.4 (a) Eurpipe 16/11-E riser platform (b) Summary of soil conditions

Houlsby et al. (2005) conducted a large-scale test at Frederikshavn in 2004, which employed loading by applying a horizontal load at a fixed height. A steel caisson with an outer diameter of 2m and a skirt length of 2m was used (see Figure 1.5(a)). This field test involved the instrumented Vestas V90 3.0 MW prototype turbine installed in 2002 at Frederikshavn, Denmark (see Figure 1.5(b)). In the same year, Houlsby et al. (2006) carried out a series of field trials on suction caisson foundations in an artificially prepared sand test bed near Luce Bay. A caisson of diameter 3m and with a skirt 1.5m deep was used for moment loading tests; a second caisson of diameter 1.5m and with a 1m skirt was used for vertical loading tests. An outline diagram of the test setup is provided in Figure 1.6(a), and the testing rig at Luce Bay location is shown in Figure 1.6(b). The investigations involved the suction installation of the caissons, cyclic moment loading under both quasi-static and dynamic conditions to simulate the behaviour of a monopod foundation and cyclic vertical loading and pullout of caissons to simulate one footing in a quadruped foundation. High-frequency, low-amplitude cyclic moment tests showed that the response was affected by stiffness as well as inertial and damping effects. Cyclic vertical loading tests showed a reduction of stiffness and increase of hysteresis as load amplitude increased. The pull-out tests indicated that a sizeable ultimate tensile resistance could be generated.

(a) (b)

Figure 1.5 (a) A large scale caisson (2×2m) for field test (b) A prototype caisson foundation (12×6m) at the test site in Frederikshavn

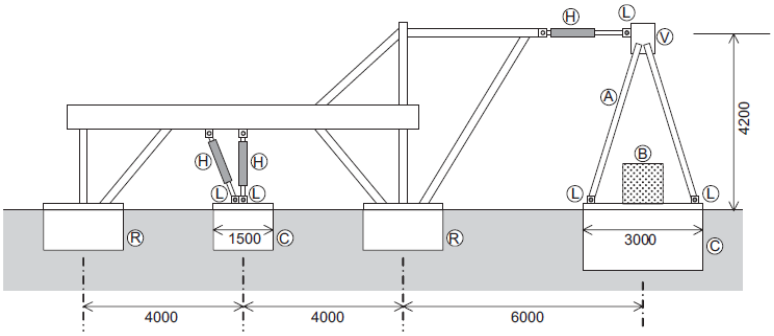

(a)

(b)

Figure 1.6 (a) Outline of field test equipment (dimensions in mm) (b) Test rig at the Luce Bay

1.2.2 1-g model test on reduced scale

The considerable cost and time-consuming nature of prototype tests or field trials on reduced scales mean that the study of the bearing capacity of actual-size equipment has limited utility. The modification of soil parameters is much easier in small-scale tests. In addition, the soil type and the caisson geometry can be varied in such cases. Owing to the advantage of model tests, many 1-g small-scale model tests have been conducted to study the bearing capacities of caisson foundations in dry, dense sands under varying embedment ratios and vertical loadings (Byrne and Houlsby 1999; Byrne 2000; Byrne and Houlsby 2003; Villalobos Jara 2006; Villalobos et al. 2009). Table 1.2 shows various model tests on a reduced scale for caisson foundations in dry sand and saturated sand.

Table 1.2 Historical sequence of 1-g model tests on reduced scale for caisson foundation in sand

Site	Soil	Caisson size		Ref.
		D (mm)	L (mm)	
Oxford University	Dry sand	100	0, 16, 33, 66	Byrne and Houlsby (1999) Byrne (2000)
	Dry sand	293	146.5	Villalobos et al. (2005) Villalobos et al. (2009)
		203.4	203.5	
	Saturated sand	293	146.5	Byrne and Houlsby (1999)
		200	100	
Aalborg University	Saturated sand	200	0, 50, 100, 150, 200	Larsen et al. (2013) Ibsen et al. (2013; 2014; 2015)
		300	0, 75, 150, 225, 300	

Byrne and Houlsby (1999) conducted a series of 1-g model tests that focused on a caisson foundation with a caisson diameter of 100 mm and four embedment ratios (0, 0.16, 0.33 and 0.66) on a sand of 95% relative density (marked as Baskarp Cyclone Sand, the particle distribution of test sand presented in Figure 1.7(a)) at Oxford University by adopting a three-degree-of-freedom testing rig (see Figure 1.7(b)). The tests concentrated primarily on the plastic deformations; the behaviour within the yield surface was also examined. The authors found that the yield surface of caisson foundations in (*V: M/2R: H*) space could be well-described by a parabolic ellipsoid. The study indicated that the shape of yield surface varied with increasing embedment ratio.

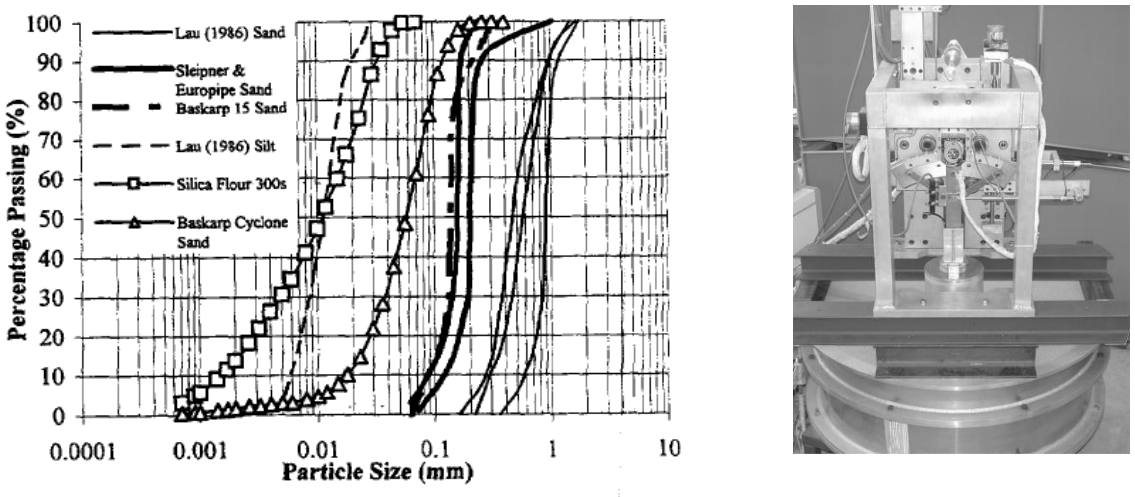

(a) (b)

Figure 1.7 (a) Particle size distribution of sand in experiments (b) Three-degree-of-freedom testing rig at Oxford University

Villalobos et al. (2009) carried out numerous model tests for a caisson foundation on dry sand at a low relative density (marked as white 14/25 Leighton Buzzard sand). The testing was conducted

using the same three-degree-of-freedom loading rig at Oxford University as shown in Figure 1.7(b). Two model foundations were used, one marked as A with diameter of 293mm and skirt length of 146.5mm, the other marked as B with diameter of 203.4mm and skirt length of 203.5mm. The experiments were successfully interpreted within the framework of work-hardening plasticity, and the shape of the yield surface and the post-yield behaviour of the caisson foundation were deduced. A key result from this work was that the caisson could mobilize a moment and/or horizontal resistance under tensile loads. These works successfully investigated the failure of a caisson foundation under multidirectional loading conditions.

Compared with the researches concentrating on dry sand, investigations on saturated sand might be more practical in guiding the design of a caisson foundation. Therefore, the literature review also considered several research works that were focused on the failure of a caisson foundation in saturated sand (Villalobos et al. 2005; Ibsen et al. 2013; Larsen et al. 2013; Ibsen et al. 2014; Ibsen et al. 2015; Li et al. 2015).

Villalobos et al. (2005) carried out a series of moment capacity tests at model scale to investigate the effects of different installation procedures (by bushing or by using suction) on the response of a suction caisson foundation in saturated sand (marked as Redhill 110). Tests were performed using the three-degree-of-freedom loading rig (3DOF) mentioned above (see Figure 1.7(b)). Two caissons of different diameters (D_1=293mm, D_2=200mm) and wall thicknesses (t_1=3.4mm, t_2=1.0mm) but similar skirt length to diameter ratio (L_1=146.5mm, L_2=100mm) were adopted. The comparative tests indicated that the moment resistance of a suction caisson depended on the installation method. Under rotation, more vertical uplift was observed for the pushed-installed caisson than for the suction-installed caisson. Moreover, the use of suction beneficially reduced the resistance to penetration of the caisson.

Researchers of Aalborg University (Ibsen et al. 2013; Larsen et al. 2013; Ibsen et al. 2014; Ibsen et al. 2015) conducted an extensive number of loading tests with small-scale caisson foundations subjected to combined loading. Tests were performed on caissons of various sizes, embedment ratios and loading paths on saturated dense Aalborg University Sand No. 1. The grading curve is shown in Figure 1.8, and the strength values of Aalborg University Sand No. 1 are summarized in Table 1.3 for void ratios of 0.55, 0.61, 0.7 and 0.85.

Table 1.3 Values of strength parameters for the Aalborg University Sand No. 1

Void ratio e	*Friction angle* φ (∘)	*Cohesion* c (kPa)
0.55	41	19.9
0.61	38.6	34.57
0.7	34.21	40.27
0.85	30.93	7

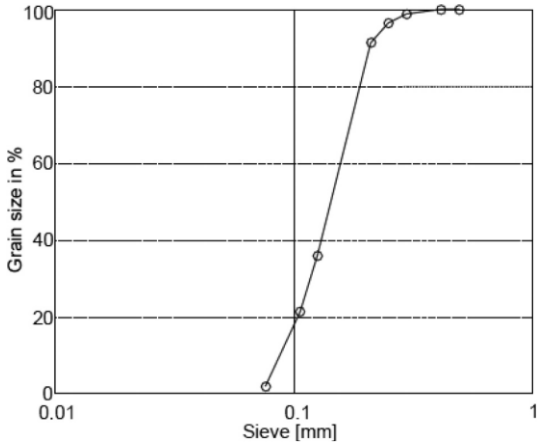

Figure 1.8 Particle size distribution of the Aalborg University Sand No. 1

Figure 1.9 presents the loading setup designed at Aalborg University for a caisson foundation. For the loading phase, a specified vertical loading was applied first. Then a moment and horizontal force were applied to the caisson foundation until failure was achieved. The diameter of the caisson was kept constant (D_1=200mm, D_2=300mm), and the length of skirt varied using embedment ratios (i.e. ratio) of 0, 0.25, 0.5, 0.75 and 1. The load path given by *M/DH* varied between 0.37 and 8.7, corresponding to loads from waves and winds respectively. Based on the data from small-scale tests on caisson foundations subjected to static loads, the shape of the yield, potential and failure surfaces were found to be dependent on the embedment ratio and load path. A similar conclusion was found for the failure surface of a caisson foundation under general combined loadings, primarily depending on the embedment ratio and the applied vertical loading. The size of the failure envelopes increased with the increase of the embedment ratio and specified vertical loading. A formula was proposed to describe the capacity of caisson foundations for combined loading by calibrating the failure criteria of bucket foundations.

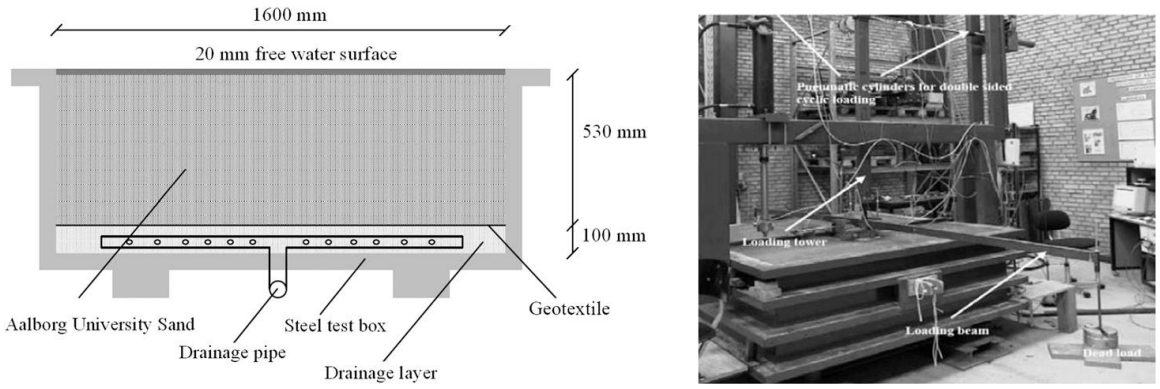

(a) (b)

Figure 1.9 (a) Geometry of the test setup, (b) Loading setup designed at Aalborg University for a caisson foundation

1.2.3 Centrifuge tests

It bears mentioning that small-scale tests present some drawbacks. Soil behaviour is stress-dependent. Small-scale models and prototypes cannot withstand the same stress level and therefore they do not exhibit identical responses. Data and conclusions from model tests should be used with caution to predict field behaviour. In order to overcome these difficulties, geotechnical centrifuge devices have been developed and adopted to reproduce the actual stress level of a prototype in small-scale tests. The results of centrifuge tests can be scaled up to the size of full-scale caissons.

Historically, several researches investigated the static or/and dynamic response of a suction pile (Fuglsang and Steensen-Bach 1991; Renzi et al. 1991; Allersma et al. 1997; Allersma et al. 1999; Zhang et al. 2003; Raines and Garnier 2004; Kim et al. 2005) or caisson (Clukey and Morrison 1993; Clukey et al. 1995; Watson and Randolph 1997; Cao 2003; Yun and Bransby 2003; Cassidy et al. 2004; Lu et al. 2007; Zhang et al. 2007; Kim et al. 2014) under general combined loadings by centrifuge tests. Table 1.4 displays the historical recorded researches on centrifuge model tests for suction pile and caisson foundations.

Table 1.4 Historical sequence of centrifuge model tests for suction pile and caisson foundation

Soil type	Model size		Prototype size		Acceleration	Reference
	D (mm)	*L* (mm)	*D* (m)	*L*(m)	(g=9.8m/s^2)	
Clay	152.5	356.9	15.25	35.69	100	Clukey et al. (1995)
Saturated sand	39	75	5.9	11.3	150	Allersma et al. (1997)
	63.2	60	9.5	9.0		
	25.2	108	3.8	16.2		

	69	61	10.4	9.2		
Calcareous silt	80	32	12	4.8	150	Watson and Randolph (1997)
Clay	30	70	4.5	10.5	150	Allersma et al. (1999)
Clay	28.7	245	2.87	24.5	100	Cao (2003)
	51.7	245	5.17	24.5		
	103.4	245	10.34	24.5		
Dry sand	100	20	10	2	100	Yun and Bransby (2003)
Clay	60	30	6	3	100	Cassidy et al. (2004)
Clay	64	300	6.4	30	100	Raines and Garnier (2004)
Dry sand	30	50	1.5	2.5	50	Kim et al. (2005)
Saturated sand	6	7.2	/	/	10, 20, 40, 60	Lu et al. (2007)
	6	4.8			40	
	6	9			60	
Silt (with 3.2% clay)	60	72	4.8	5.76	80	Zhang et al. (2007)
	60	90	4.8	7.2		
	60	48	4.8	3.84		
Layer of silty sand	92.9	114.3	6.5	8.0	70	Kim et al. (2014)
Layer of sandy silt	221.4	150	15.5	10.5		

Most of the above-mentioned studies focused on clay, only few researches conducted centrifuge tests in sand. More specifically, a test program was carried out using the small geotechnical centrifuge of the Delft University of Technology to investigate the installation of suction piles in sand (Allersma et al. 1997). Figure 1.10 shows the geotechnical centrifuge at the Delft University of Technology. All tests were carried out in homogeneous sand layers. In order to reduce the particle-size effect, sand with a small grain size was used. The main characteristics of this sand are displayed in Table 1.5. The tests were performed at an acceleration of n=150g. The model size and corresponding prototype size are shown in Table 1.4. The installation phase of a suction pile was investigated by measuring the displacements and pressures during the installation. The results indicated a linear relationship between the pressure and the dimensions of the suction pile. The penetration load during suction was approximately 8 times smaller than during mechanical penetration.

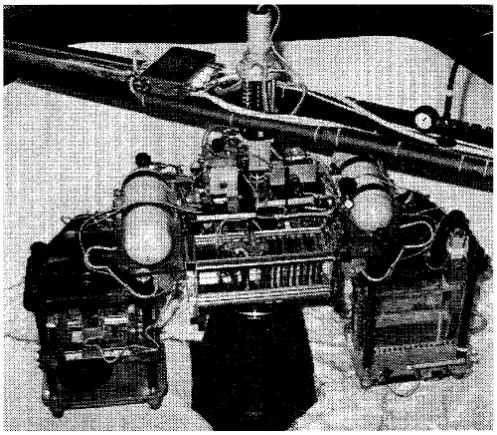

Figure 1.10 Geotechnical centrifuge at the Delft University of Technology

Table 1.5 Properties of the sand used in experiments

d_{90} (mm)	0.140	Specific gravity G_s	2.65
d_{60} (mm)	0.109	Minimum dry unit weight $\gamma_{d,min}$ (kN/m^3)	12.32
d_{50} (mm)	0.102	Maximum dry unit weight $\gamma_{d,max}$ (kN/m^3)	16.06
d_{10} (mm)	0.068	Coefficient of uniformity CU=d_{60}/d_{10}	1.62

Yun and Bransby (2003) presented the combined vertical, horizontal and moment loading response of a caisson foundation on drained loose sand (a mean density of 1540kg/m^3) by conducting numerous centrifuge tests in the University of Dundee Geotechnical Centrifuge. The model foundations tests were all performed at 100 times earth's gravity. The diameter of 10m and skirt length of 2m in the prototype correspond to a diameter of 10mm and skirt length of 2mm in the model scale. Figure 1.11 presents a photograph and cross-section of the centrifuge testing apparatus. The foundation soil was a poorly graded sand with D_{50}=0.22 mm and D_{10}=0.16 mm. The angle of friction φ=31° and dilation angle ψ=0° were based on direct shear box tests. The test results showed that the horizontal capacity of the skirted foundation was increased to about 3-4 times that of a raft foundation because of the skirts, even in drained conditions. It was also suggested that the foundation failure mechanism changed to a rotational mode instead of a sliding mechanism.

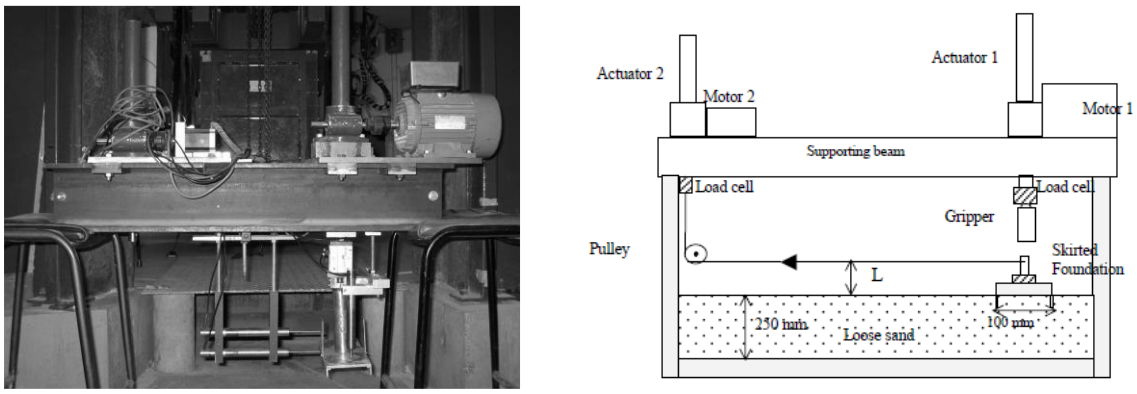

(a) (b)

Figure 1.11 (a) Photograph of part of the centrifuge testing apparatus (b) Cross-section of the test apparatus

Lu et al. (2007) conducted a series of centrifuge experiments to study the response of caisson foundations under horizontal and vertical dynamic loadings by using the 50g-ton centrifuge at Tsinghua University (see in Figure 1.12). The applied centrifuge acceleration in the test program is displayed in Table 1.4. The experimental material was fine sand with special gravity 2.69 and average grain diameter (D_{50}) 0.014cm. It was shown that when the loading amplitude was over a critical value, the sand at the upper part around the bucket was softened or even liquefied. The excess pore pressure decreased from the upper part to the lower part of the sand layer in the vertical direction and decreased radially from the bucket's side wall in the horizontal direction. Significant settlement of the bucket and the sand layer around the bucket was induced by dynamic loading. The dynamic response of the bucket with smaller height (the same diameter) was more obvious.

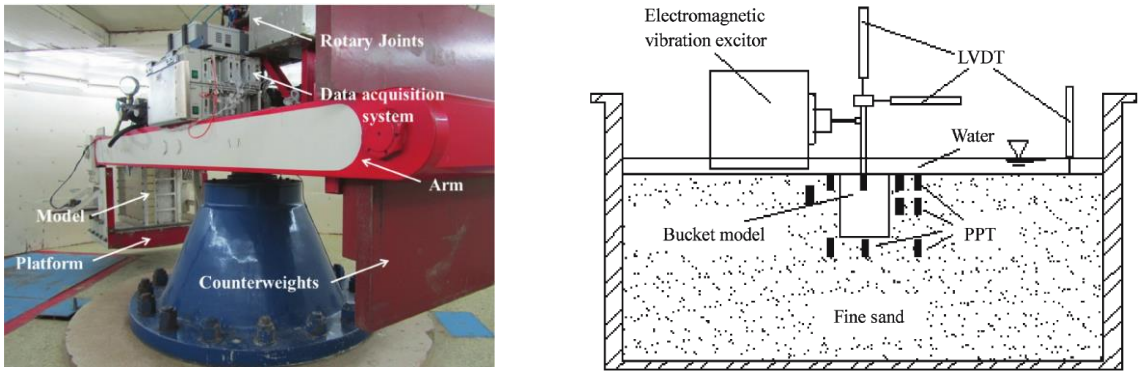

(a) (b)

Figure 1.12 (a) Photograph of the centrifuge at Tsinghua University (b) Layout of the model

1.3 Numerical studies on caisson foundations

1.3.1 Finite element modelling

An investigation of the failure surface and the bearing capacity characteristics entirely based on model tests is costly and time-consuming (Byrne 2000; Nguyen-Sy 2005; Villalobos et al. 2010; Ibsen et al. 2013; Foglia et al. 2015). A more timesaving and economic approach are numerical finite element simulations, sometimes combined with experimental data. It is however worth mentioning that the numerical analysis reliability depends strongly on whether the simulations can accurately reproduce the nonlinear behaviour of the soil.

In recent years, many researchers have numerically investigated the response of a caisson foundation in sand. Examples include the vertical bearing capacity characteristics during the installation procedure (Erbrich and Tjelta 1999; Houlsby and Byrne 2004; Senders and Randolph 2009; Harireche et al. 2013; Cerfontaine et al. 2015; Cerfontaine et al. 2016; Park et al. 2016) and the bearing capacity behaviour under combined general loadings (Achmus et al. 2013; Liu et al. 2014; Gerolymos et al. 2015; Li et al. 2015; Zafeirakos and Gerolymos 2016; Bagheri et al. 2017; Skau et al. 2018). Table 1.6 lists the related research studies on the behaviour of caisson foundations subjected to combined monotonic and cyclic loadings by analytical or numerical (Finite Element Method – FEM) approaches.

Table 1.6 Summary of analytical and numerical studies on the behaviour of a caisson foundation subjected to combined monotonic and cyclic loadings

Approach	Constitutive Model	Soil Type	Soil parameter calibration	Content of analysis	Bibliographic Reference
Analytical calculation	/	Dense sand	/	Resistance to penetration with and without suction	Houlsby and Byrne (2004)
Analytical calculation	/	(Medium) dense sand	/	Suction required during installation	Senders and Randolph (2009)
Analytical calculation	/	Sand	/	Effect of soil resistance and critical suction during installation	Harireche et al. (2013)
FEM **ABAQUS**	Drucker-Prager	Dense sand	Drained triaxial test	Mechanisms during installation, including critical gradients of suction, degradation of skirt friction and tip	Erbrich and Tjelta (1999)

				resistance	
FEM **LAGAMINE**	Prevost	Very dense sand	Drained triaxial test (Andersen et al. 2008)	Monotonic and cyclic behavior upon vertical transient loading	Cerfontaine et al. (2015) Cerfontaine et al. (2016)
FEM **ABAQUS**	Mohr-Coulomb	Sand	Empirical value	Vertical load transfer mechanism and bearing capacity	Park et al. (2016)
FEM **ABAQUS**	Mohr-Coulomb	(Very/medium) dense sand	Back-calculation	Bearing behavior under drained monotonic loading	Achmus et al. (2013)
FEM **ABAQUS**	Mohr-Coulomb	Dense sand	Soil strength profile in specific area (East China Sea)	Yield envelope in 2D and 3D spaces and failure mode	Liu et al. (2014)
FEM **ABAQUS**	Armstrong-Frederik (Frederick and Armstrong 2007)	Cohesive soil	Empirical value	Response to combined vertical, horizontal and moment loading	Gerolymos et al. (2015)
FEM **Z-SOIL** (Truty et al. 2011)	HSS (Benz 2007)	Saturated marine sand	Back analysis with FEM	Influence factors on the horizontal and moment bearing capacity; rotation center positions under monotonic horizontal loading	Li et al. (2015)
FEM **ABAQUS**	BWGG (Giannakos et al. 2012)	Dense sand (Marked as 14/25 Leighton Buzzard sand)	Empirical correlations	Bearing capacity under combined loading considering embedment ratio, vertical load magnitude and caisson-soil contact interface conditions	Zafeirakos and Gerolymos (2016)
FEM **PLAXIS 3D**	Mohr-Coulomb	(Medium) dense sand	Back-calculation	Behavior of the caisson and response of the soil supporting the caisson in (medium) dense sand subjected to static horizontal loading	Bagheri et al. (2017)

FEM **PLAXIS 3D**	NGI-ADP (Grimstad et al. 2012)	Clay and sand	Soil strength profile in specific area	Macroelement for a caisson foundation in clay. Results also for sand.	Skau et al. (2018)

Among the above mentioned research studies, Houlsby and Byrne (2004), Senders and Randolph (2009) and Harireche et al. (2013) proposed analytical methods to assess the installation of caisson foundations in sand with or without suction. Houlsby and Byrne (2004) compared the analytical predictions with four series of case records: (1) trail installations at Tenby and Sandy Haven, (2) the first jacket structure named Draupner E, (3) the second jacket named Sleipner T to be installed in the North Sea and (4) several laboratory-scale tests. Good agreement was found with the measured data. Senders and Randolph (2009) proposed a CPT-based method to estimate the self-weight penetration and suction required during the installation of suction caissons in dense sand. The method was able to satisfactory predict data from centrifuge model tests and from field installation. Harireche et al. (2013) found that a more accurate estimation of the critical suction during the installation process could be achieved by considering the effect of varying with depth permeability.

The remaining studies investigated numerically the installation procedure and/or bearing capacity of caisson foundations subjected to combined loadings in very dense sand (relative density of 90%). Cerfontaine et al. (2015, 2016) studied the axisymmetric behaviour of suction caisson installed in sand upon vertical monotonic and cyclic loading. The finite element code LAGAMINE combined with the Prevost model was adopted to consider drained and partially drained conditions. The simulation results indicated that the transient differential of pressure between the inside and outside of the caisson created a suction effect, increasing the caisson resistance both in traction and in compression (the increase was bigger in traction). For the cyclic loading cases, all simulations presented a settlement accumulation during the cyclic loading. The major part of the load variation was sustained by positive or negative variations of the pore water pressure within the soil inside the caisson and around it, leading to a low loading of the soil solid skeleton.

Gerolymos et al. (2015) investigated the response of a caisson foundation in cohesive soil subjected to combined vertical (N), horizontal (Q) and moment (M) loading. The finite element code ABAQUS with the Armstrong-Frederik Model (Frederick and Armstrong 2007) was adopted to study the ultimate states of failure envelopes in dimensionless normalized forms. The effects of the embedment ratio, vertical load and interface friction on the bearing capacity were studied in detail. Simulation results were then employed to develop a generalized expression for the bearing strength in the N-Q-M 3D space. The finite element results and the associated closed-form expression were

verified against an upper bound limit-equilibrium solution based on the Brinch Hansen theory for ultimate lateral soil reaction. Furthermore, the bearing strength envelope was validated for low and high-frequency dynamic loading. Results indicated that the maximum dynamic moment and horizontal force were bounded by the static bearing strength envelope for low-frequency loading conditions. For the high-frequency cases, a significant over strength was observed, attributed to the 'violent' impacts of the caisson on the sides of the gap.

Bagheri et al. (2017) conducted research on the behaviour of a caisson foundation in dense and medium-dense sand subjected to a static horizontal load. The finite element code Plaxis 3D and Mohr-Coulomb failure criterion was adopted to reproduce the elastic perfectly plastic stress-strain relationship. The adopted soil properties based on a back-calculation method were validated with field test results. Based on the numerical analysis results, dimensionless equations for load-displacement and moment-rotation relations were proposed. The simulation results indicated that the caisson skirt withstood the major part of the load, while the caisson lid had only a slight part.

It is noteworthy that various constitutive models have been adopted to study the response of caisson foundations subjected to combined loadings. Examples include plasticity constitutive models governed by the Mohr-Coulomb failure criterion (Achmus et al. 2013; Liu et al. 2014; Zafeirakos and Gerolymos 2016); the so-called NGI-ADP model based on an anisotropic undrained shear strength failure criterion (Skau et al. 2018) and an elasto-plastic model named the Hardening Small Stain model (HSS), which can reproduce basic macroscopic phenomena exhibited by the soil (Li et al. 2015). It is however necessary to point out that some studies adopted back-calculations of experimental field tests or empirical equations to calibrate the model parameters (Achmus et al. 2013; Zafeirakos and Gerolymos 2016). Some researchers used the representative soil strength profile of a specific area; however, related validation of soil parameters was not found in the literature (Liu et al. 2014; Skau et al. 2018). One study calibrated part of the model parameters with triaxial tests while obtaining the other using a back analysis and the finite element method (Li et al. 2015).

Up to the author knowledge, there is no available study today including conventional triaxial tests or model tests up to field tests, necessary to obtain more accurate results and to improve the engineering design and understanding of the nonlinear behaviour of caisson foundations. Furthermore, the abovementioned studies adopted the conventional finite element method and could not guarantee stress redistribution due to the caisson penetration or the evolution of the failure surface under large deformations. Extreme loading conditions (i.e. large deformations) need therefore to be considered together with a critical state based constitutive model as it describes more accurately the sand

characteristics, the influence of several soil parameters (density, friction angle, deformability, crushability etc.). and the evolving failure envelope.

1.3.2 Macroelement modelling

The finite element method allows the use of complicated constitutive laws, 3D meshes and the application of combined loadings. Nevertheless, the price to pay is the high computational demand in terms of running time, computer memory and data storage capacity. Furthermore, highly qualified engineers are needed to prepare and run the calculations and to do the post-treatment.

An alternative method is the macroelement concept, a generalised 2D or 3D stress-resultant model that concentrates the nonlinear behaviour of the soil foundation system to a reference point. The theory of plasticity has been often employed to reproduce the response of shallow foundations under combined loadings, see for example (Nova and Montrasio 1991; Montrasio and Nova 1997; Gottardi et al. 1999; Martin and Houlsby 2000; Byrne and Houlsby 2001; Cremer et al. 2001; Cassidy et al. 2002; Cremer et al. 2002; Houlsby and Cassidy 2002; 2004; 2006; Grange et al. 2008; Chatzigogos et al. 2009; Grange et al. 2009; Chatzigogos et al. 2011). Research has been also focused on modelling the response of bucket foundations for offshore wind turbines (Byrne 2000; Houlsby 2005; Villalobos Jara 2006; Achmus et al. 2013; Ibsen et al. 2013). Nguyen-Sy (2005) derived a hyperplastic model (Houlsby and Puzrin 2007) and applied it to bucket foundations. di Prisco et al. (2003a, 2003b) integrated the Nova and Montrasio (1991) model with a boundary surface model to represent cyclic loading. An application of the latter was presented in di Prisco et al. (2006). Buscarnera et al. (2010) used the same model to calculate the accumulated displacement of an onshore wind turbine on gravity-based foundation under wind loading. Kafle and Wuttke (2013) slightly modified the models of Nova and Montrasio (1991) and di Prisco et al. (2003) to predict the response of a footing on unsaturated soil. Foglia et al. (2015) conducted a series of monotonic and cyclic laboratory tests on a bucket foundation and the test results were interpreted within the macroelement approach, using an existing analytical model (Villalobos et al. 2009), suitably modified to accommodate the footing embedment and the application of cyclic load. Skau et al. (2018) adopted the multi-surface plasticity framework to analyse the characteristic behaviour of a bucket foundation subjected to irregular cyclic loading.

Macroelements considering rate-type hypoplastic constitutive equations (Kolymbas 1991; Tamagnini et al. 2000; Niemunis 2003) have been recently developed for shallow and deep foundations. Salciarini and Tamagnini (2009) proposed a hypoplastic macroelement for surface

footings. The same model was later extended to 6-DOF by Tamagnini et al. (2013). A hypoplastic macroelement for vertical and inclined piles has been recently developed by Li et al. (2016), Li et al. (2018). Table 1.7 lists the developed macroelement models of foundations including footing, spudcan and caissons in sand and clay subjected to monotonic and cyclic loadings in recent years.

Table 1.7 A list of existing macroelements for foundations in sand or clay

Modeling approach	Soil type	Framework	Foundation type	Loading	Reference
Model tests	Silica sand	Plasticity	Footing	Monotonic	(Nova and Montrasio 1991; Montrasio and Nova 1997)
FEM **DYNAFLOW**	Saturated clay	Plasticity	Footing	Cyclic, Seismic	(Cremer et al. 2001)
Model tests	Sand	Plasticity	Footing	Monotonic	(Houlsby and Cassidy 2002)
Model tests	Loose carbonate sand	Plasticity	Circular footing	Monotonic	(Cassidy et al. 2002)
Model tests	Silica sand (yellow Leighton Buzzard 14/25)	Plasticity	Footing	Monotonic	(Bienen et al. 2006)
Centrifuge tests	Clay	Plasticity	Caisson	Monotonic	(Cassidy et al. 2006)
Model tests	Sand and clay	Hyperplasticity	Caisson	Monotonic, Cyclic	(Nguyen-Sy and Houlsby 2005)
Model tests	Sand	Plasticity	Footing	Monotonic, Seismic	(Grange et al. 2008)
Model tests	Sand	Hypoplasticity	Footing	Monotonic, Cyclic	(Salciarini and Tamagnini 2009; Tamagnini et al. 2013)
Model tests	Silica sand (yellow Leighton Buzzard 14/25)	Plasticity	Caisson	Monotonic	(Villalobos et al. 2009)
FEM **ABAQUS**	Coarse-grained soil	Plasticity	Footing	Cyclic	(Buscarnera et al. 2010)
Model tests	Sand	Plasticity	Footing	Monotonic, Cyclic	(Chatzigogos et al. 2011)
Model tests	Unsaturated sand	Plasticity	Footing	Cyclic	(Kafle and Wuttke 2013)
Model tests	Saturated sand	Plasticity	Caisson	Monotonic	(Ibsen et al. 2013)

Centrifuge tests	Soft clay (UWA kaolin clay)	Plasticity	Spudcan	Monotonic	(Zhang et al. 2014)
Model tests	Sand (Aalborg University Sand No.1)	Bounding surface plasticity	Caisson	Monotonic, Cyclic	(Foglia et al. 2015)
Centrifuge tests	Sand	Hypoplasticity	Pile	Monotonic, Cyclic	(Li et al. 2016; Li et al. 2018)
FEM **PLAXIS 3D**	Over consolidated clay	Multi-surface plasticity	Caisson	Monotonic, Cyclic	(Skau et al. 2018)

More details about the existing macroelements for caisson foundations in sand or clays (Byrne and Houlsby 1999; Cassidy 1999; Gottardi et al. 1999; Villalobos et al. 2005; Cassidy et al. 2006; Villalobos Jara 2006; Foglia et al. 2015; Skau et al. 2018) are given in the Appendix. Their main characteristics are provided Table 1.8.

Table 1.8 Framework of macroelements for caisson foundations in sand and clay

Elastic behavior	Yield surface	Hardening law	Flow rule	Reference
$\begin{bmatrix} V/GR^2 \\ H/GR^2 \\ M/GR^2 \end{bmatrix} = DG \begin{bmatrix} k_{VV}^0 & 0 & 0 \\ 0 & k_{HH}^0 & k_{HM}^0 \\ 0 & k_{HM}^0 & k_{MM}^0 \end{bmatrix} + \begin{bmatrix} dw_p \\ d\theta_p \\ du_p \end{bmatrix}$	$y = \left(\frac{H}{h_0 V_0}\right)^2 + \left(\frac{M}{Dm_0 V_0}\right)^2 + 2e\frac{H}{h_0 V_0}\frac{M}{Dm_0 V_0}$ $-F(V, V_t, V_0) = 0$	$V = \frac{kw_p}{1 + (\frac{kw_{pm}}{V_{peak}} - 2)(\frac{w_p}{w_{pm}}) + (\frac{w_p}{w_{pm}})^2}$	$\begin{bmatrix} dw_p \\ d\theta_p \\ du_p \end{bmatrix}_p = \lambda \begin{bmatrix} \frac{\partial g}{\partial V} \\ \frac{\partial g}{\partial H} \\ \frac{\partial g}{\partial M} \end{bmatrix}$ $g = (\frac{H}{V' h_0})^2 + (\frac{M}{V' m_0 D})^2$ $-2a(\frac{H}{V' h_0})(\frac{M}{V' m_0 D})$ $-\alpha_v^2 \beta_{34} (\frac{V}{V'})^{2\beta_3} (1 - \frac{V}{V'})^{2\beta_4} = 0$	(Byrne and Houlsby 1999; Cassidy 1999; Gottardi et al. 1999; Villalobos et al. 2005)
$\begin{bmatrix} dV \\ dM/D \\ dH \end{bmatrix} = DG \begin{bmatrix} k_v & 0 & 0 \\ 0 & k_m & k_c \\ 0 & k_c & k_h \end{bmatrix} \begin{bmatrix} dw_e \\ Dd\theta_e \\ du_e \end{bmatrix}$	$y = (\frac{V}{V_u})^2 + [\left(\frac{M}{M_u}\right)\left(1 - \alpha_1 \frac{HM}{H_u \lvert M \rvert}\right)]^2$ $+ \left\lvert \left(\frac{H}{H_u}\right)^3 \right\rvert - 1 = 0$	$V = (\alpha_i D_i + \alpha_0 D_0) s_{u1} \pi w$ $+ (N_c s_{u2} + \gamma' w) \pi D_{ave} t$ $V = \alpha_0 D_0 \pi L s_{u1}$ $+ N_c^* s_{u2} \frac{\pi D_0^2}{4}$ $V = -\alpha_0 D_0 \pi w s_{u1}$ $- N_c^* s_{u2} \frac{\pi D_0^2}{4}$	$dw_p = \lambda \frac{\partial f}{\partial V}$, $du_p = \lambda \frac{\partial f}{\partial H}$, $d\theta_p = \lambda \frac{\partial f}{\partial M/D}$	(Cassidy et al. 2006)

$\begin{bmatrix} V' \\ M \\ H \end{bmatrix} = DG \begin{bmatrix} K_V & 0 & 0 \\ 0 & K_M & K_{MH} \\ 0 & K_{MH} & K_H \end{bmatrix} \begin{bmatrix} w \\ \theta \\ u \end{bmatrix}$	$y = t^2 - \beta_{12}^2 (v_1 + t_0)^{2\beta_1} (1 - v_2)^{2\beta_2} = 0$ $t = \sqrt{h^2 + m^2 - 2emh}$ $h = \frac{a_H \chi_H + (1 - \mathrm{a_H})\mathrm{H}}{h_0 V_0} \quad v_1 = \frac{a_{V_1} \chi_V + (1 - a_{V_1}) V'}{V_0}$ $m = \frac{a_M \chi_M + (1 - \mathrm{a_M}) M}{2 R m_0 V_0} \quad v_2 = \frac{a_{V_2} \chi_V + (1 - a_{V_2}) V'}{V_0}$	/	$\begin{Bmatrix} \dot{\alpha}_V \\ \dot{\alpha}_M \\ \dot{\alpha}_H \end{Bmatrix} = \lambda \begin{Bmatrix} \frac{\partial y}{\partial \chi_V} \\ \frac{\partial y}{\partial \chi_M} \\ \frac{\partial y}{\partial \chi_H} \end{Bmatrix}$	(Villalobos Jara 2006)
$\boldsymbol{q} = \begin{pmatrix} \eta \\ \varepsilon \\ \zeta \end{pmatrix} = V_M \begin{pmatrix} w \\ u\mu \\ \psi D\theta \end{pmatrix}$ $\boldsymbol{Q} = \begin{pmatrix} \xi \\ h \\ m \end{pmatrix} = \frac{1}{V_M} \begin{pmatrix} V \\ H/\mu \\ M/(D\psi) \end{pmatrix}$	$f = h^2 + m^2 - (\xi + t_s \rho_c)^2 (1 - \frac{\xi}{\rho_c})^{2\beta}$	$d\rho_c = (1 - \rho_c) \frac{R_0}{V_M} \left(d\eta + \frac{\alpha \lvert d\varepsilon \rvert}{\mu} + \frac{\gamma \lvert d\zeta \rvert}{\psi} \right)$	$dq_p = \Lambda \frac{\partial g}{\partial Q}$ $g = (\mathrm{h}\lambda)^2 + (\mathrm{m}\chi)^2$ $-(\xi + \mathrm{t_s}\,\rho_\mathrm{g})^2 (1 - \frac{\xi}{\rho_\mathrm{g}})^{2\beta}$	(Foglia et al. 2015)
$D = \begin{bmatrix} k_v^e & 0 & 0 \\ 0 & k_h^e & 0 \\ 0 & 0 & k_\theta^e \end{bmatrix}$	$\frac{\partial g_i}{\partial F} = \frac{\partial f_i}{\partial F}$ $f_i = \left(\frac{V - \alpha_{i,V}}{V_{i,\max}} \right)^2 + \left(\frac{H - \alpha_{i,H}}{H_{i,\max}} \right)^2$ $+ \left(\frac{M - \alpha_{i,M}}{M_{i,\max}} \right)^2 - 1 = 0$	$du^p = \sum_{i=1}^{k} du_i^p = \sum_{i=1}^{k} d\lambda_i \cdot \partial g_i / \partial F$	$\frac{\partial g_i}{\partial F} = \frac{\partial f_i}{\partial F}$ $g_i = \left(\frac{V - \alpha_{i,V}}{V_{i,\max}} \right)^2 + \left(\frac{H - \alpha_{i,H}}{H_{i,\max}} \right)^2$ $+ \left(\frac{M - \alpha_{i,M}}{M_{i,\max}} \right)^2 - 1 = 0$	(Skau et al. 2018)

1.4 Conclusions

This first chapter of the manuscript focused on a brief literature review on experimental and numerical studies on the behaviour of caisson foundations subjected to combined loadings. The finite element method used often in the literature for the simulations cannot however guarantee the stress redistribution during the caisson penetration, the evolution of the failure surface and the characterisation of the failure modes under large deformations. Furthermore, a comprehensive study combining conventional triaxial tests, model tests and field tests is still lacking. These issues are treated in the following chapters.

Chapter 2 Numerical investigation on the evolving failure of caisson foundations: Combined Lagrangian - SPH technique, Mohr-Coulomb model

2.1 Introduction

Caisson foundations are often used in offshore engineering. For an optimum design, understanding the failure process of a caisson during its installation and the subsequent external loadings is crucial. Extensive experimental field tests on small-scale and full-scale caisson foundations have been conducted to determine the installation characteristics and the lateral load suction foundation capacity (Hogervorst 1980; Tjelta et al. 1986; Tjelta 1995). Field tests are valuable as they help to obtain necessary data for the foundation design, nevertheless they are expensive and time consuming. For these reasons, model laboratory tests have been also conducted under controlled experimental conditions either in clay (Houlsby et al. 2005; Villalobos et al. 2010; Barari and Ibsen 2012) or sand (Houlsby et al. 2006; Cox et al. 2013; Foglia and Ibsen 2013; Zhu et al. 2013). Finally, 2D and 3D numerical studies have been also performed (Erbrich and Tjelta 1999; Sukumaran et al. 1999; El-Gharbawy and Olson 2000; Deng and Carter 2002) to investigate the foundation bearing capacity under different loading combinations and drainage conditions. In all these numerical studies however, the installation process was ignored and the evolving failure and the final failure modes under different loading combinations were not discussed.

This chapter focuses on the investigation of the failure process and failure modes of a caisson foundation in sand by numerical modelling. As the failure evolves under large deformations, a combined Lagrangian - Smoothed Particle Hydrodynamics method (SPH) is adopted for the simulations. This numerical strategy is first validated by simulating cone penetration tests in sand. Then, an experimental campaign of a caisson in the same sand is selected to calibrate the model. More representative loading combinations are then chosen to reproduce the failure process. Finally, three additional caisson dimensions (D/d=0.5, 1.5 and 2.0, changing the ratio of the caisson diameter D to the skirt length d while keeping the same soil-structure surface contact area) under six representative combined loading paths are studied to investigate the influence of the caisson dimensions to the failure process and failure modes.

2.2 Combined Lagrangian - SPH technique

The Smooth Particle Hydrodynamics (SPH) method was first developed by Gingold and Monaghan (1977) for simulations in astrophysics. Further developments of the method allowed for applications to a broad range of problems in solid mechanics. In SPH simulations, the computational domain is discretized into a finite number of particles, each representing a certain volume and mass of material (fluid or solid) and carrying simulation parameters such as acceleration, velocity, density and pressure/stress.

The material properties $f(x)$ at any point x in the simulation domain are calculated according to an interpolation process over its neighboring particles that are within an influence domain Ω through

$$f(x) = \int_{\Omega} f(x') W(x - x', h) \, \mathrm{d}x' \tag{2-1}$$

where W is the kernel or smoothing function, which is essentially a weighting function.

The continuous integral representation of the field variable $f(x)$ in Eq.(2-1) can be further approximated by the summation over neighboring particles as

$$f(x) = \sum_{i=1}^{N} f(x_i) W(x - x_i, h) V_i = \sum_{i=1}^{N} f(x_i) W(x - x_i, h) \frac{m_i}{\rho_i} \tag{2-2}$$

where V_i , m_i and ρ_i are the volume, mass and density of the i^{th} particle, respectively; and N is the number of particles within the influence domain. The spatial derivative of field variable $f(x)$ can be approximated through the differential operations on the kernel function

$$\frac{\partial f(x)}{\partial x} = \sum_{i=1}^{N} \frac{m_i}{\rho_i} f(x_i) \frac{\partial W(x - x_i, h)}{\partial x_i} \tag{2-3}$$

The efficiency and accuracy of SPH simulations depend on the kernel function (see Eq.(2-1) and Eq.(2-3)). The SPH particles are used as interpolation points and are the basis for calculating all the field variables in the continuum around them. The SPH particles, like the objects in astrophysics,

can be separated by large distances. The field variables between the SPH particles are approximated (smoothed) by smoothing shape functions. The interaction between SPH particles starts when a particle gets to a certain distance (smoothing length *h*) from another one. SPH particles interact with each other only if they are within the influence domain. Otherwise, they are independent. Therefore, a larger smoothing length (i.e. larger influence domain) results in a smoother or more continuous behavior; whereas a smaller smoothing length (i.e. smaller influence domain) yields more discrete behaviors as the SPH particles are more independent.

In a solid body discretized with densely packed SPH particles there is no connectivity defined between the particles through the mesh. A major attraction of the SPH technique is therefore that there is no need for a fixed computational grid when calculating spatial derivatives. Instead, estimates of derivatives are obtained from analytical expressions based on the derivatives of the smoothing functions (Li and Liu 2002). Since the connectivity between the particles is generated as a part of the computation and can change over the time, the SPH method can handle analysis of very large deformations and displacements.

One disadvantage of the SPH method over the Lagrangian method is however the necessary computational requirements (Bojanowski 2014). The SPH method is also less accurate under small deformations. For this reason, in the following only a part of the soil domain is modeled with the SPH method while a Lagrangian model is adopted for the rest (combined Lagrangian-SPH technique). The combined Lagrangian-SPH technique already implemented in the commercial finite element code ABAQUS is adopted. The function "Tie Constraint" of the code treats the interface between the SPH and the Lagrangian domains so that no relative motion exists. It allows fusing two domains even though their meshes are not identical. More details on this modeling strategy can be found in the ABAQUS manual (ABAQUS 2014).

The SPH method implemented in ABAQUS uses the explicit time integration method (Hibbitt et al. 2001). As shown in Figure 2.1, the equilibrium condition is first written with the balance of internal force and external force,

$$M\ddot{u}_{(t)} = P_{(t)} - I_{(t)} \tag{2-4}$$

where M is the mass matrix; $\ddot{u}$ is the acceleration; P is the applied external force vector, and I is the internal force vector.

The equations of motion for the body are then integrated using the explicit time central-difference integration rule as follows:

$$\begin{cases} \dot{u}_{\left(t+\frac{\Delta t}{2}\right)} = \dot{u}_{\left(t-\frac{\Delta t}{2}\right)} + \dfrac{\Delta t_{(t+\Delta t)} + \Delta t_{(t)}}{2} \ddot{u}_{(t)} \\ u_{(t+\Delta t)} = u_{(t)} + \Delta t_{(t+\Delta t)} \dot{u}_{\left(t+\frac{\Delta t}{2}\right)} \end{cases} \tag{2-5}$$

where u is the displacement and the subscript t refers to the time in an explicit dynamic step. $\dot{u}$ is the velocity; Δt is the increment of time. For the stability of calculation, the time increment Δt should be smaller than a limited value $\Delta t \approx L_{\min}/c_d$ with the smallest element dimension of mesh L_{min} and the dilatory wave speed c^d.

Finally, incremental strain calculated by incremental displacement will be called by the constitutive model to update stresses and then internal forces, up to a new equilibrium condition.

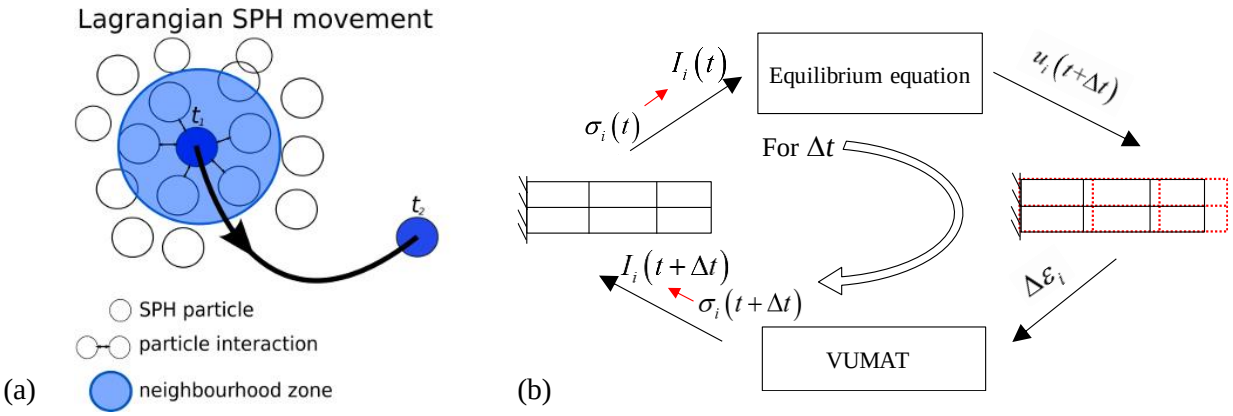

Figure 2.1 SPH numerical method (a) kinetics and interactions of a SPH particle and (b) Flow chart of explicit analysis

2.3 Validation of the numerical strategy

In the following, the combined Lagrangian-SPH model is first calibrated and validated using experimental results of a sand cone penetration test and of a caisson foundation.

2.3.1 Experimental campaign

A well-documented series of laboratory tests of a caisson foundation in sand (marked as baskarp sand no. 15) including Cone Penetration Tests (CPT), the installation phase and the application of monotonic loadings is selected hereafter, Foglia et al. (2015). The experimental set-up consisted of a sand box (1600 mm × 1600 mm × 1150 mm), a loading frame and a hinged beam. A system of steel

cables and pulleys induced loadings to the foundation through an electric motor drive placed on the hinged beam. The load, set by means of three weight hangers, was transferred to the foundation through a vertical beam bolted on the caisson lid. The foundation was instrumented with three LVDTs and two load cells (see in Figure 2.2).

Figure 2.2 Testing rig at Aalborg University, Foglia et al. (2015)

Cone Penetration Tests (CPT) were carried out to assess the soil parameters. The caisson foundation was made of steel, with an outer diameter of 300 mm, a lid thickness of 11.5 mm, a skirt length of 300 mm and a skirt thickness of 1.5 mm. Six tests on caisson foundations were then performed under different monotonic loading combinations (one pure vertical load up to failure and five dimensionally homogeneous moment to horizontal load ratios (M/DH=1.1, 1.987, 3.01, 5.82, 8.748) at constant vertical load).

2.3.2 Numerical model

The numerical model has the same dimensions as the experimental box. The horizontal displacements are constrained on the lateral sides as well as all the translational degrees of freedom at the bottom. A perfect elasto-plastic Mohr-Coulomb model is adopted for the soil behavior (the constitutive equations are presented in the Appendix). The constitutive model parameters are obtained based on the tests results of Ibsen et al. (2009). We get finally: Young modulus E 26 MPa, the Poisson ratio υ 0.25, the frictional angle ϕ 40.8°, the dilation angle ψ 17.5°, and the cohesion c 6 kPa. Furthermore, the density is taken equal to 1100 kg/m^3, the friction coefficient of the soil-caisson interface 0.35 (k=tan (ϕ/2)) and the damping ratio is set to 0.

In the combined Lagrangian - SPH model, only the portion of the soil experiencing large deformations is modeled with SPH particles (see Figure 2.3). The SPH domain has a length of 1400 mm (the side with the horizontal or moment loading), a width of 800 mm, a height of 1150 mm and a total number of 88407 particles. The Lagrangian mesh at the outside is composed by 105984 hexahedral elements. For numerical stability reasons, at least four SPH particles per face of a Lagrangian element in contact are considered.

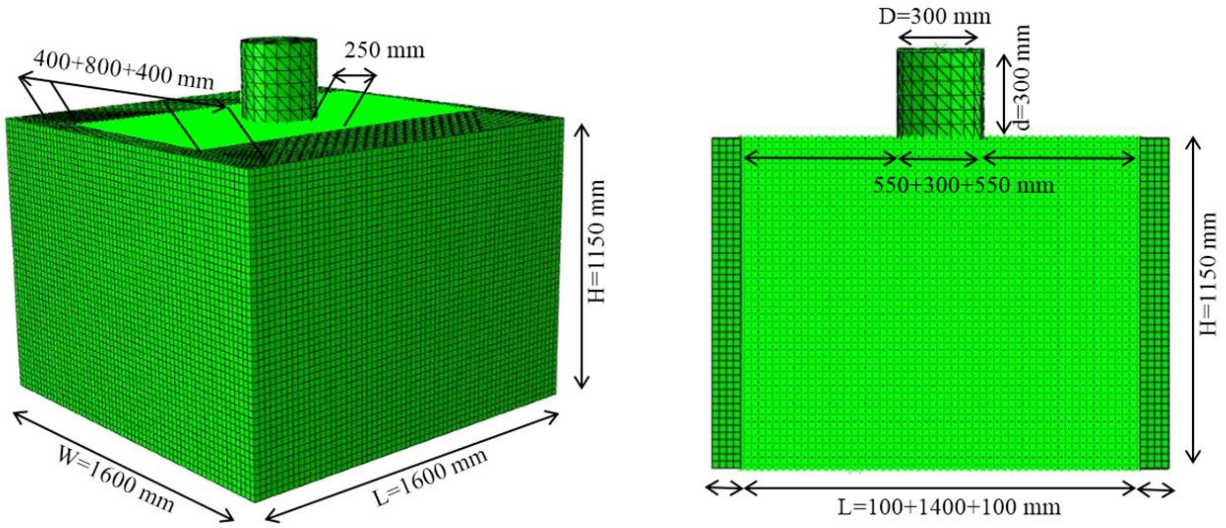

Figure 2.3 Combined Lagrangian - SPH model

The caisson is modeled using 927 rigid tetrahedron elements with the same dimension and thickness as in the experiments. According to Foglia et al. (2015), the density of the caisson is taken equal to 7800 kg/m^3, the Young modulus 200 GPa and the Poisson ratio 0.3. The caisson is initially positioned on the surface of soil at the center of box. For the CPT tests simulation, the caisson is replaced by a cylinder bar (using 807 rigid tetrahedron elements) with a diameter of 20 mm and a 60 degrees cone at bottom.

2.3.3 Validation using CPT tests

In order to validate the combined Lagrangian - SPH model with the chosen material parameters, CPT test simulations are first carried out. The cone penetration velocity is taken equal to 5 mm/s, following Foglia et al. (2015). A rigid Mohr-Coulomb type interface model is adopted applied on the entire (tip and shaft) surface of the cone.

A comparison of the experimental and numerical results is presented in Figure 2.4, where four CPT experimental tests are provided by Foglia et al. (2015). A good agreement is achieved which

indicates that the combined Lagrangian - SPH model is validated. It can be used in the following to simulate the nonlinear behavior of caisson foundations.

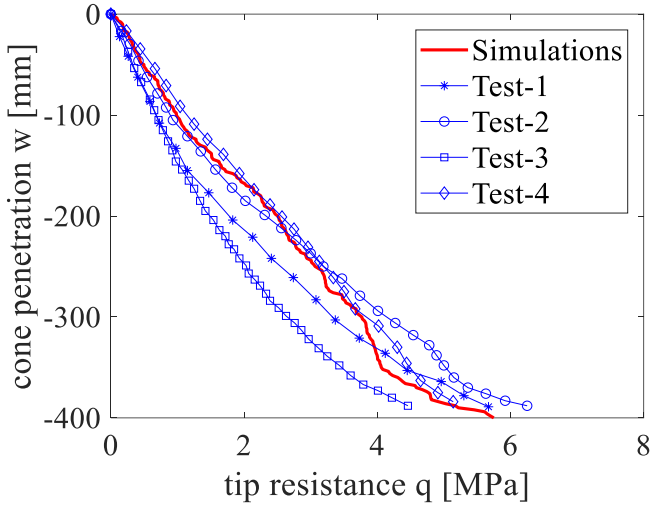

Figure 2.4 Comparison between experiments and simulation of CPT tests, CLSPH Mohr-Coulomb model

Each SPH particle represents one gauss integration point. As in the finite element approach, the total strain of each particle is divided into an elastic and a plastic part. The equivalent plastic strain PEEQ is therefore defined as PEEQ = $\sqrt{\frac{2}{3}\cdot\dot{\varepsilon}_{ij}^{p}:\dot{\varepsilon}_{ij}^{p}}$ (where $\dot{\varepsilon}_{ij}^{p}$ is the tensor of the plastic strain rate). The fields of equivalent plastic strain (PEEQ), the deviatoric stress (S Mises, Pa) and the mean effective stress (S Pressure, Pa) corresponding to a penetration of 400 mm are plotted in Figure 2.5 which shows reasonable distributions and an influence distance much smaller than the SPH domain.

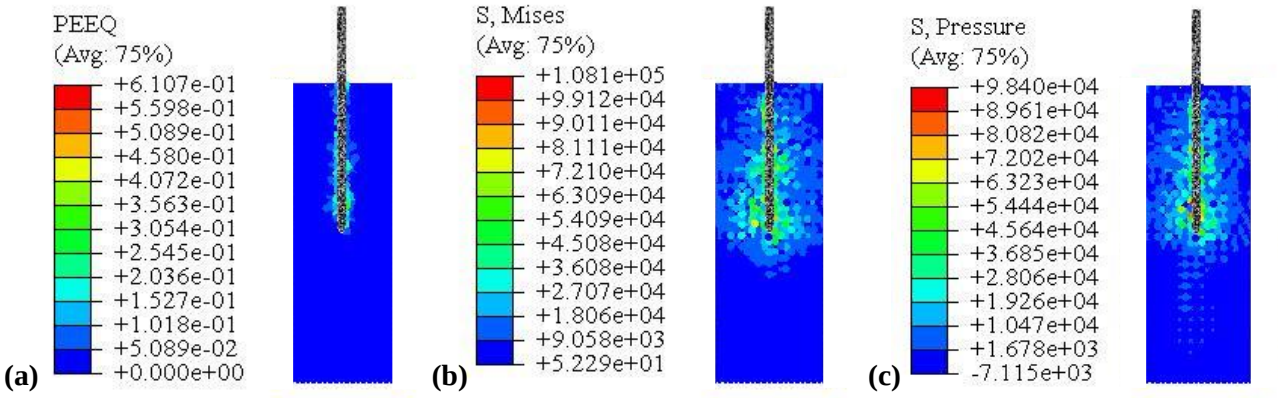

Figure 2.5 Results of CPT simulation, CLSPH Mohr-Coulomb model: fields of (a) equivalent plastic strain (PEEQ), (b) deviatoric stress (S Mises, Pa) and (c) mean effective stress (S Pressure, Pa)

2.3.4 Validation using caisson foundation tests

The combined Lagrangian - SPH model of Figure 2.3 is used hereafter to simulate one pure penetration test (Hogervorst 1980) by vertical displacement control at a rate of 5 mm/s, and five tests at different dimensionally homogeneous moment to horizontal load ratios (M/DH=1.1, 1.987, 3.01, 5.82, 8.748) (Foglia et al. 2015). The tests are done under a constant vertical load of 241 N and combined horizontal - rotation control at the middle point of the caisson.

ABAQUS explicit is used for the simulations. For explicit calculations, the loading rate is usually ten times the real loading rate in order to save computational time. Nevertheless, the quasi-static state of the simulation should be guaranteed (Qiu et al. 2009). In ABAQUS/SPH, quasi-static conditions are defined when the ratio of the kinematic energy over the internal energy is smaller than 5%. Noting that the loading rates were not presented in the monotonic tests. For the calculations presented hereafter, a displacement rate of 10 mm/s and rotation rate of 0.5 degree/s are selected after many attempts to find an optimum trade-off between computational time and computational stability. All monotonic loading paths are followed until the horizontal capacity (H_R) or moment capacity (M_R) are reached. The displacements and rotations corresponding to the horizontal capacity (H_R) or moment capacity (M_R) are summarized in Table 2.1.

Table 2.1 Displacements and rotations for capacity level loadings and for different M/DH values, CLSPH Mohr-Coulomb model

M/DH	u (mm)	$D\theta$ (mm)	H_R (N)	M_R/D (N)
1.1	5.8	7.4	420	540
1.987	4.6	6.0	330	640
3.01	4.0	5.5	190	690
5.82	5.0	6.8	110	700
8.748	3.5	5.1	90	760

Figure 2.6 shows the applied vertical force versus the vertical displacement for the pure vertical loading test (comparison between the experimental results and the numerical simulations). Figure 2.7 presents the horizontal load (H) versus the horizontal displacement (U) and the dimensionally homogeneous moment (M/D) versus the rotational displacement ($D\theta$) for five M/DH values (1.100, 1.987, 3.010, 5.820 and 8.748). For all tests a good agreement is achieved between the experiments and the simulations. The combined Lagrangian – SPH model with the chosen material parameters is therefore well calibrated. It can be used for further numerical investigations of the failure process and mode of caisson foundations.

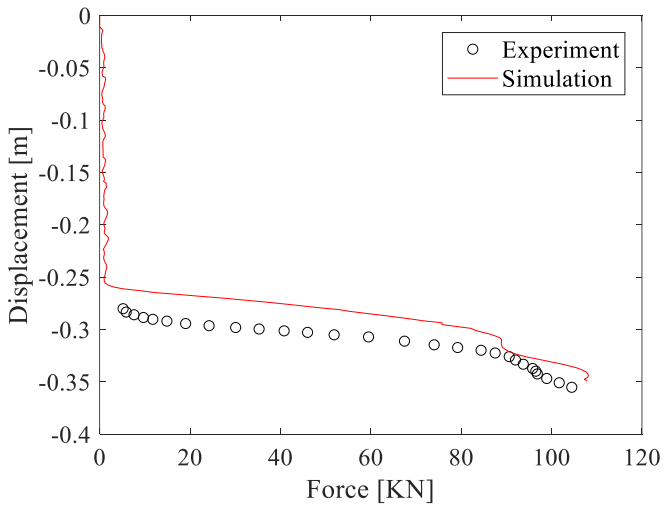

Figure 2.6 Pure vertical loading test: vertical displacement versus vertical force, comparison of experiments and simulations, CLSPH Mohr-Coulomb model

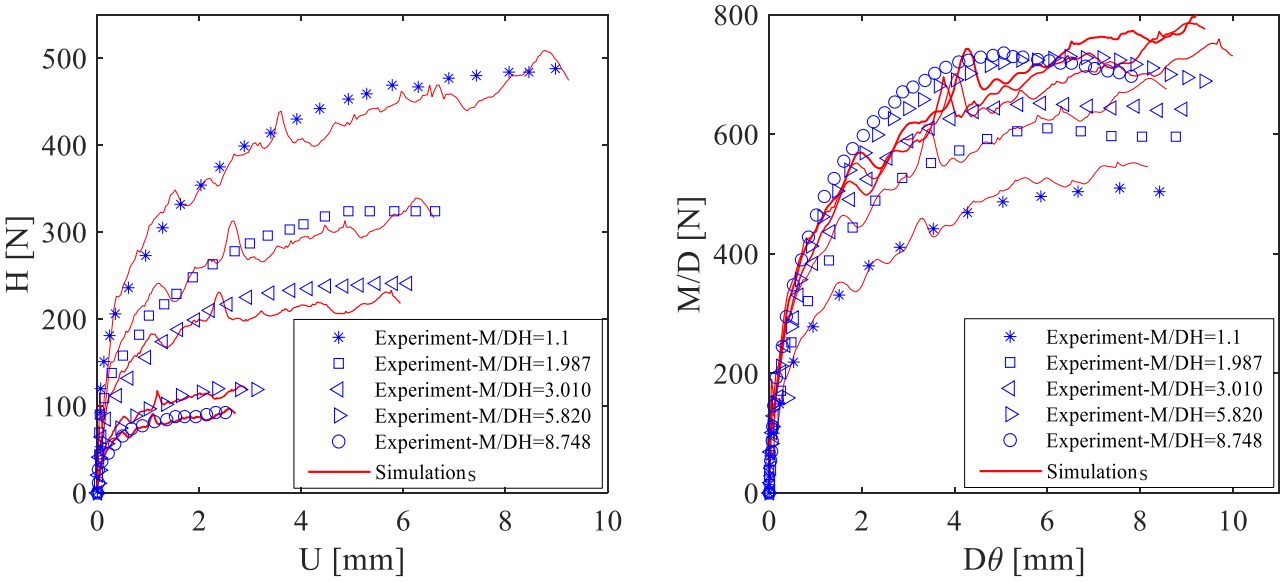

Figure 2.7 Monotonic multidirectional loading tests: (a) horizontal force versus horizontal displacement, (b) dimensionally homogeneous moment versus rotational displacement, comparison of experiments and simulations for five *M*/*DH* values, CLSPH Mohr-Coulomb model

It can be observed that the calculated curves are not smooth. This is probably due to numerical noise, typical for SPH calculations with the explicit time integration scheme. The numerical noise can be affected by various factors, such as the time increment, the contact law between the foundation and the soil and the application of the mass scaling method for improving the calculation efficiency.

Two extreme cases are selected hereafter to study large deformations: one pure vertical loading test and one moment combined horizontal loading test (*M/DH*=8.748). The fields of equivalent plastic strain (PEEQ), deviatoric stress (S Mises, Pa) and mean effective stress (S Pressure, Pa) are plotted in Figure 2.8. Distributions are again reasonable and the influence distance (in vertical and horizontal directions) is again much smaller than the SPH domain.

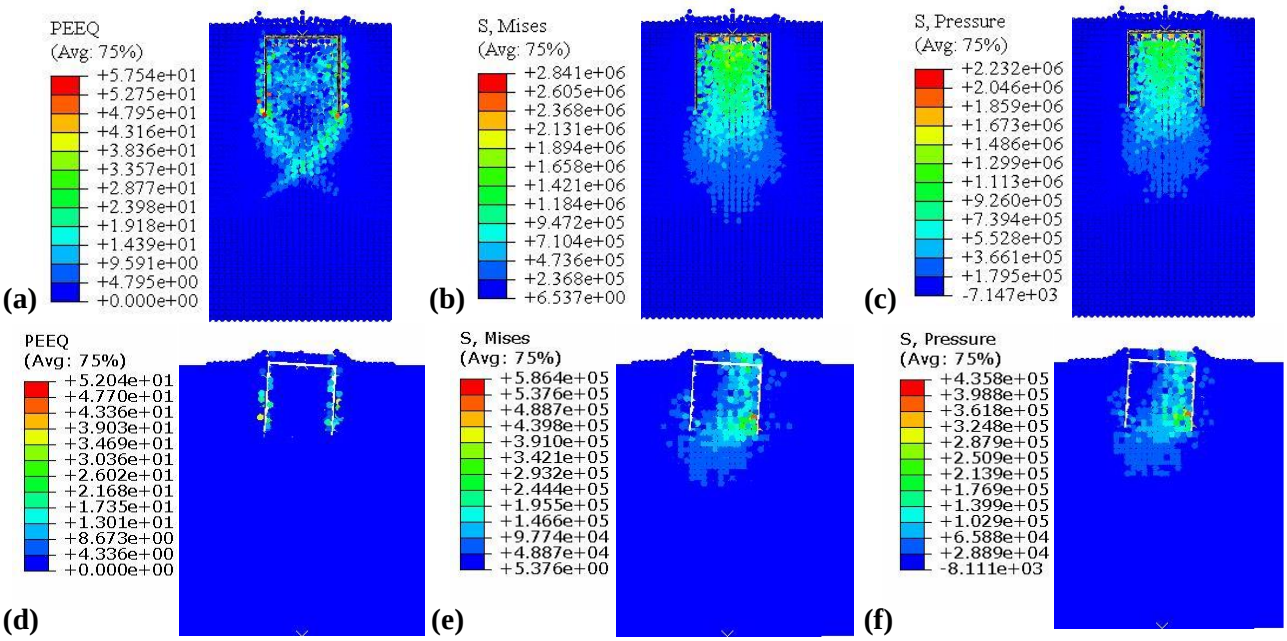

Figure 2.8 Contour of plastic deviatoric strain (PEEQ), deviatoric stress (S, Mises, Pa) and Mean stress (S Pressure, Pa) for (a-c) pure vertical loading test and (d-f) moment combined horizontal loading test (M/DH=8.748), CLSPH Mohr-Coulomb model

Finally, the bearing capacity diagrams (or failure envelopes) in the *H:M/D* loading plane and for the same vertical loading provided by the numerical simulations and by models of reference in the literature (Villalobos et al. (2010), Ibsen et al. (2014) and Foglia et al. (2015)) are compared in Figure 2.9. A good agreement is again achieved, validating the adopted numerical strategy.

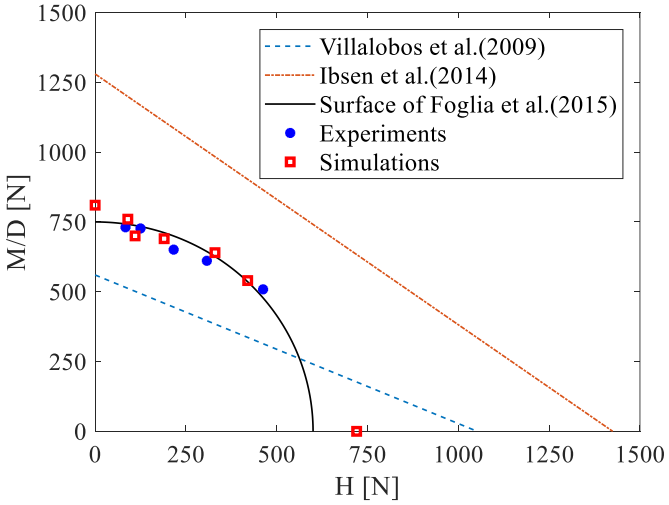

Figure 2.9 Failure envelope in the *H:M/D* loading plane for the same vertical loading: simulation with the CLSPH Mohr-Coulomb model versus experimental results and predictions of models of reference

2.4 Numerical analysis of failure process and failure modes

Based on the validated numerical model, various tests under different loading combinations are simulated hereafter: three single loading tests (P-V, P-H and P-M for pure vertical, pure horizontal and pure moment loading respectively), four tests under two combined loadings (C-VH for combined horizontal and vertical loadings, C-VM for combined vertical loading and moment, C-H^+M for combined horizontal loading and moment at the same direction, C-H^-M for combined horizontal loading and moment at the opposite direction), and two tests under three combined loadings (C-VH^+M and C-VH^-M which are similar to C-H^+M and C-H^-M with additional vertical loading). During all simulations, the displacement rate is kept equal to 10 mm/s and the rotation rate 0.5 degree/s. The applied displacement or rotation angle is big enough to ensure the complete development of a sliding surface in the sand.

Figure 2.10 illustrates the way to determine F_y; the softening part is not considered; the peak value is used to define failure. The results of the test simulations are summarized in Table 2.2. The evolution of the sliding surface of the caisson foundation is represented by the equivalent plastic strain. Five phases are illustrated: $0.33F_y$ (F_y being the force or moment on the failure surface), $0.66F_y$, $0.95F_y$, $2D_{Fy}$ (D_{Fy} is the displacement or rotation angle at $0.95F_y$) and $4D_{Fy}$. Table 2.3 presents specific views at $4D_{Fy}$. In particular, the XZ, XY, YZ sections and the overall (3D) view are included.

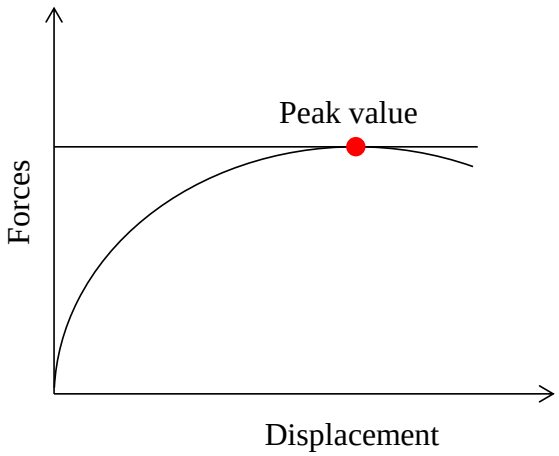

Figure 2.10 Determination of the peak values

Table 2.2 Evolution of the sliding surface of a caisson foundation in sand under different loading paths, CLSPH Mohr-Coulomb model

	F=0.33F_y	F=0.66F_y	F=0.95F_y	S=2D_{Fy}	S=4D_{Fy}
P-V	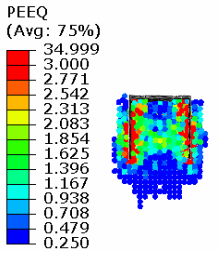	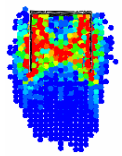	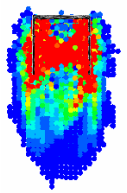	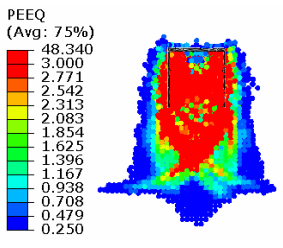	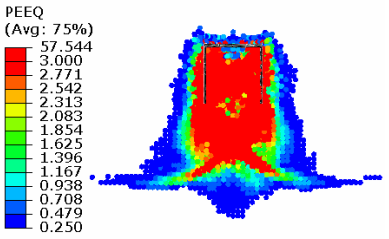
P-H	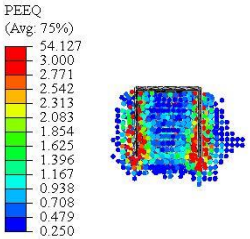	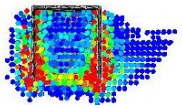	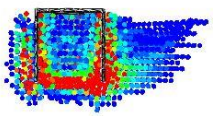	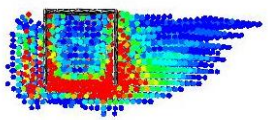	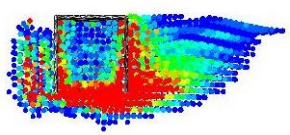
P-M	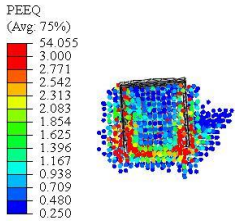	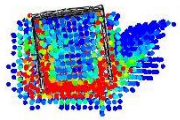	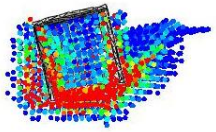	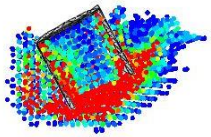	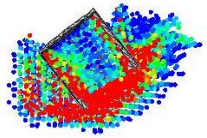
C-HV	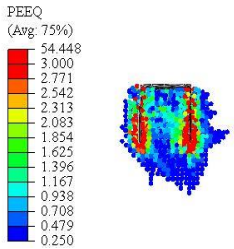	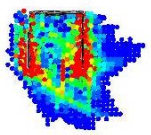	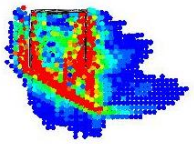	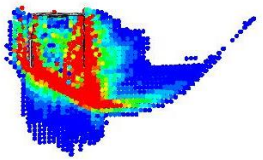	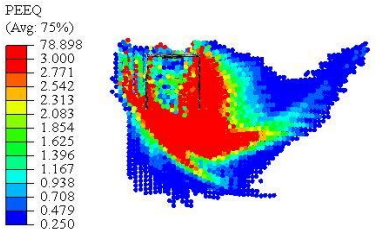

C-VM	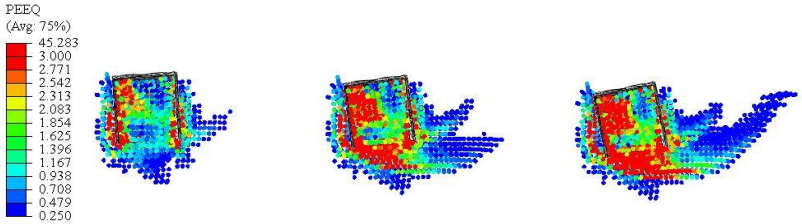	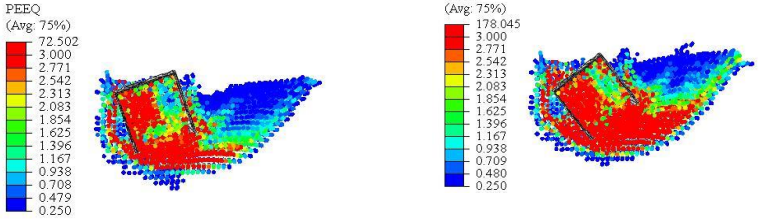	
C-H^{+}M	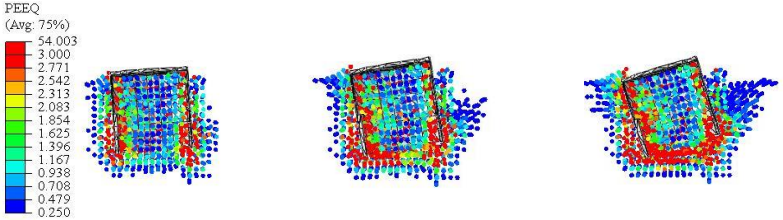			
C-H^{-}M	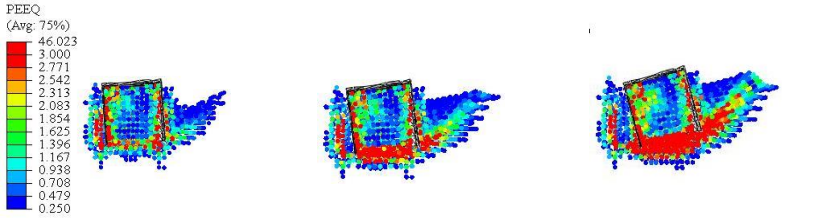		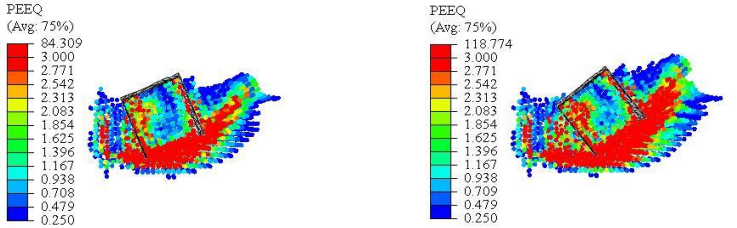	
C-H^{+}VM	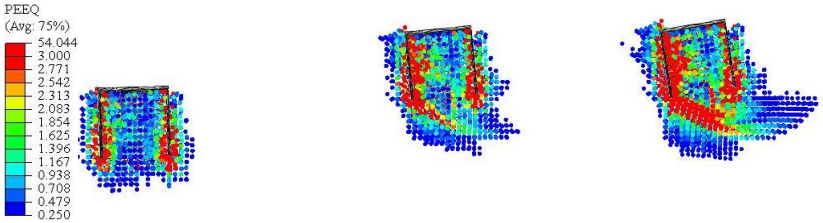		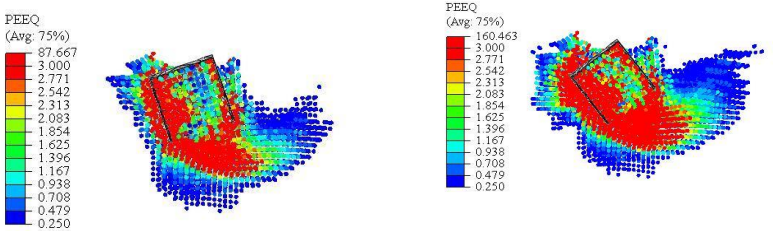	

C-H-VM	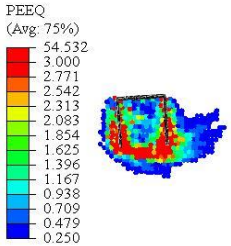 PEEQ (Avg: 75%) 54.532 3.000 2.771 2.542 2.313 2.083 1.854 1.625 1.396 1.167 0.938 0.709 0.479 0.250	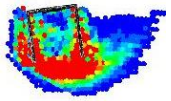	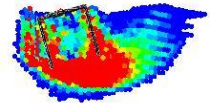	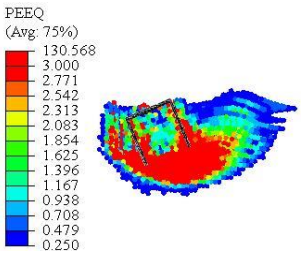 PEEQ (Avg: 75%) 130.568 3.000 2.771 2.542 2.313 2.083 1.854 1.625 1.396 1.167 0.938 0.708 0.479 0.250	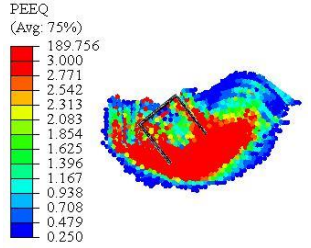 PEEQ (Avg: 75%) 189.756 3.000 2.771 2.542 2.313 2.083 1.854 1.625 1.396 1.167 0.938 0.708 0.479 0.250

Table 2.3 Specific views of the sliding surface of a caisson foundation in sand under different loading paths, CLSPH Mohr-Coulomb model

	XZ-section view	XY-section view	YZ-section view	Overall view
P-V	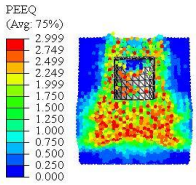	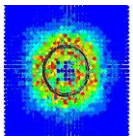	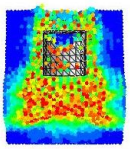	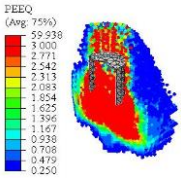
P-H	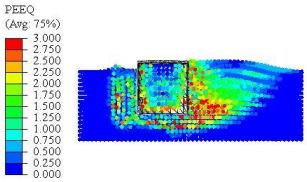	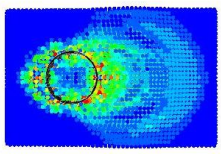	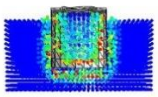	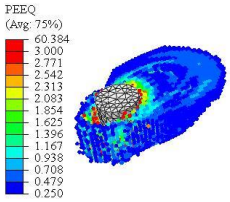
P-M	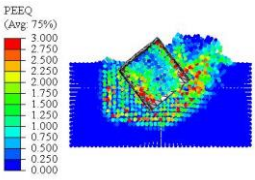	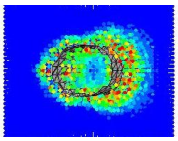	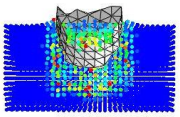	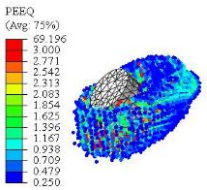
C-HV	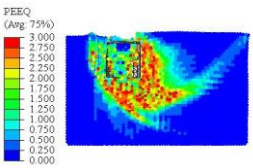	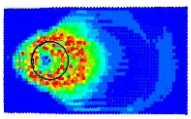	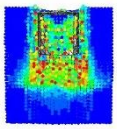	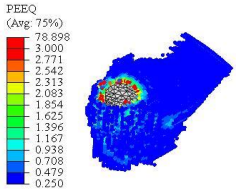
C-VM	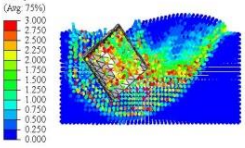	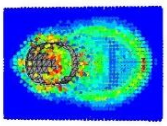	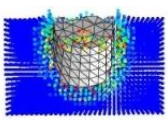	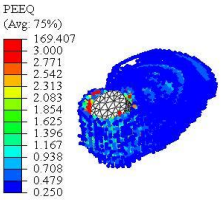
C-H^{+}M	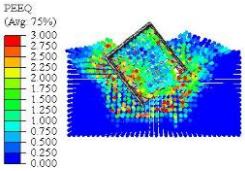	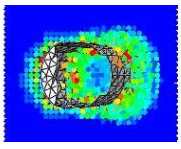	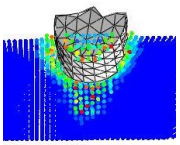	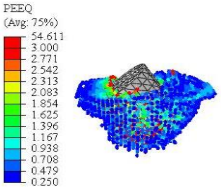

C-H⁻M	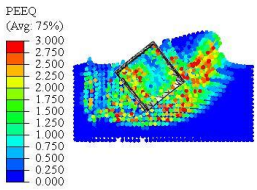	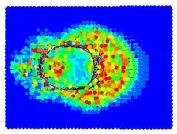	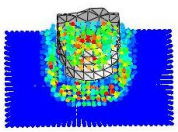	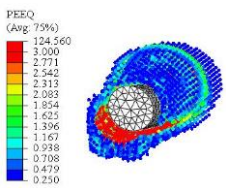
C-H⁺VM	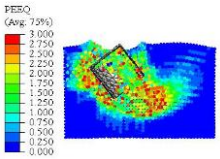	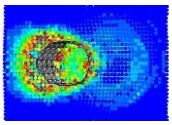	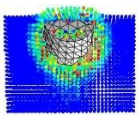	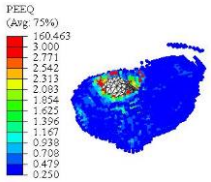
C-H⁻VM	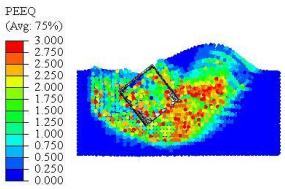	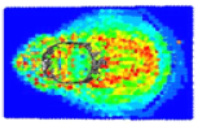	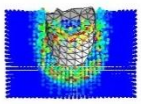	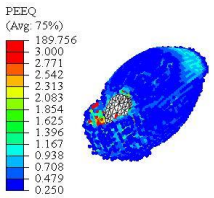

2.4.1 Failure modes under single loading paths

For the single vertical loading test (P-V), the plastic zone expands at the beginning along the vertical direction. With increasing displacement, the soil underneath the caisson is compressed and the plastic zone expands also along the horizontal direction. Significant plasticity concentrates on the bottom of the caisson. The final plastic zone looks like a matrass, as shown in Table 2.2.

For the single horizontal loading test (P-H), the plastic zone expands in the horizontal direction, see Table 2.2. The shear stress at the bottom of the caisson being higher, the plastic zone expands less at the bottom than in the above layer. As a result, the final sliding surface is similar to spheroidicity, see Table 2.3. Plastic zone is mainly situated on the sliding plane and near the right skirt of the caisson.

For the single moment loading test (P-M), the plastic zone expands in the circumferential direction. Comparing with the previous two cases, the plastic zone occupies a smaller area and it is primarily concentrated on the sliding plane near the left inner skirt of the caisson.

2.4.2 Failure modes under two combined loading paths

For the C-VH case, the plastic zone extends first in the resultant force direction H and V, 45° with the horizontal direction. With increasing displacement, a polarization of the plastic zone occurs.

As shown in Table 2.2, the plastic zone extends in with two directions, the horizontal and the vertical. The plastic zone mainly concentrates on the 45° glide plane, the areas near the right skirt and at the bottom of the caisson. Compared to the cases of pure vertical and pure horizontal loading, the plastic zone of the C-VH case can be considered as the superposition of the former two.

Under combined V and M loadings, case C-VM, the plastic zone expands along with the vertical and the circumferential directions. Compared to the case of the pure moment, the extension of the plastic zone in the circumference is larger. The final sliding surface approximates as a spheroidicity. High plastic zone primarily centralizes on the sliding plane near the left inner skirt of the caisson.

As shown in Table 2.1, the plastic zone expands in the circumferential and horizontal directions under combined H and M loadings for the C-H^{+}M case. As mentioned above, because the shear stress at the upper soil layer is smaller, the sliding surface looks like a basin and the plastic zone is basically bilateral symmetric. Compared to the case of the pure moment, the plastic zone extends mostly at the left side.

Similar to the above case, the plastic zone of the C-H^{-}M case expands along with the circumferential and horizontal directions. Compared to C-H^{+}M and because of the opposite direction of horizontal loading, the plastic extension is more apparent. The plastic extension of H and M is mutually stimulative, with a positive correlation. A high plastic area centralizes mainly on the sliding plane and has the form of a continuous zone expanding in the horizontal and circumferential directions.

2.4.3 Failure modes under three combined loading paths

As shown in Table 2.2, the extension of the plastic zone for C-H^{+}VM follows three directions, i.e. horizontal, vertical and circumferential. The final sliding surface is a shape of hemispheroidicity. The plastic zone primarily concentrates on the left skirt (including the inner and outer sides) of the caisson and near the bottom.

For the C-H^{-}VM case, the edge of the plastic zone has the shape of a smooth arc. With the rotational displacement increasing, the upper soil layer is lifted. The plastic zone concentrates primarily on the sliding plane near the caisson bottom. Like for the C-H^{-}M case, the extension of the plastic zone due to H and M is mutually stimulative. Compared to C-H^{-}M case, the final sliding

surface is smaller, the reason being is that the vertical loading enhances the interaction between the caisson and the soil, thereby reducing the displacement and rotation of the caisson.

2.4.4 Bearing strength and sliding surface area under different loading conditions

In order to find the relation between the bearing strength and the sliding surface expansion under different loading conditions, the sliding surface area is calculated hereafter for each case. The shape of the sliding surfaces for all cases can be approximated as an ellipsoid, which can be described as,

$$\frac{x^2}{a^2}+\frac{y^2}{b^2}+\frac{z^2}{c^2}=1 \tag{2-6}$$

where a, b and c respectively define the length of the ellipsoid in the three dimensions expressed as:

$$\begin{cases} a = 0.25a_1 + 0.5a_2 + 0.25a_3 \\ b = 0.25b_1 + 0.5b_2 + 0.25b_3 \\ c = 0.25c_1 + 0.5c_2 + 0.25c_3 \end{cases} \tag{2-7}$$

To measure (a_1, a_2 and a_3), (b_1, b_2 and b_3) and (c_1, c_2 and c_3), an illustrative example is given hereafter; as shown in Figure 2.11 and for the XZ-section, the weights of a_1, a_2 and a_3 are 0.25, 0.5 and 0.25 respectively, because of the irregular shape. A similar method is adopted for the two other directions.

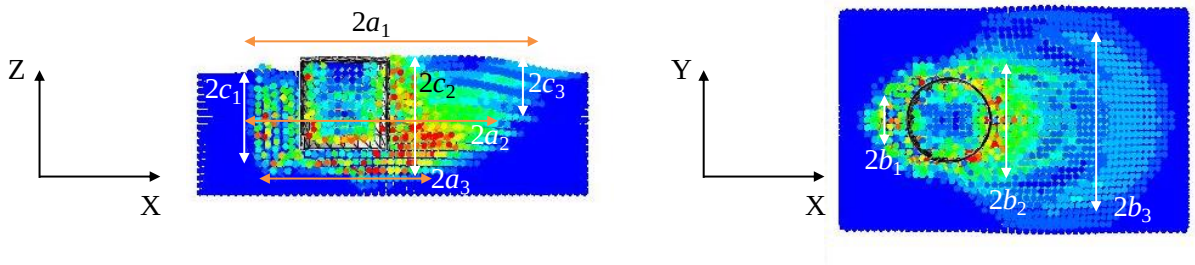

Figure 2.11 Illustrative example for calculating the sliding surface area

By measuring the length of the ellipsoid in the three dimensions, the sliding surface area is calculated following the Knud Thomsen formula,

$$S \approx 4\pi \left(\frac{a^{\xi} b^{\xi} + a^{\xi} c^{\xi} + b^{\xi} c^{\xi}}{3} \right)^{\frac{1}{\xi}} \tag{2-8}$$

where $\xi \approx 1.6075$ with the relative error approximates to 1.061% (Krajcik and McLenithan, 2001).

Results are summarized in Table 2.4. Figure 2.12 shows the sliding surface area under different loading paths.

Table 2.4 Bearing strength and sliding surface area under various loading paths, CLSPH Mohr-Coulomb model

	a (mm)	b (mm)	c (mm)	s (mm^2)	*V* (N)	*H* (N)	*M/D* (N)
P-V	665.9	665.9	866.3	2160432	87949	\	\
P-H	991.7	693.3	441.4	1547919	\	720	\
P-M	887.6	647.9	530.1	1473167	\	\	810
C-VH	1012.5	729.4	729.5	2117608	4227	923	\
C-VM	1070.1	817.7	660.7	2247553	4019	\	1237
C-H^{+}M	913.0	670.8	480.8	1468090	\	652	793
C-H^{-}M	807.6	572.1	511.6	1235435	\	563	652
C-VH^{+}M	1239.5	786.8	659.5	2465439	3771	852	939
C-VH^{-}M	807.6	572.1	757.5	1589610	4625	671	576

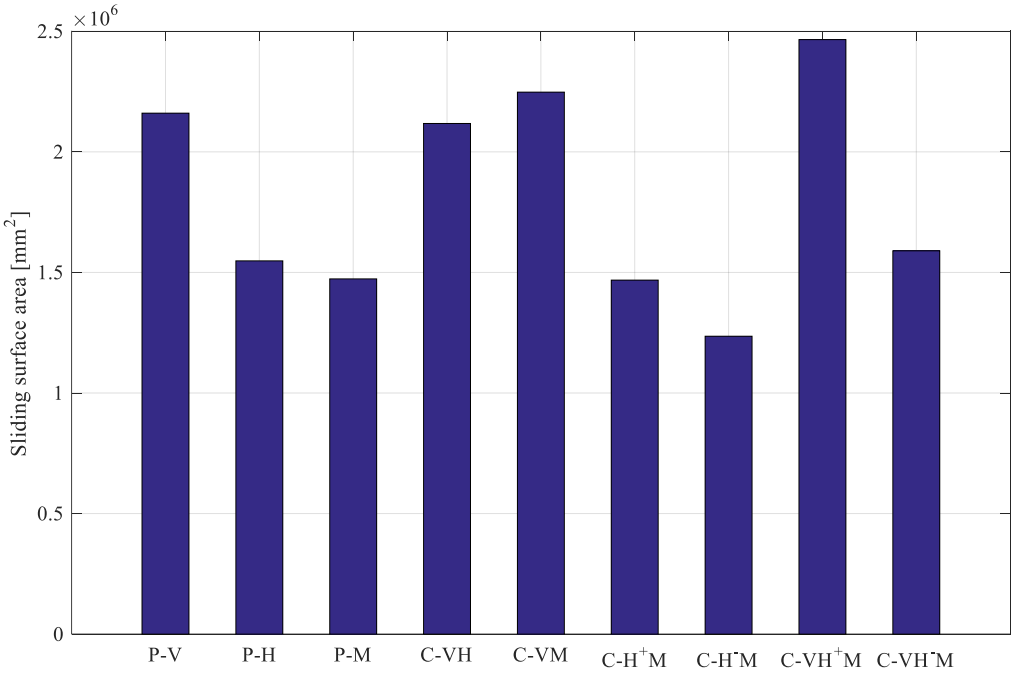

Figure 2.12 Sliding surface area under different loading paths, CLSPH Mohr-Coulomb model

As shown in Table 2.4 and Figure 2.12, among the single loading cases, the penetration test (pure vertical load) has the higher strength and the more significant sliding surface area. The sliding surface areas are nearly the same for the pure *H* and *M* cases. For the two combined loading cases, while *V* combined with *H* or *M*, compared to single loading case, the global bearing capacity is improved. For the three combined loading cases, comparing the case C-VH^{+}M to C-VH^{-}M, the higher sliding surface and the larger bearing capacity are observed when the direction of *H* and *M* are the same (see C-VH^{+}M case).

2.4.5 Influence of the caisson dimensions

Three additional caisson dimensions, designated as *D*/*d*=0.5, 1.5 and 2 (*D* being the caisson diameter and *d* the skirt length) with the same soil-structure contact area are studied hereafter: the narrow-deep caisson R0.5 (*D*=224mm, *d*=447mm), the wide-shallow caisson R1.5 (*D*=350mm, *d*=233mm) and the R2.0 (*D*=387mm, *d*=193mm). For each caisson configuration, six representative combined loading paths are selected for the simulations: H-V, V-M, H^{+}-M, H^{-}-M, H^{+}-V-M, H^{-}-V-M.As the failure progress and failure modes are found very similar to that of *D*/*d*=1.0 (only with a different sliding surface size), the plastic zones are not plotted in this section. Only the bearing strength and the sliding surface areas are used for the comparisons.

As shown in Figure 2.13, the bearing strength for vertical loads increases slightly and linearly, while the horizontal and moment capacities show a slightly linear decrease. Comparing the cases H^{+}-M to H^{-}-M, H^{+}-V-M to H^{-}-V-M, for the opposite direction of applied horizontal loading, the H and M bearing capacities reduce. When a vertical load is applied, the H and M bearing capacities are improved.

The sliding surface area is calculated for all cases and plotted in Figure 2.14. It can be seen that in all cases, with increasing *D/d* ratio, the sliding surface area decreases slightly and then increases linearly. Comparing the cases H^{+}-M to H^{-}-M, H^{+}-V-M to H^{-}-V-M, for the opposite direction of applied horizontal loading, the sliding surface expansion reduces. When a vertical load is applied, the sliding surface area increases.

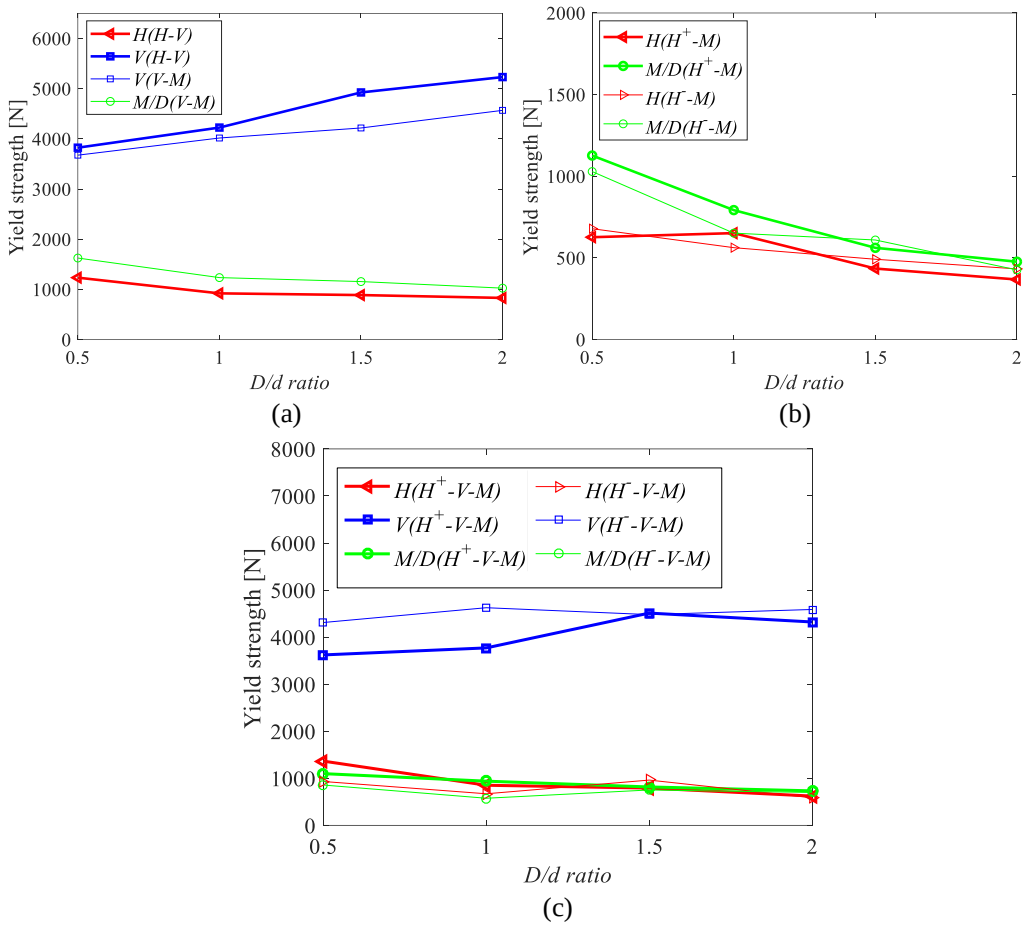

Figure 2.13 Bearing strength for different combined loadings and ratios *D/d*: (a) H-V & V-M, (b) H^+-M & H^--M, (c) H^+-V-M & H^--V-M, CLSPH Mohr-Coulomb model

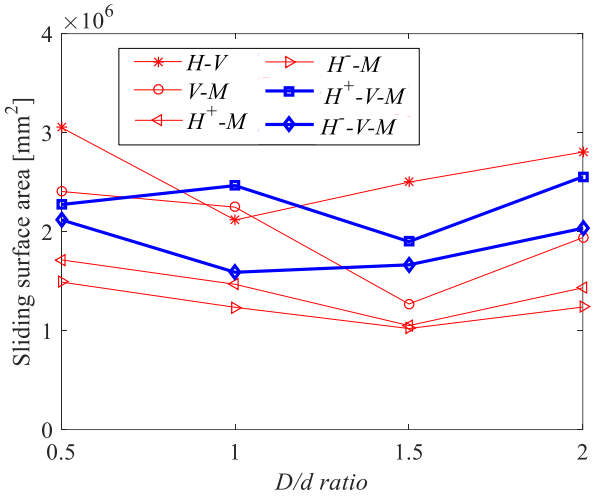

Figure 2.14 Sliding surface areas for different combined loadings and ratios *D/d,* CLSPH Mohr-Coulomb model

2.5 Conclusions

The evolving failure of a caisson foundation in sand was modelled under various loading combinations. A combined Lagrangian - Smoothed Particle Hydrodynamics method was adopted to deal with large deformations. The method was first calibrated and validated by simulating sand cone penetration tests. The results of an experimental campaign of a caisson were then used to further validate the approach.

More representative loading combinations were then chosen to numerically study the failure process and failure modes. It is concluded that, (1) the sliding surfaces for various combined loadings have the same shape but different sizes; (2) the vertical loading improves the horizontal or/and moment strength and thus increases the bearing capacity of the caisson foundation; (3) for the case when H and M are on the same direction, the sliding surface is more pronounced and the bearing capacity is bigger.

Various caissons with different dimensions were then simulated, submitted to representative combined loading paths. It was found that with increasing D/d ratio, the vertical loading bearing capacity increases slightly and linearly, while the horizontal and moment capacities present a slightly linear decrease. The sliding surface area first decreases slightly and then increases linearly.

A critical state-based soil model combined with the SPH method is introduced and validated with granular collapse experimental data in chapter 3. Then, in chapter 4, the validated model is used to further investigate the 3D bearing capacity diagram of caisson foundations under complex loading conditions and different soil parameters.

Chapter 3 SPH-SIMSAND numerical approach and validation with granular collapse experiments

3.1 Introduction

Granular collapse, such as debris, rock avalanches and landslides is a common issue in natural hazards. In order to understand this phenomenon, two types of experiments are often conducted: rectangular channel flowing tests, Balmforth and Kerswell 2005; Lajeunesse et al. 2005; Lube et al. 2005; Lube et al. 2007; Bui et al. 2008; Crosta et al. 2009 and column flowing tests, Lube et al. (2004, 2005 and 2007). In rectangular channel flowing tests, granular collapse is obtained by putting the granular material in a rectangular channel while quickly removing a vertical side boundary. In column flowing tests, the granular material is positioned in a hollow cylinder pipe. Daerr and Douady (1999) showed using low aspect ratio column granular collapse experiments that the final deposit morphology depends on the initial soil density. Lajeunesse et al. 2004; Lube et al. 2004; Lube et al. 2005; Lube et al. 2007 showed that the final deposit morphology (deposit radius, deposit height and slumping velocity) mainly depends on the initial aspect ratio of the granular column (the authors did not study the influence of soil density).

Recently, various numerical studies were also conducted to investigate granular collapse. Several authors confirmed that the final deposit morphology depends on the initial aspect ratio using the Discrete Element Method (DEM) (Staron and Hinch 2005; Zenit 2005; Lacaze et al. 2008; Girolami et al. 2012; Soundararajan 2015; Utili et al. 2015). In these articles, the effect of the initial void ratio (corresponding to the soil density) was not studied. Kermani et al. (2015) and Soundararajan (2015) simulated the effect of initial porosity on 3D asymmetrical collapsing and for different aspect ratios. The number of particles in the majority of DEM simulations being however limited, the applicability of this method to real scale problems remains questionable.

The finite element method was also adopted to reproduce granular collapse (Shen et al. 2014; Shen et al. 2017; Wu et al. 2016; Wu et al. 2017a). Crosta et al. 2009 used the classical Mohr-Coulomb and Drucker-Prager constitutive models and the Arbitrary Lagrangian-Eulerian technique. Zhang et al. 2015 the Particle Finite Element Method, Bui et al. 2008; Nguyen et al. 2016 the Smooth Particle Hydrodynamics (SPH) and Sołowski and Sloan 2015 the Material Point Method.

In this chapter we illustrate and validate the use of the Smooth Particle Hydrodynamics (SPH) method with a more advanced soil constitutive model than the Mohr-Coulom model used in the previous chapter. Combining the SPH method with a critical state constitutive model is a necessary step to identify a more realistic 3D failure surface for caisson foundations in sand (see chapter 4).

3.2 The SIMSAND critical state constitutive model

The SIMSAND model was developed based on the Mohr-Coulomb model by implementing the Critical State Line (CSL) concept (Yin et al. 2016a; Jin et al. 2017) with non-linear elasticity, non-linear plastic hardening, and a simplified three-dimensional strength criterion. The state-dependent peak strength and stress-dilatancy (contraction or dilation) are well captured by the SIMSAND model (Jin et al. 2017). The SIMSAND equations are summarized in Table 3.1. Calibration of the model parameters can be carried out using a straightforward way (Wu et al. 2017) or optimisation methods (Jin et al. 2016a,b; Yin et al. 2016b, see for example Table 3.2. for calibrated values for the Toyoura sand).

Table 3.1 The SIMSAND model

Components	Constitutive equations
Elasticity	$\dot{\varepsilon}_{ij}^{e}=\frac{1+\upsilon}{3K\left(1-2\upsilon\right)}\sigma'_{ij}-\frac{\upsilon}{3K\left(1-2\upsilon\right)}\sigma'_{kk}\delta_{ij} \quad K=K_0\cdot p_{at}\frac{\left(2.97-e\right)^2}{\left(1+e\right)}\left(\frac{p'}{p_{at}}\right)^{\zeta}$
Yield surface	$f=\frac{q}{p'}-H$
Potential surface	$\frac{\partial g}{\partial p'}=A_d\left(M_{pt}-\frac{q}{p'}\right);\ \frac{\partial g}{\partial s_{ij}}=\{1 \quad 1 \quad 1 \quad 1 \quad 1 \quad 1\}$
Hardening rule	$H=\frac{M_p\varepsilon_d^p}{k_p+\varepsilon_d^p}$
Critical state with inter-locking effects	$e_c=e_{ref}-\lambda\left(\frac{p'}{p_{at}}\right)^{\xi} \quad \tan\phi_p=\left(\frac{e_c}{e}\right)^{n_p}\tan\phi_\mu \quad \tan\phi_{pt}=\left(\frac{e_c}{e}\right)^{-n_d}\tan\phi_\mu$
Three-dimensional strength criterion	$M_p=\frac{6\sin\phi_p}{3-\sin\phi_p}\left[\frac{2c_1^{\,4}}{1+c_1^{\,4}+\left(1-c_1^{\,4}\right)\sin 3\theta}\right]^{\frac{1}{4}} \quad \text{with } c_1=\frac{3-\sin\phi_p}{3+\sin\phi_p}$ $M_{pt}=\frac{6\sin\phi_{pt}}{3-\sin\phi_{pt}}\left[\frac{2c_2^{\,4}}{1+c_2^{\,4}+\left(1-c_2^{\,4}\right)\sin 3\theta}\right]^{\frac{1}{4}} \quad \text{with } c_2=\frac{3-\sin\phi_{pt}}{3+\sin\phi_{pt}}$

* p_{at} atmospheric pressure (p_{at} = 101.3 kPa); p' effective mean pressure; q deviatoric stress; e_c critical state void ratio; ϕ_p peak friction angle; ϕ_{pt} phase transformation friction angle; M_{pt} stress ratio corresponding to the phase transformation; M_p peak stress ratio; θ Lode's angle, Sheng et al. (2000), Yao et al.(2004, 2008 and 2009) ; n_p and n_d parameters controlling the degree of interlocking due to neighboring particles, Yin and Chang (2010, 2013).

Table 3.2 The parameters of the SIMSAND model and calibrated values for the Toyoura sand

Parameters	Definitions	Value
K_0	Referential bulk modulus (dimensionless)	130 (kPa)
υ	Poisson's ratio	0.2
n	Elastic constant controlling the nonlinear stiffness	0.5
ϕ_μ	Critical state friction angle	31.5 (°)
e_{ref}	Initial critical state void ratio	0.977
λ	Constant controlling the nonlinearity of CSL	0.0596
ξ	Constant controlling the nonlinearity of CSL	0.365
A_{d}	Constant of magnitude of the stress-dilatancy	0.7
k_{p}	Plastic modulus related constant	0.0044
n_{p}	Inter-locking related peak strength parameter	2.4
n_{d}	Inter-locking related phase transformation parameter	2.9

The SIMSAND model was implemented into ABAQUS/Explicit as a user-defined material model via user material subroutine VUMAT. The procedure of model implementation follows the way of Hibbitt et al. (2001), see also chapter 2. In ABAQUS/Explicit combining with VUMAT, the strain increment on the element $\Delta\varepsilon$ at Δt is first solved by ABAQUS using an explicit time central-differential integration method. Then, the stress increment $\Delta\sigma$ is updated through VUMAT using the solved $\Delta\varepsilon$. For the stress integration, the cutting plane algorithm proposed by Ortiz and Simo (1986) was adopted.

3.3 Rectangular channel soil collapse simulations

3.3.1 Experimental and numerical configurations

In order to validate the SPH-SIMSAND model and the adopted numerical integration scheme, the rectangular channel soil collapse tests of (Bui et al. 2008)) are first simulated hereafter. In the experiments, small aluminium bars of various diameters (0.1cm and 0.15cm) were used to simulate soil. The bars were initially arranged into an area of 20cm length × 10cm height × 2cm width, delimited by two flat solid walls. The experiment starts by quickly moving the right wall horizontally to the right causing the flow of the aluminium bars to the side due to gravity (Figure 3.1).

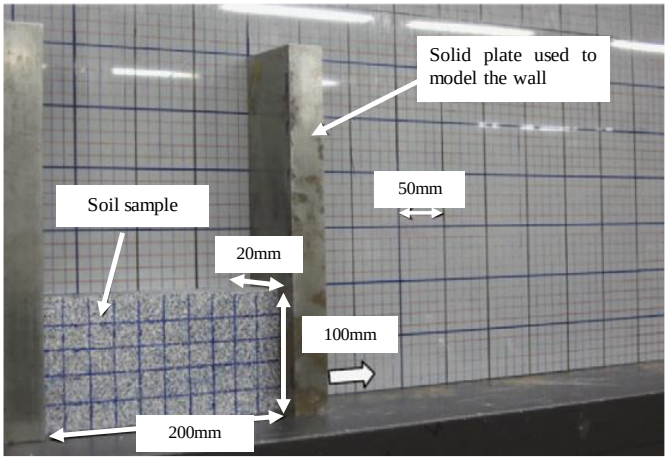

Figure 3.1 Rectangular channel soil collapse experiments, Bui et al. (2008)

In the numerical model, the spatial discretization domain is shown in Figure 3.2(a). SPH particles are used to model the soil while the two solid walls are discretized with rigid hexahedral finite elements. The initial SPH particles distance is (approximately) the same in the horizontal and vertical directions, in order to reproduce homogenous conditions.

A cell size of 0.2 cm was adopted for all the simulations hereafter by checking mesh dependency (Figure 3.2(b-d) with different sizes from 0.1 to 0.2 cm) and the particle space was half of the cell size (i.e. eight particles in each cell). The total number of particles was around 400,000. The bottom surface was set as a fixed boundary, whereas the nodal displacement of the four lateral boundaries were restricted in normal direction.

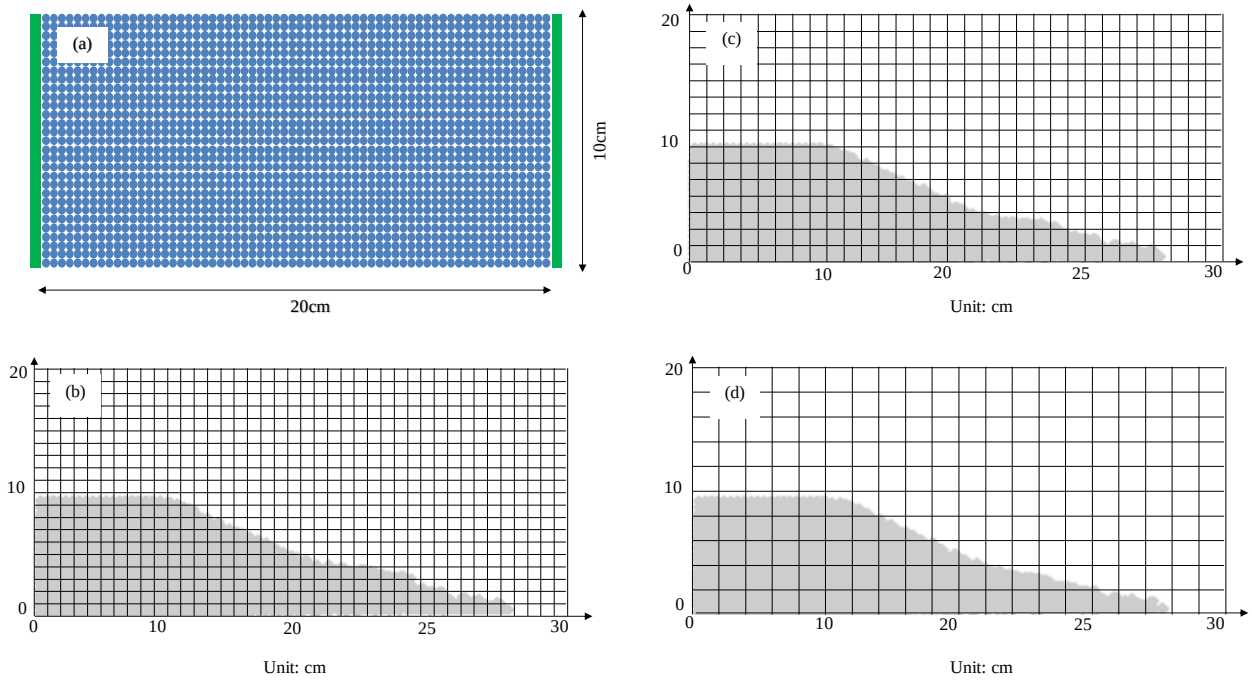

Figure 3.2 SPH particle density and mesh-dependency: (a) 2D spatial domain discretization for SPH particles and rigid hexahedral finite elements, (b) cell size of 0.1 cm (c) cell size of 0.15 cm (d) cell size of 0.2 cm

Due to the lack of mechanical tests on the experimental behaviour of the material used in the rectangular channel soil collapse tests, the SIMSAND model is adopted for the numerical simulations calibrated for the Toyoura sand, see Table 3.2. Figure 3.3 presents the typical state-dependent behaviour of granular materials simulated by the SIMSAND model under a very low confining stress (as was the condition in the rectangular channel soil collapse tests). It can be observed that the initial void ratio (or initial density) significantly influences the peak strength and the dilation/contraction. which should be considered in granular collapse since the density is highly changing during the collapse. Actually and following Lube et al.(2004 and 2005), the collapse behaviour is less sensitive to the grain properties of the granular material than to its density. Furthermore, density is highly changing during the collapse and should therefore be considered.

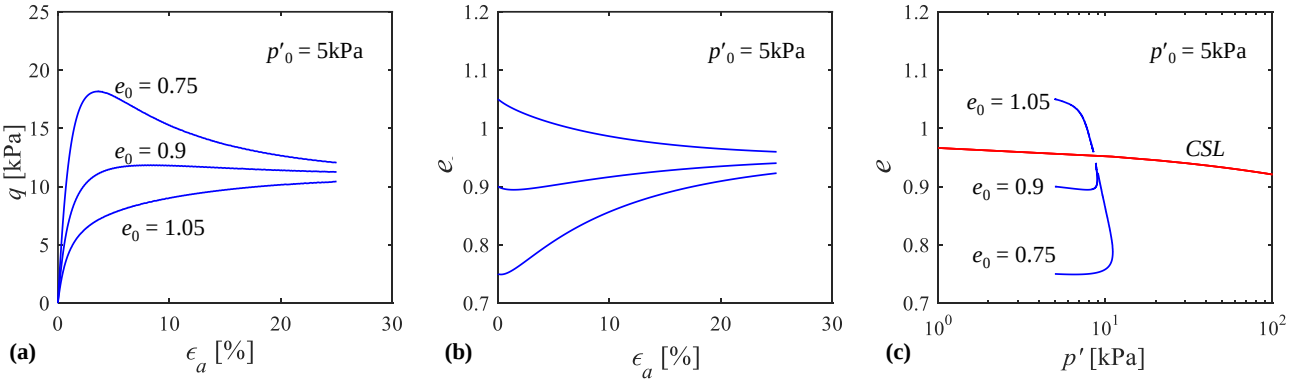

Figure 3.3 Simulated stress-strain behaviour of conventional triaxial tests using the SIMSAND model calibrated for the Toyoura sand: (a) deviatoric stress versus axial strain, (b) void ratio versus axial strain, and (c) void ratio versus mean effective stress in demi-logarithmic scale

The simulation of the experiments is carried out in two steps: a) the first step to balance the geostatic field and b) the second step to move the right wall along the horizontal direction with a speed of 1m/s to the right. The contacts between the sand and the two walls are described with the classical Coulomb law with a friction coefficient $\mu = \tan(\phi_\mu/2) = 0.28$.

3.3.2 Validation

Different void ratios e_0 from 0.75 to 1.05 are assumed hereafter for the simulations and compared with the experimental results. As shown in Figure 3.4, the smaller the void ratio (or the higher the initial density), the steeper the free surface and failure line and the longer the run-out

distance. This agrees with the experimental results of Lube et al. (2005). Luckily, the simulation with e_0= 0.95 fits well the experiment. Thus, e_0= 0.95 is adopted as a reference void ratio in the following.

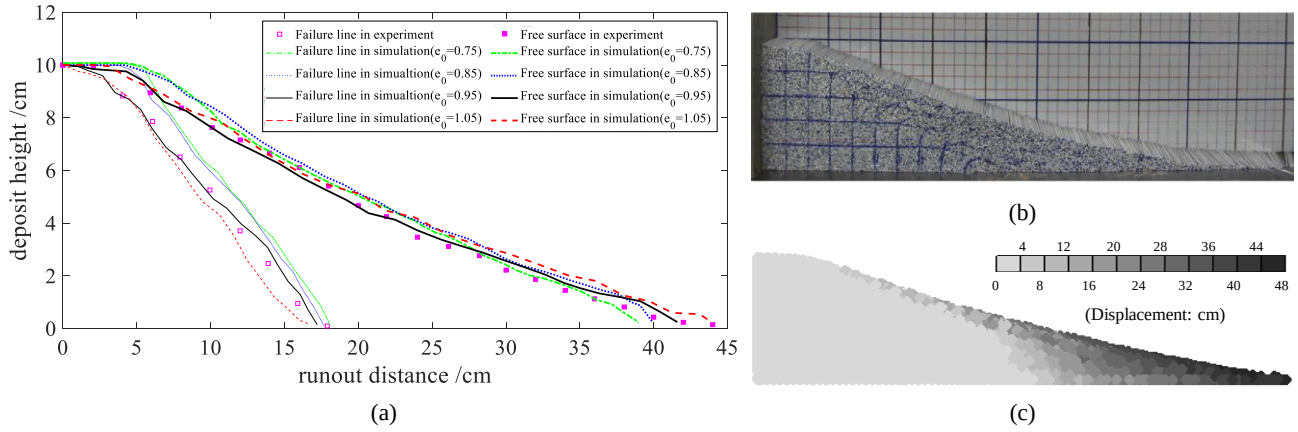

Figure 3.4 Rectangular channel soil collapse simulations and experimental data: (a) final free surfaces and failure lines for various initial void ratios (e_0=0.75, 0.85, 0.95, 1.05), (b) final deformed shaped of the column in the experiment, and (c) final deformed shaped of the column in the simulations with e_0=0.95

Figure 3.5 shows the numerical deformed shaped of column and the distribution of deviatoric plastic strain at different time steps. The movement takes place for approximately 0.6s.

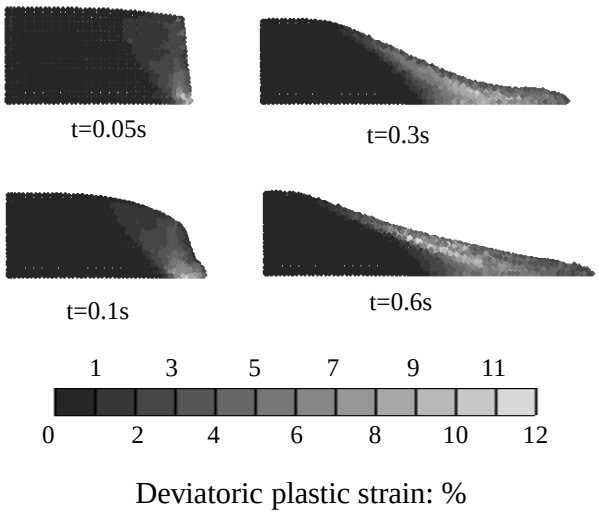

Figure 3.5 Rectangular channel soil collapse simulations: deformed shape and deviatoric plastic strain distribution at different time steps

3.4 2D column collapse simulations

3.4.1 Influence of aspect ratio

In order to have a better understanding on the granular column collapse and to further validate the adopted SPH-SIMSAND numerical approach, the two-dimensional column collapse experiences of Lube et al. (2005) with different initial aspect ratio are simulated hereafter. In the numerical model, the spatial discretization domain has the same dimensions as in the experiments of Lube et al. (2005), see Figure 3.6, where h_i is the initial height, d_i the initial basal length and $a=h_i/d_i$ the aspect ratio of the granular column. As in the experiments, six aspect ratios are simulated (a=0.5, 1.0, 1.5, 3.0, 7.0, 9.0) where the column initial basal length is taken constant and equal to 10 cm. The element size for all aspect ratios is 0.2cm. The total number of SPH particles varies from 31250 to 562500 for the different column aspect ratios, see Table 3.3.

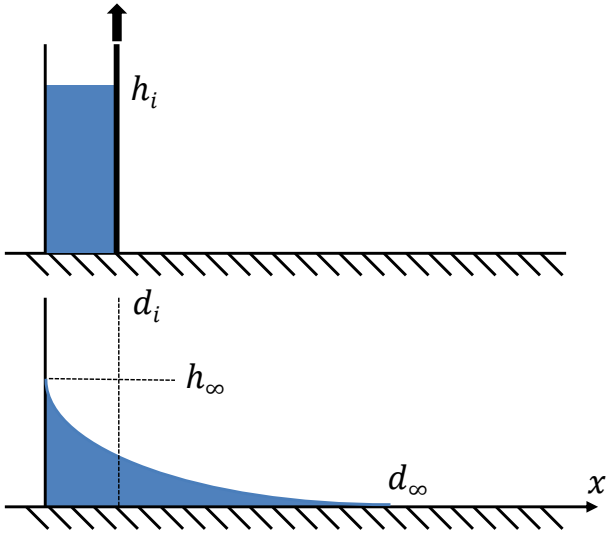

Figure 3.6 2D column collapse: discretization domain plane views

Table 3.3 2D column collapse: discretization parameters for all simulations

Aspect ratio a	Initial basal length d_i (cm)	Initial height h_i (cm)	Column size(cm^3)	Number of SPH particles
0.5	10	5	10×5×5	31250
1.0	10	10	10×10×5	62500
1.5	10	15	10×15×5	93750
3.0	10	30	10×30×5	187500
7.0	10	70	10×70×5	437500
9.0	10	90	10×90×5	562500

Three different aspect ratios (a = 0.5, 1. 5 and 7.0) are compared with the experimental results of Lube et al. (2005) in Figure 3.7, where the distribution of the deviatoric plastic strain can be seen.

A good agreement is observed in terms of deposit morphology. Furthermore, simulations captured the progressive collapsing process and more specifically:

(1) For a = 0.5: the outer region at the bottom flows and the length of the run-out region at the column foot increases. The inner region is less disturbed than for the other cases and a flat area remains at the top.

(2) For a = 1.5: the run-out distance at the bottom increases and a flat undisturbed area is created at the top during the initial stage. Finally, a cone tip is formed.

(3) For a = 7.0: an important degradation of the column height first happens. Then, the run-out distance at the column foot increases and the upper initially undisturbed surface begins to flow. Finally, a very large run-out distance with a cone tip is formed.

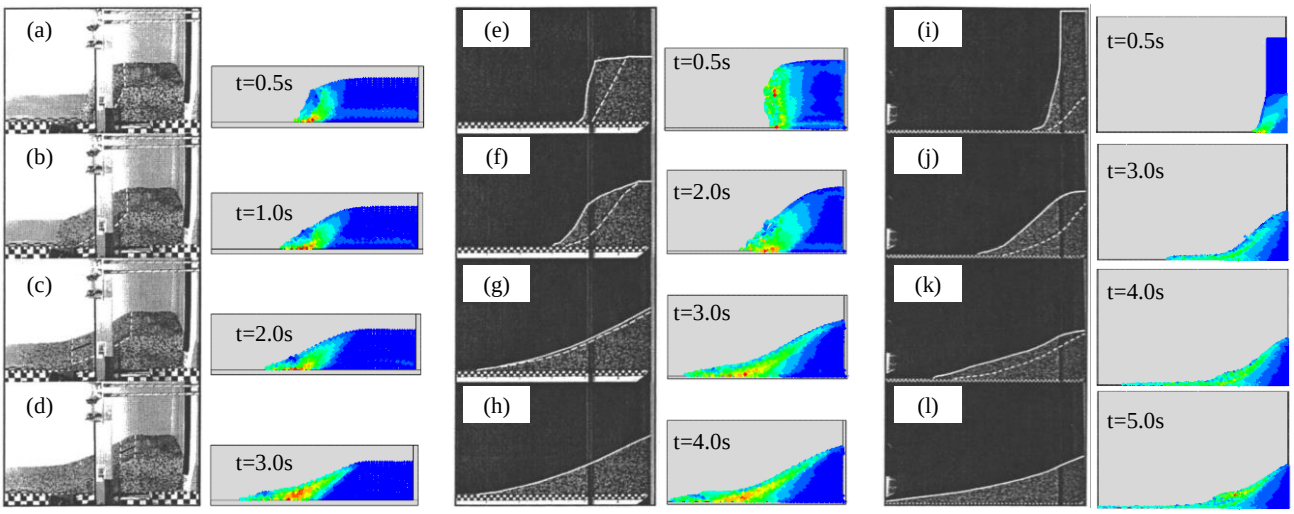

Figure 3.7 2D column collapse: comparison of progressive granular collapse between simulations and experiments for different aspect ratios (a-d) a = 0.5, (e-h) a = 1.5 and (i-l) a = 7.0

3.4.2 Flow description

Figure 3.8 shows the successive numerical granular collapse profiles for the three aspect ratios. Lube et al. (2004) distinguished three deposit morphologies based on the aspect ratio range: (1) a <0.74, (2) 0.74 < a <1.7 and (3) a >1.7. These distinctive flow processes are well captured by simulations:

For a = 0.5 (< 0.74): a lateral flow develops at the column foot and a flat undisturbed area remains at the top. The deposit height h_0 stays constant.

For 0.74 < a = 1.5 <1.7: the evolution of the lateral flow is accompanied by a small decrease of the initial height h0. A wedge shape is formed at the end.

For a = 7 >1.7: initially, the column height greatly decreases but the upper surface remains unchanged. Then, the lateral flow quickly develops. Simultaneously, the length of the upper surface decreases and a dome-like shape is formed. At the final stage, the run-out distance d_∞ is important and a wedge shape is formed at the top h_∞.

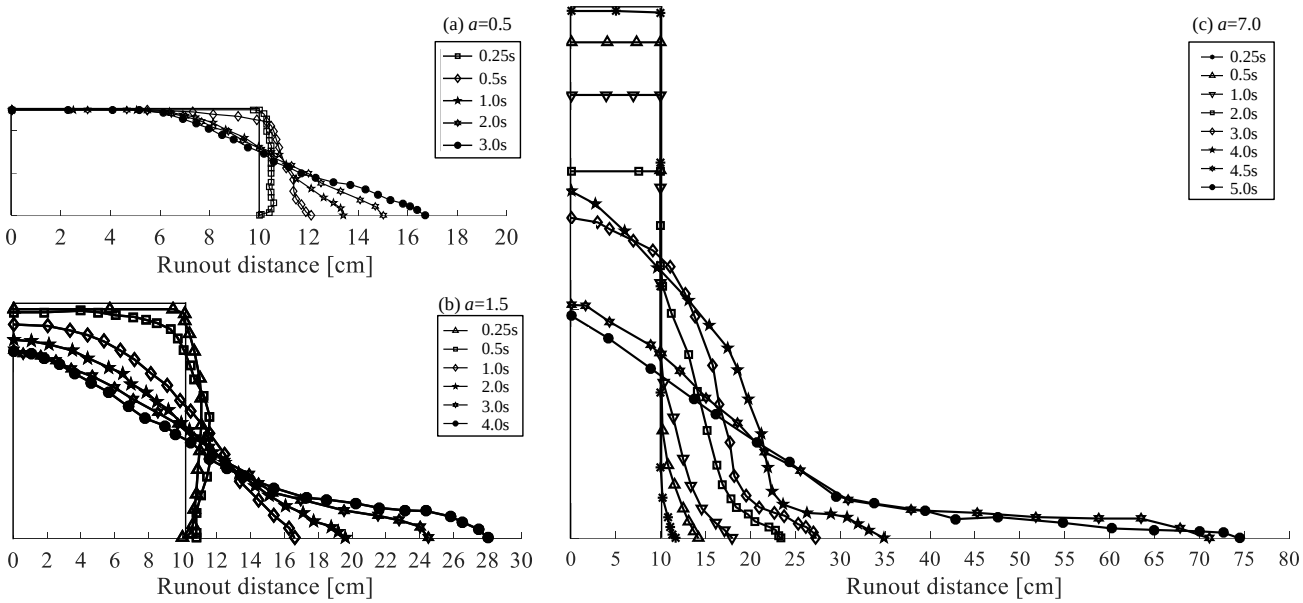

Figure 3.8 2D column collapse: numerical progressive column collapse profiles for different aspect ratios (a) a = 0.5, (b) a = 1.5 and (c) a =7.0

Figure 3.9 shows the comparison of plastic strain fields between simulations with different aspect ratios, where the smallest value of deviatoric plastic strain ε_d^p is coloured in black. The undisturbed stable area inside the granular column is characterized by a relatively small value of deviatoric plastic strain. For the cases a = 0.5, 1.0 and 1.5 only, an undisturbed trapezoid area develops on the upper free surface of the column. For the larger aspect ratios a = 3.0, 7.0 and 9.0, a triangle area is formed at the upper free surface and the repose angle presents an increasing trend.

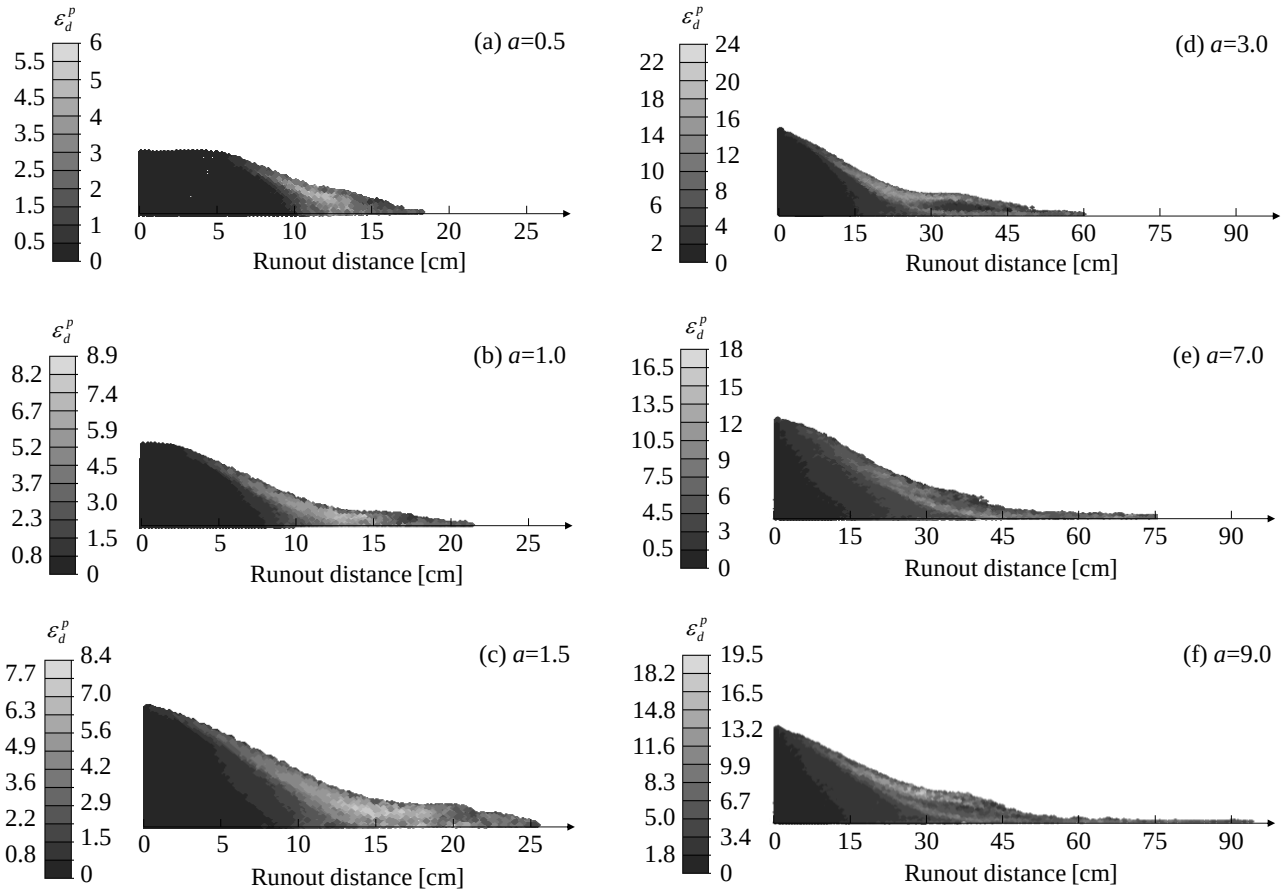

Figure 3.9 2D column collapse: side view of plastic deviatoric strain after collapsing for different aspect ratios (a) a = 0.5, (b) a =1.0, (c) a = 1.5, (d) a = 3.0 , (e) a = 7.0 and (f) a = 9.0

3.4.3 Influence of soil density

In order to study the influence of soil density, granular columns with four initial void ratios (e_0 = 0.75, 0.85, 0.95 and 1.05, corresponding to a unit weight of γ = 1.51, 1.43, 1.36 and 1.29 when G_s=2.65) and for six aspect ratios (a = 0.5, 1.0, 1.5, 3.0, 7.0 and 9.0) are simulated hereafter. The numerical results are compared with the best-fitting equations of Lube et al. (2005) in Figure 3.10. It can be seen, the numerical results are in agreement with the best-fitting equations for the normalized final run-out distance when e_0=0.95. Differences however appear for smaller initial void ratios, especially for the larger aspect ratios cases. The normalized final deposit height seems less sensitive to the soil density. However, the effect increases for the larger aspect ratios cases. The comparisons indicate that the deposit morphology (final run-out distance and final deposit height) depends not only the aspect ratio but also on the initial density. This is in agreement with results reported by the Discrete Element Method (Kermani et al. 2015).

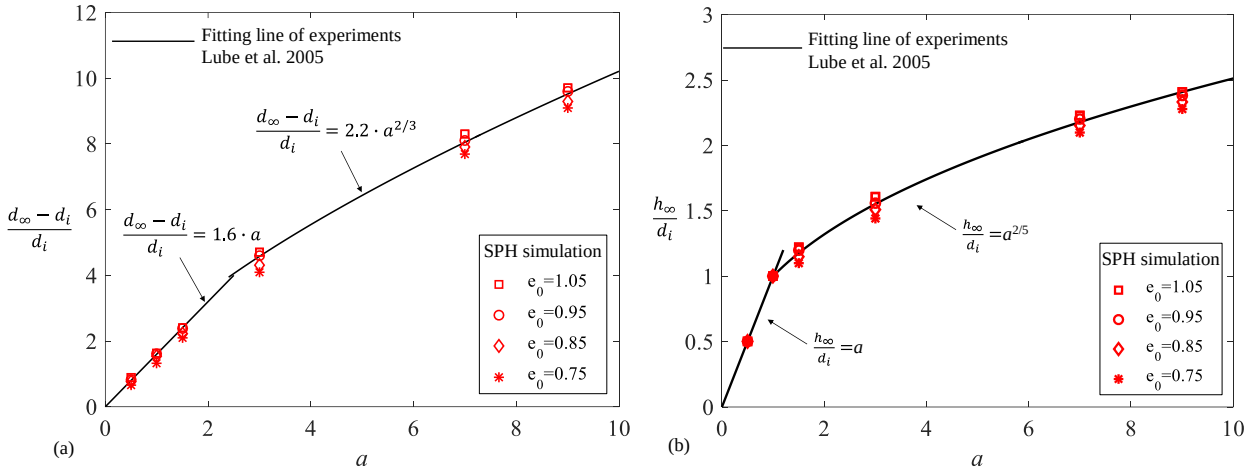

Figure 3.10 2D column collapse: comparison between the numerical simulations and the best-fitting equations of Lube et al. (2005) for different aspect ratios and initial void ratios (a) normalized final runout distance and (b) normalized final deposit height

Figure 3.11 presents the final deposit morphology of the numerical simulations with different initial void ratios. It can be seen that the final deposit morphology is sensitive to the initial void ratio or the soil density. For the cases of $a < 1.15$, the height of the circular undisturbed zone in the upper surface is maintained but its area decreases. The run-out distance increases with increasing initial void ratio (or decreases with decreasing initial soil density). For a higher column $a > 1.15$, the denser granular material causes shorter run-out distance and higher final deposited height. This result is in agreement with DEM simulations Kermani et al. (2015) and experiments Daerr and Douady (1999).

The SPH method combined with the critical state based SIMSAND model captures well the influence of void ratio (or soil density) on granular collapse. The different deposit morphologies for different void ratios with the same aspect ratio can be explained by stress-dilatancy. For a dense sand, a stronger interlocking force develops between the particles, a higher mobilized strength and finally a stable inner region is formed during collapse. A denser granular column corresponds to a bigger inclination of the slope surface, a more important deposit height and a smaller run-out distance.

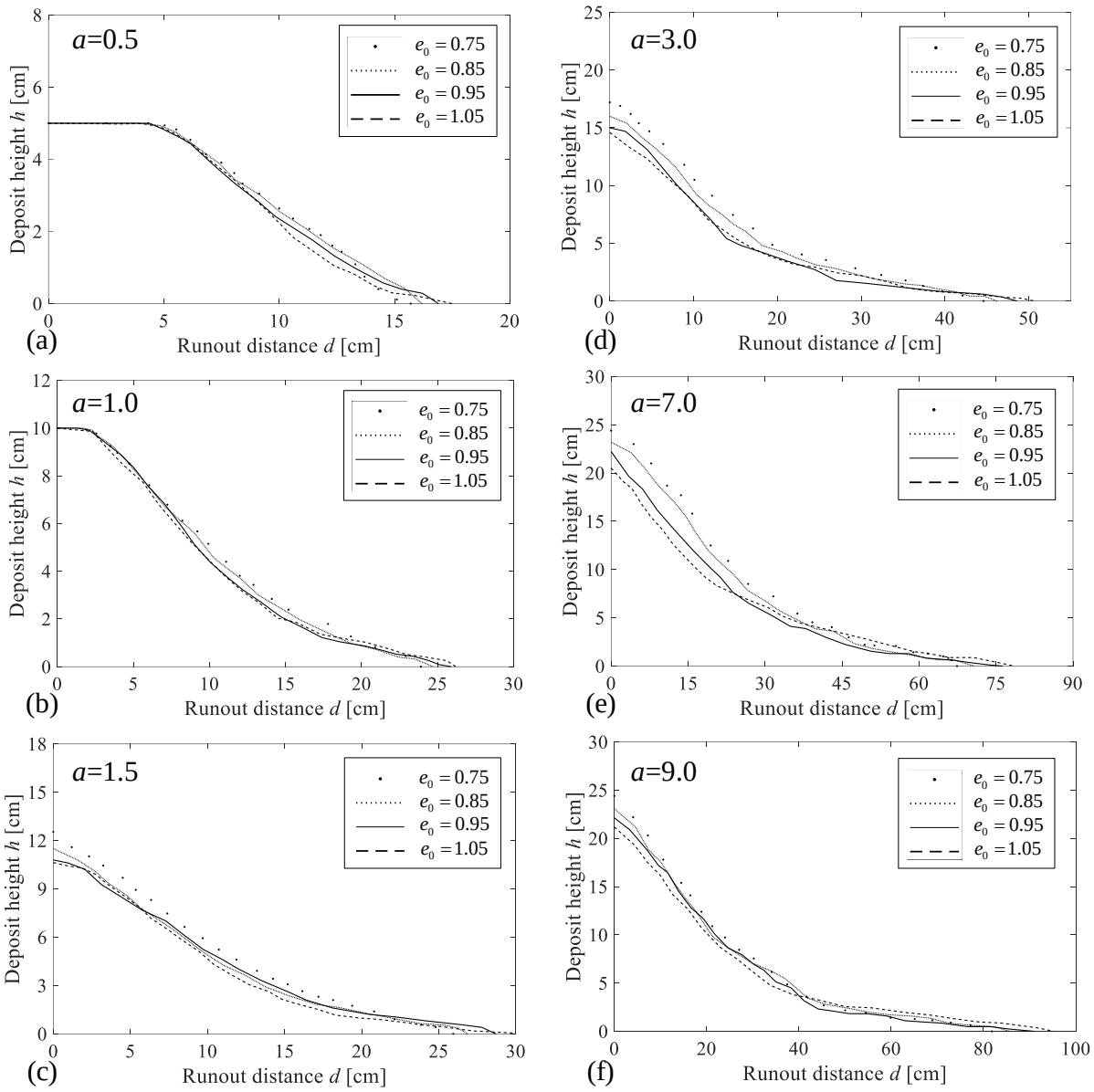

Figure 3.11 2D column collapse: influence of the initial void ratio on the final deposit morphology for (a) a = 0.5; (b) a = 1.0; (c) a = 1.5; (d) a = 3.0; (e) a =7.0; (f) a = 9.0

3.4.4 Monitoring collapse

The collapsing time t is normalised hereafter by the intrinsic critical time t_c that can be calculated from the initial height of the sand column $t_c = \sqrt{h_i/g}$ (Soundararajan 2015). Figure 3.12 and Figure 3.13 present the simulation results of the normalized run-out distance $(d_\infty - d_i)/d_i$ and the normalized deposit height h_∞/d_i with the normalized time t/t_c. All results present an "S-shape" curve with two successive stages, regardless the initial aspect and void ratios; an acceleration and then a deceleration stage starting close to $1.5t_c \sim 2.0t_c$. Collapse ceases approximately at $3.5t_c$.

The following conclusions can be made:

(1) For the same initial void ratio, a higher aspect ratio leads to a more important normalized run-out distance and deposit height.

(2) For the same aspect ratio, a denser sand (smaller initial void ratio) leads to a more important deposit height but to a shorter run-out distance in the same time scale.

(3) The normalized deposit height initially increases when the right boundary plate is lifted (Figure 3.13(a-c)). This uplift depends strongly on the soil density. A denser soil leads to a more important uplift. The reason for this is again the stronger interlocking between particles that develops more on a denser sand at initial shearing.

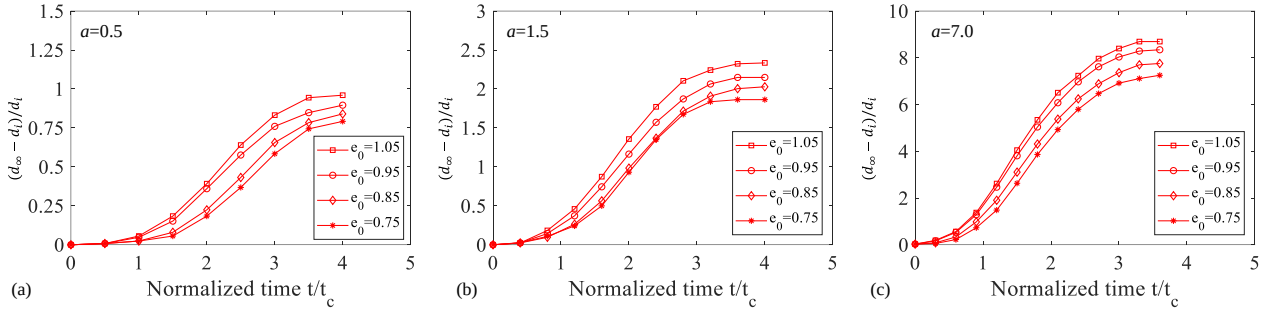

Figure 3.12 2D column collapse: evolution of the normalized runout distance for different aspect ratios and initial void ratios

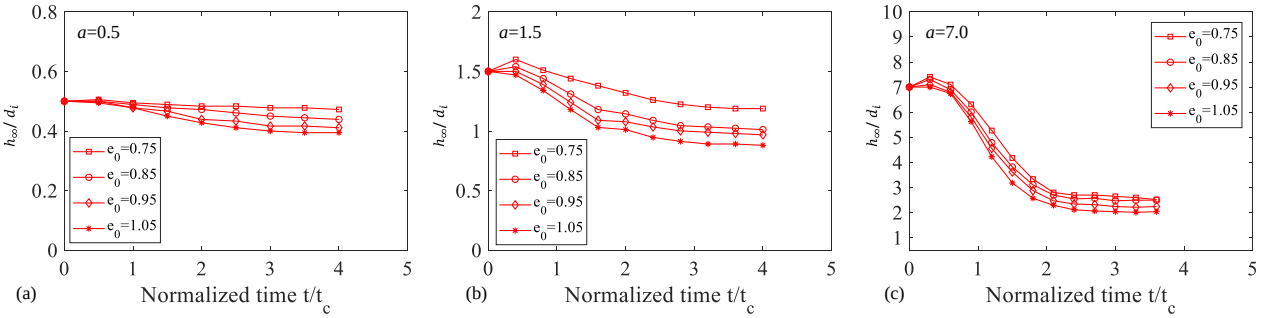

Figure 3.13 2D column collapse: evolution of the normalized deposit height for different aspect ratios and initial void ratios

3.5 Conclusions

A numerical investigation on granular collapse, based on the critical state soil model SIMSAND and the SPH method has been carried out. The validation was first provided by comparing experimental data from rectangular channel and two-dimensional column collapse tests. Then, the influence of the initial aspect ratio and the soil density was studied in details.

All comparisons show that the adopted numerical strategy is able to reproduce qualitatively and quantitatively the main behaviours of granular column collapse, i.e. free surface, failure line, the final deformed profile for the rectangular channel test, final run-out distance and deposit height. More specifically, when the initial soil density decreases the failure surface shrinks and the free surface enlarges. A lower initial void ratio generates a stronger interlocking force leading to a higher deposit height and a shorter run-out distance.

The combination of the SIMSAND model with the SPH method is able to reproduce granular collapse considering the influence of different aspect ratios and soil densities. It is therefore an effective computational tool for the analysis of real scale granular flow. The combination of the SIMSAND model with the SPH method being validated, the Combined Lagrangian-SPH method and the SIMSAND model are adopted in the next chapter to further study the failure envelope of a caisson foundation in sand.

Chapter 4 Numerical investigation on the evolving failure of caisson foundations: Combined Lagrangian - SPH technique, SIMSAND model

4.1 Introduction

The design of caisson foundations has recently become an important geotechnical challenge. Although caisson foundations have been used in the oil and gas industry for several decades (Tjelta 1995; 2001), they have been used for Offshore Wind Turbines since the early 21st century (Iskander et al. 2002; Villalobos et al. 2004; Houlsby et al. 2005; Nguyen-Sy and Houlsby 2005; Houlsby et al. 2006; Senders 2009; Villalobos et al. 2009). Providing a skirt, caisson foundations significantly improve the stiffness and the bearing capacity with the additional expense of a (minor) weight increase compared to classical surface foundations (Villalobos et al. 2003). A caisson foundation is lighter than a gravity platform jacket; nevertheless, the horizontal loads and moments are high in comparison to its weight.

For an optimum caisson foundation design in the offshore field it is necessary to consider the couplings between the vertical force (V), the horizontal force (H) and the bending moment (M). Previous research studies on the bearing capacity of caisson foundations in sand mainly focused in in-situ tests (Hogervorst 1980; Tjelta 1995; Houlsby et al. 2006), model test (Gottardi et al. 1999; Byrne and Houlsby 2001; Cassidy et al. 2002; Ibsen et al. 2013; Ibsen et al. 2014; Foglia et al. 2015) or finite element method simulations (Gourvenec 2008; Bransby and Yun 2009; Liu et al. 2014; Gerolymos et al. 2015; Ntritsos et al. 2015; Zafeirakos and Gerolymos 2016). The above experimental or numerical results can be used to construct simplified numerical strategies for design purposes, e.g. macroelements (Nova and Montrasio 1991; Montrasio and Nova 1997; Gottardi et al. 1999; Byrne and Houlsby 2001; Cremer et al. 2001; Cassidy et al. 2002; Grange et al. 2008; Salciarini and Tamagnini 2009; Li et al. 2016). Following the macroelement concept, the entire soil-foundation system is regarded as a single element with a constitutive law expressed in generalised variables following the plasticity or hypoplasticity theory. Compared to a conventional finite element approach, macroelements are simpler, faster and more robust but suitable only for specific foundation - soil configurations.

The definition of the failure surface is of paramount importance in the development a macroelement (Gottardi and Butterfield 1993; Houlsby and Cassidy 2002; Gourvenec and Randolph 2003; Gourvenec and Barnett 2011; Li et al. 2014) as it introduces the effects of combined loads for different loading levels. An investigation of the failure surface entirely based on model tests induces however important financial and computational costs (Byrne 2000; Nguyen-Sy 2005; Villalobos et al. 2010; Ibsen et al. 2013; Foglia et al. 2015). A timesaving and more economical approach is to use a combination of experiments and finite element method simulations. It is worth noting however that

the reliability of the numerical analysis depends on its ability to realistically reproduce the soil nonlinear behaviour.

The response of a caisson foundation in sand subjected to combined loading has been recently simulated with different constitutive models, such as a plasticity constitutive model governed by the Mohr-Coulomb failure criterion (Achmus et al. 2013; Liu et al. 2014; Zafeirakos and Gerolymos 2016), the NGI - ADP model with an anisotropic undrained shear strength failure criterion (Skau et al. 2018) and an elastoplasticity model called Hardening Small stain Soil model (HSS) which can reproduce basic macroscopic phenomena in the soil (Li et al. 2015). The calibration strategy of the soil parameters is also of great importance. Some studies adopt back calculations from experimental field tests or empirical formulas (Achmus et al. 2013; Zafeirakos and Gerolymos 2016), the representative soil strength profile of specific areas when the relevant soil parameters are not available (Liu et al. 2014; Skau et al. 2018) or triaxial tests and back analysis using the finite element method (Li et al. 2015). However, the full numerical analyses with different scales from laboratory to in-situ conditions including large deformation phases (e.g. CPT or caisson penetration for validations) have not been reported.

The Combined Lagrangian-SPH method (CLSPH) is adopted hereafter to consider large deformations. The SIMSAND critical state elastoplastic constitutive model is used to describe in a realistic way the sand characteristics, the evolving failure envelope and the influence of different soil parameters (density, friction angle, deformability and grain crushability). The SIMSAND soil parameters are calibrated from triaxial tests on Baskarp sand. The CLSPH-SIMSAND numerical model is then validated using a cone penetration test, model tests and a reduced scale field test. A large number of finite element simulations are then carried out to investigate the behaviour of a caisson foundation in sand subjected to different load combinations. In order to identify the failure envelope in the *H-M-V* space, radial displacement loadings are applied. Various factors affecting the shape and size of the failure envelope are considered, including soil density, friction strength, soil stiffness, grain breakage, foundation geometry and aspect ratio. The coupling relationships among geometry, aspect ratio and characteristic parameters of the failure envelope are quantified with a general equation. An analytical formula of the 3D failure surface is finally proposed, useful for design purposes and the development of macroelements.

4.2 Validation of the CLSPH-SIMSAND approach

4.2.1 Drained triaxial tests

The calibration of the constitutive model parameters can be carried out using the straightforward method from experimental results (Wu et al. 2017) or using optimization methods (Jin et al. 2016a,b; Yin et al. 2016b). In this study, the experimental results of conventional drained

triaxial tests on Baskarp sand (named Aalborg University Sand No 0) by Houlsby et al. (2005) are used to calibrate the SIMSAND model parameters. For the triaxial experiments, three void ratios (0.85, 0.70, 0.61) and nine stress levels (5kPa, 10kPa, 20kPa, 40kPa, 80kPa, 160kPa, 320kPa, 640kPa, 800kPa), 27 groups in total, were tested.

A typical value of Poison's ratio ν = 0.25 is assumed. The other two elastic parameters (K_0, n) are determined with an isotropic compression test (see Figure 4.1). The critical state line related parameters e_{ref}, λ, ζ are measured from the position of the critical states in the p'-e plane (Figure 4.2(d)). Other parameters are calibrated manually from tests on sand with a void ratio e_0=0.85 (Wu et al. 2017). All the calibrated parameters are summarized in Table 4.1. Using these values, additional tests (e_0=0.7, 0.61) are simulated demonstrating the good performance of the model (see Figure 4.2).

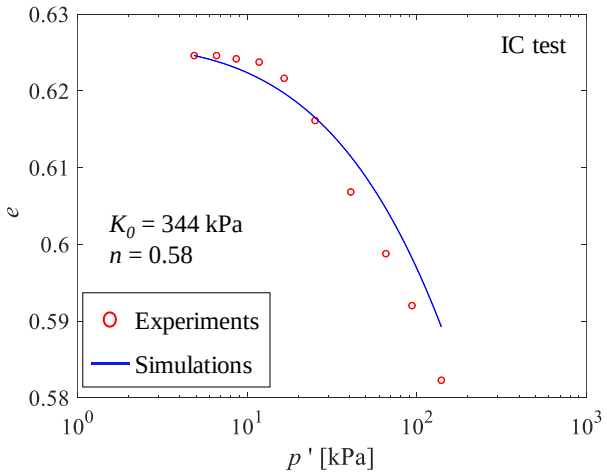

Figure 4.1 Calibration of the SIMSAND model parameters from isotropic compression test on Baskarp sand

Table 4.1 Calibrated parameters of the SIMSAND model for the Baskarp sand

Parameters	Name	Value
K_0	Referential bulk modulus (dimensionless)	344 (kPa)
υ	Poisson's ratio	0.25
n	Elastic constant controlling nonlinear stiffness	0.58
ϕ_μ	Critical state friction angle	35.1 (°)
e_{ref}	Initial critical state void ratio	1.25
λ	Constant controlling the nonlinearity of CSL	0.38
ξ	Constant controlling the nonlinearity of CSL	0.11
A_{d}	Constant of magnitude of the stress-dilatancy	0.45
k_{p}	Plastic modulus related constant	0.0034

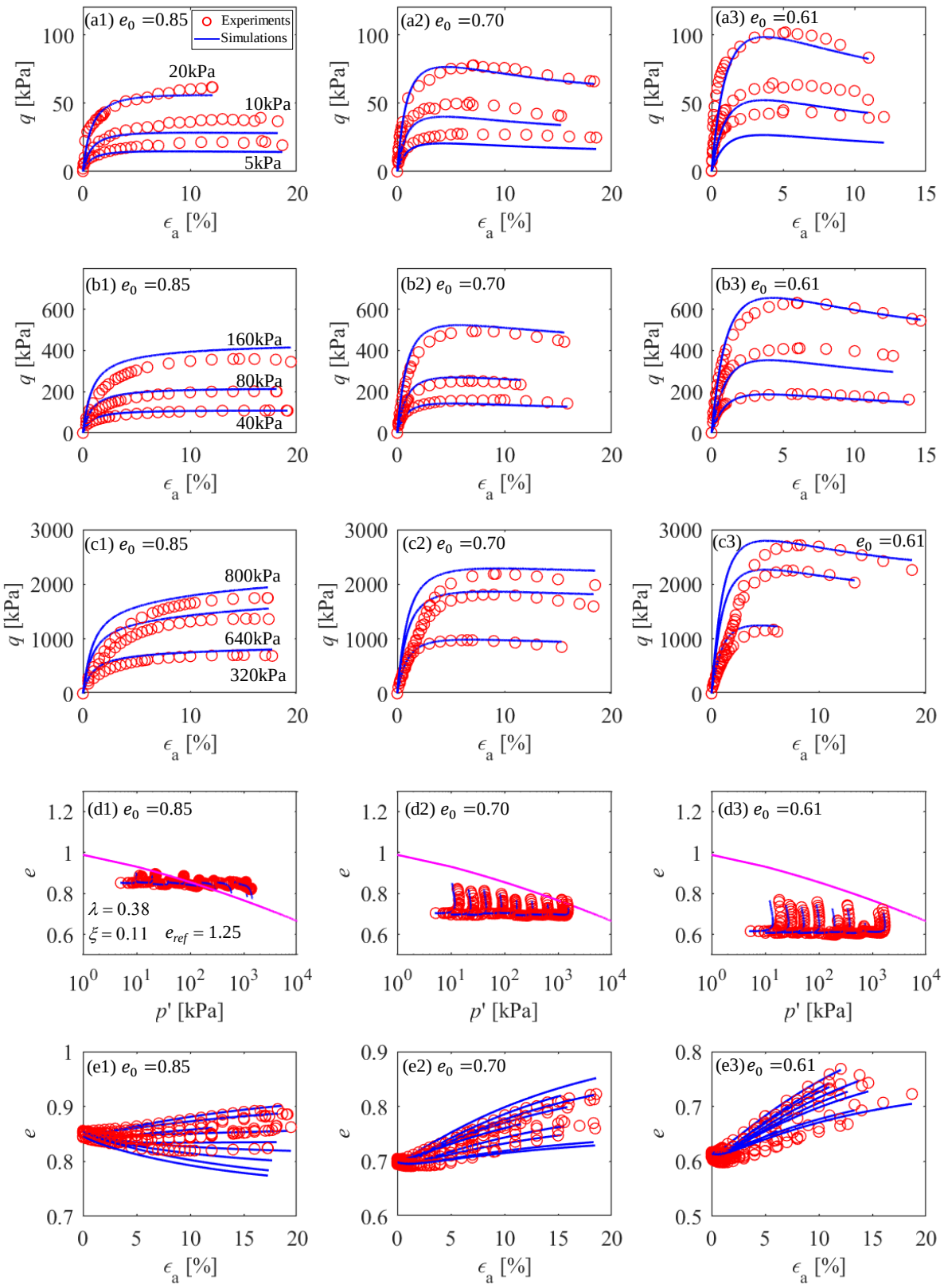

Figure 4.2 Calibration of the SIMSAND model parameters from drained triaxial tests on Baskarp sand with void ratios varying from 0.61 to 0.85 and stress levels from 5 to 800 kPa: (a-c) ratio of deviatoric stress to mean effective stress (*q/p'*) versus axial strain; (d) void ratio versus mean effective stress in semi-logarithmic scale; (e) void ratio versus axial strain

4.2.2 Indoor model tests

4.2.2.1 Experimental campaign

The experimental campaign of Foglia et al. (2015) simulated in chapter 2 with the CLSPH-Mohr Coulomb model is hereafter revisited with the CLSPH-SIMSAND approach.

4.2.2.2 Numerical model

The numerical discretization and the boundaries conditions are the same as in chapter 2. The SIMSAND constitutive model is adopted.

4.2.2.3 Validation using CPT tests

In order to validate the CLSPH-SIMSAND numerical model, the CPT test is simulated hereafter. Following Houlsby et al. (2006), the cone penetration applied velocity is taken equal to 5 mm/s. Assuming a typical soil-structure interface friction coefficient, a rigid Mohr-Coulomb type interface model is adopted and the interface model is applied on the entire (tip and shaft) surface of the cone, see Figure 4.3(a).

Figure 4.3(b) presents the simulation results and the comparison with four groups of CPT data, Foglia et al. (2015). A good agreement is generally observed which indicates that the CLSPH-SIMSAND model with calibrated material parameters performs in a satisfactory manner. The plastic deviatoric strain (SDV18), the void ratio (SDV1) and the mean effective stress (S Pressure, kPa) fields corresponding to a penetration of 400 mm are plotted in Figure 4.3(c)-(e). Results show reasonable distributions with an influence distance much smaller than the SPH domain.

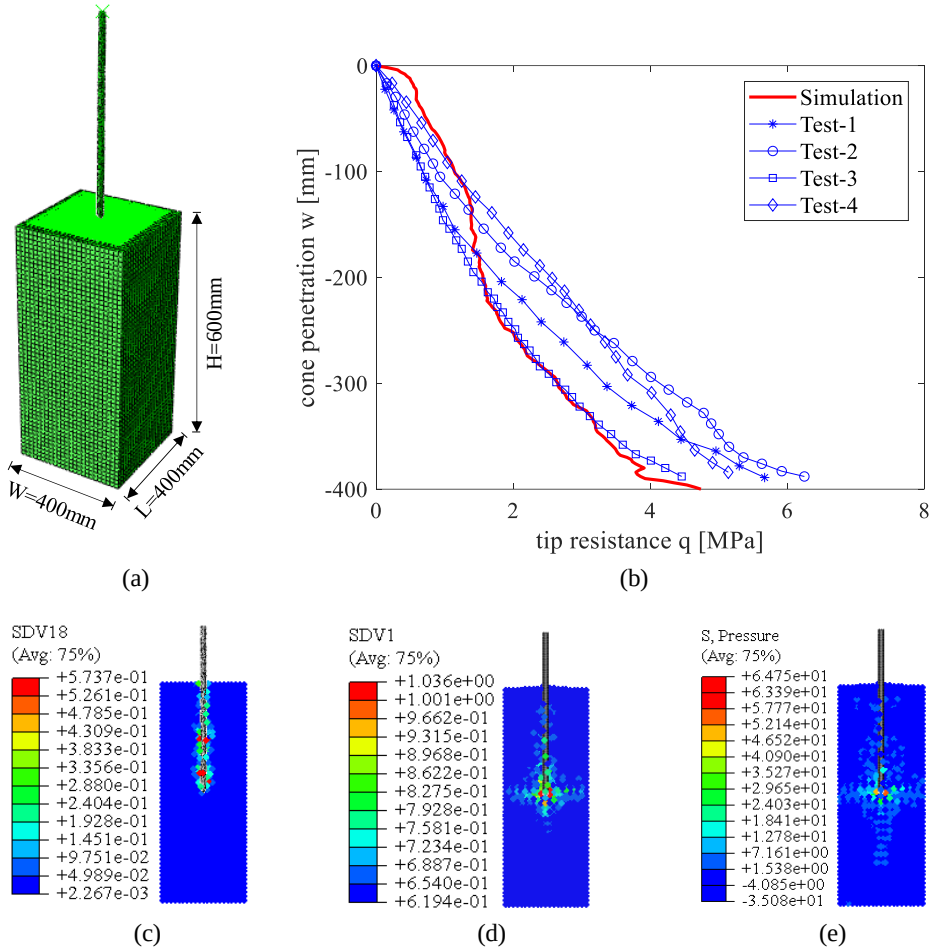

Figure 4.3 Results of the CPT test: (a) spatial discretization, (b) comparison of q-w curves between experiments and simulation, fields of (c) plastic deviatoric strain, (d) void ratio, (e) mean effective stress at the end of the CPT test, CLSPH-SIMSAND model

4.2.2.4 Validation using caisson foundation tests

The combined Lagrangian - SPH model is hereafter used to simulate a vertical penetration test with a vertical displacement control at a rate of 5 mm/s, and five tests at various dimensionally homogeneous moment to horizontal load ratios (*M/DH*=1.1, 1.987, 3.01, 5.82, 8.748) at a constant vertical load of 241 N. The horizontal displacements and the rotations are applied at the middle point of the caisson. A relatively slow displacement rate of 10 mm/s and a rotation rate of 0.5 degree/s are chosen to eliminate the dynamic effects. All monotonic loading paths are followed until the vertical bearing capacity (*VM*) or the horizontal capacity and moment capacity (*MR*) are reached.

The applied vertical force versus the vertical displacement for the penetration test is plotted in Figure 4.4. The results of five typical *M*/*DH* values (1.100, 1.987, 3.010, 5.820 and 8.748) are shown

in Figure 4.5. For all five cases the horizontal load (H) versus the horizontal displacement (U) and the dimensionally homogeneous moment (M/D) versus the rotations ($D\theta$) are plotted. A good agreement is obtained for all tests between experiments and simulations, showing the good performance of the CLSPH-SIMSAND approach.

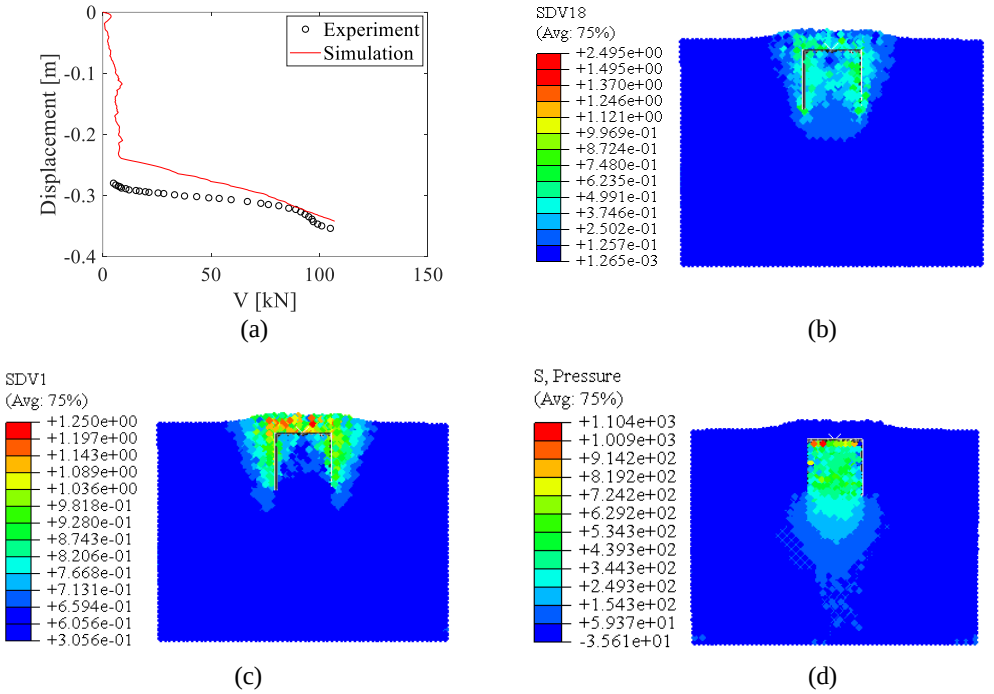

Figure 4.4 Results of the pure vertical penetration test: (a) comparison of vertical force - vertical displacement between experiment and simulation, fields of (b) plastic deviatoric strain, (c) void ratio and (d) mean effective stress at the end of the vertical penetration test, CLSPH SIMSAND model

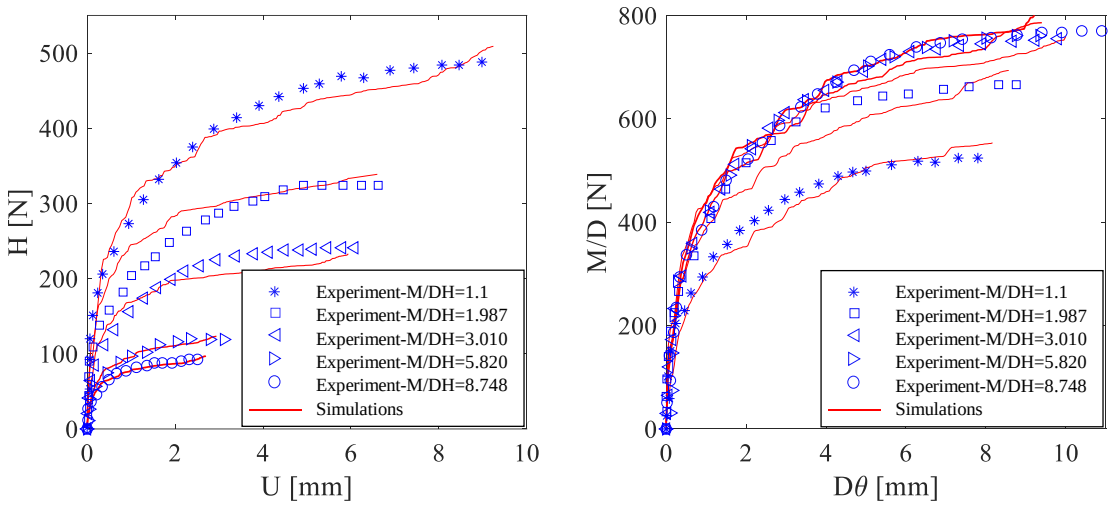

Figure 4.5 Comparison between simulated and experimental results for indoor model tests of a caisson foundation under combined loadings, CLSPH SIMSAND model

An extreme case is selected hereafter to check the behavior of the model under large deformations: the moment horizontal loading test *M/DH*=3.010. The plastic deviatoric strain (SDV18), the void ratio (SDV1) and the mean effective stress (S Pressure, kPa) fields at the end of loading are plotted in Figure 4.6(a)-(c). To further examine the progressive failure, a higher load is applied till the appearance of sliding at the bottom and the results are plotted in Figure 4.6(d)-(f). All results show reasonable field distributions with an influence distance, in the vertical and horizontal directions, much smaller than the SPH particles domain.

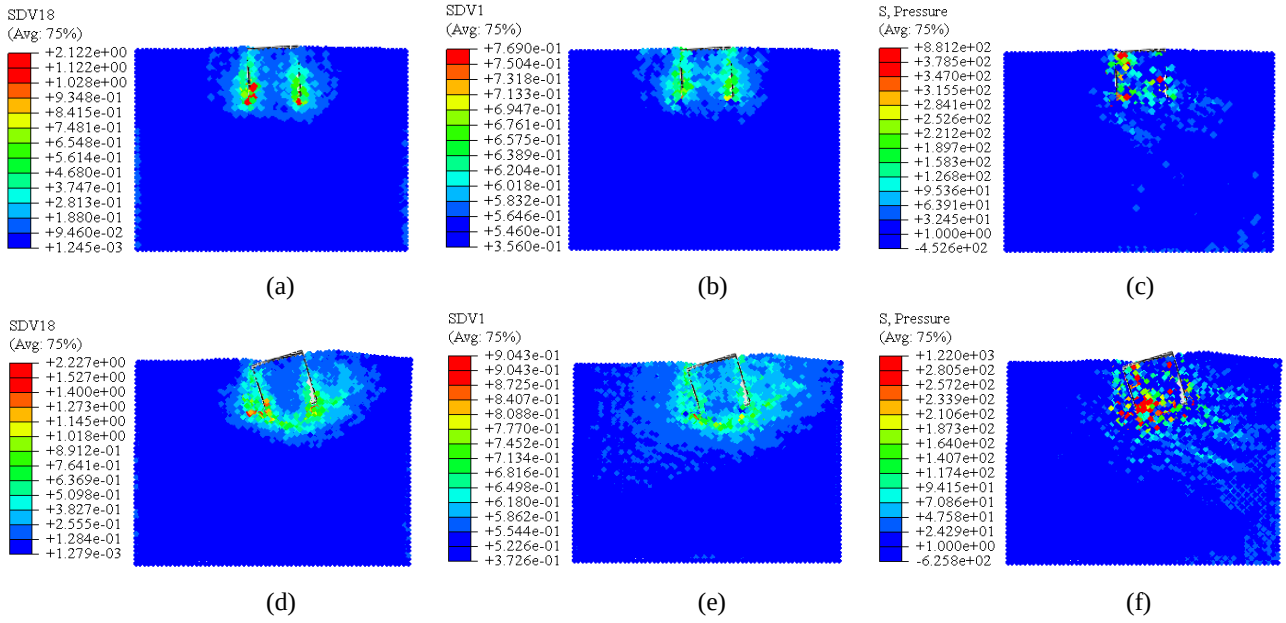

Figure 4.6 Simulated progressive failure of the *M/DH*=3.01 test; peak values and post-peak values: fields of (a,d) plastic deviatoric strain, (b,e) void ratio, (c,f) mean effective stress, CLSPH SIMSAND model

The failure envelopes on the *H:M/D* loading plane of Villalobos et al. (2010), Ibsen et al. (2014) and Foglia et al. (2015) plotted in Figure 4.7 and compared with the numerical simulations for the same vertical loading. A good agreement is again observed.

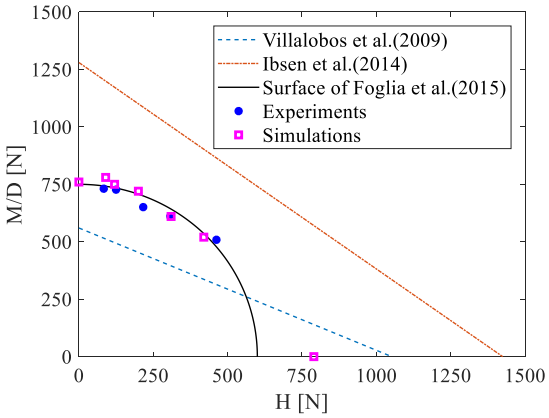

Figure 4.7 Comparison between simulated and experimental results; failure envelopes on the *H:M/D* loading plane, CLSPH SIMSAND model

4.2.3 Field test

4.2.3.1 Experimental setup

In order to further validate the numerical model, a reduced scale field test conducted by Houlsby et al. (2005) is simulated hereafter. A steel caisson with an outer diameter of 2m and a skirt length of 2m was tested. The skirt was made of steel plate 12mm thick and the caisson was installed in a shallow pond near the sea to model a bucket foundation. The load eccentricity *h* and vertical load *V* were 17.4m and 37.3kN, respectively. The caisson was installed in dense Baskarp sand area with unit weight 19.5kN/m^3 and specific gravity 26.5kN/m^3 (e_0=0.549) as indicated by Ibsen et al. (2005). The test contained three phases: installation, loading and dismantling. For the loading phase, an old tower from a wind turbine was mounted on top of the caisson. The caisson was loaded by pulling the tower horizontally with a wire. The combined loading (*H, M*) was controlled by changing the tower height.

4.2.3.2 Numerical model

The caisson is modelled using rigid hexahedron elements with the same dimensions and thickness as in the experiment (see Figure 4.8), while the behavior of the sand is reproduced with the SIMSAND model. The interface behavior between the caisson and the soil is modelled with a classical Coulomb model, where the tangential frictional stress is assumed proportional to the normal stress. Large deformations and geometric non-linearities are considered. The modelling strategy is similar to that of the indoor model tests (combined Lagrangian - SPH model).

The calculation domain is composed of two parts: the inner SPH domain and the outer Lagrangian domain. The SPH domain has a length of 10m (horizontal direction), a height of 12m and a total number of 106840 particles. The Lagrangian part is discretized with 32670 hexahedral elements. The SPH domain interacts with the Lagrangian finite element domain via contact interfaces that can open and close (Documentation 2010). More specifically and due to the lack of experimental data for the limit stress in the tangential direction, no threshold (τ_{max}) on the tangential frictional stress is adopted. The contact behavior between the caisson and the soil is characterized by a friction coefficient $\mu = \tan(\phi_c/2) = 0.32$, where the soil critical friction angle is $\phi_c = 35.1°$. A penalty algorithm is adopted for the contact behavior (Hibbitt et al. 2001). The horizontal displacements of the lateral sides are constrained as well as the translational degrees of freedom at the bottom. The different parameters used for the simulation are summarized in Table 4.1.

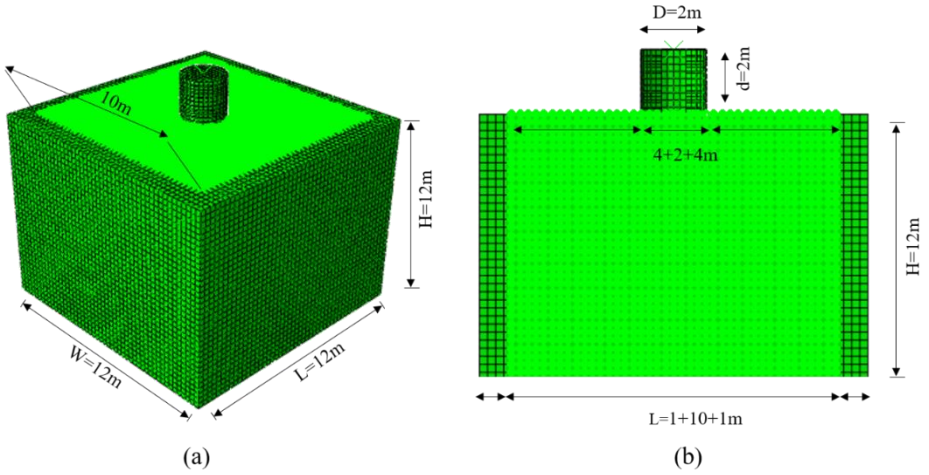

Figure 4.8 Combined Lagrangian-SPH model for the field test: (a) 3D mesh, and (b) middle cross section

4.2.3.3 Validation using caisson foundation tests

A moment-rotation test on the 2×2 m caisson is first considered to further prove the robustness of the CLSPH-SIMSAND approach (see Houlsby et al. (2005)). A relatively slow displacement rate of 10 mm/s and a rotation rate of 0.5 degree/s are applied to eliminate dynamic effects. Numerical results are compared with the experimental results in Figure 4.9. The performance of the model is again satisfactory. The numerical model reproduces correctly not only the moment evolution but also the bearing capacity of the caisson.

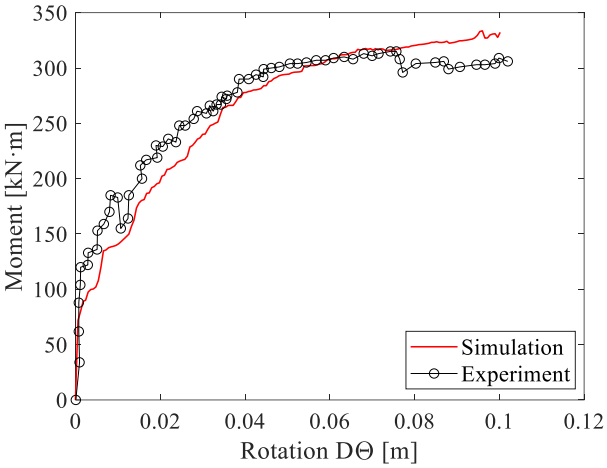

Figure 4.9 Comparison between simulated results and field measurements: moment *M* and rotation *Dθ* curve, CLSPH SIMSAND model

An extreme case is shown hereafter to analyze the progressive failure of the field test. The simulation is composed of two steps: the caisson foundation is first installed to the specified depth; then, a displacement rate of 10mm/s and rotation rate of 0.5 degree/s are applied up to the ultimate strength. The plastic deviatoric strain (SDV18), the void ratio (SDV1) and the mean effective stress (S Pressure, kPa) fields are shown in Figure 4.10 for the different phases. It is obvious that the area of these three variables increases with increasing applied displacement. The peak value also increases with time. The CLSPH-SIMSAND approach again successfully reproduces the progressive failure of the caisson foundation.

	deviatoric plastic strain	void ratio	mean effective stress
(a)	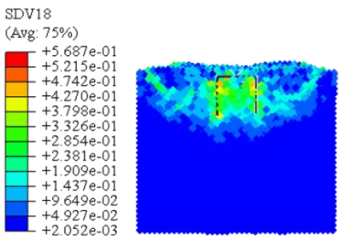	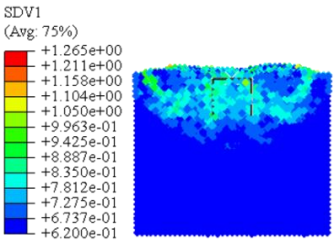	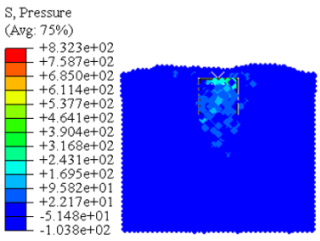
(b)	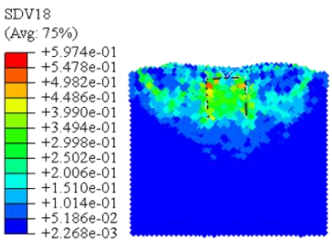	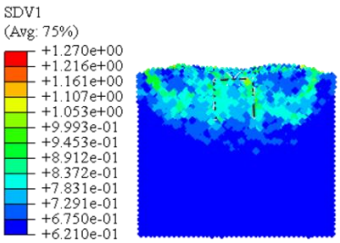	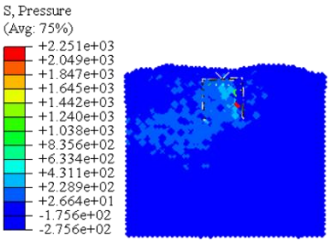

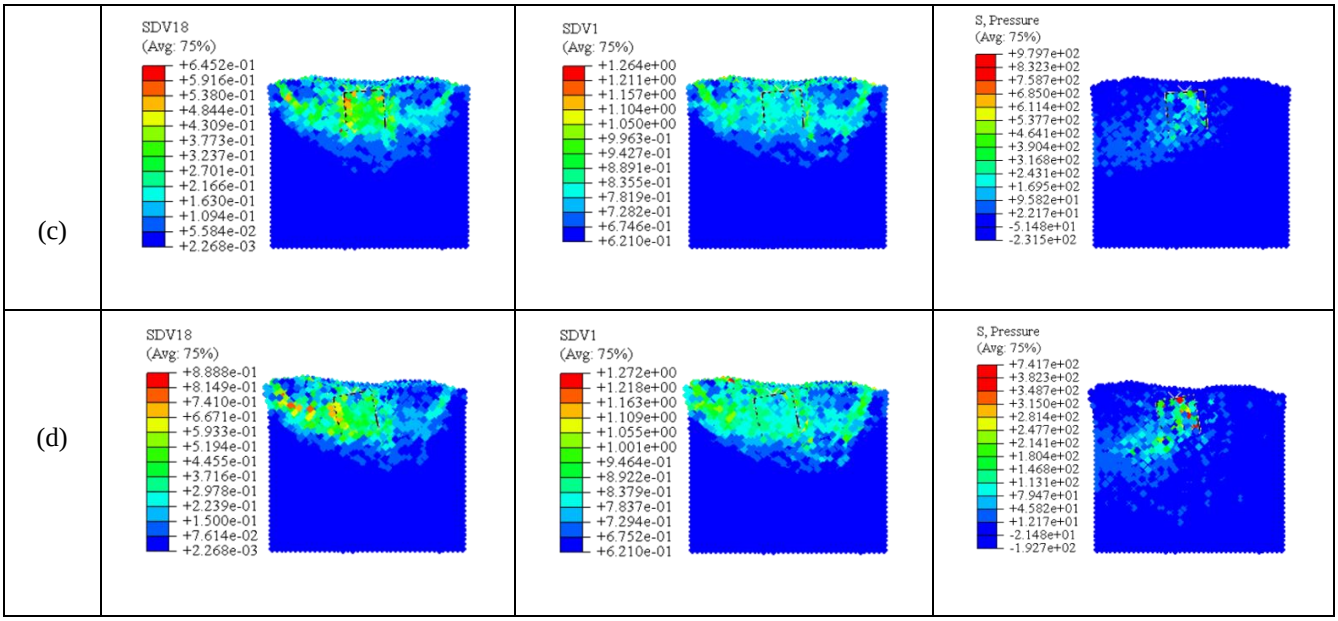

Figure 4.10 Simulated results of the field test at different phases: (a) end of penetration, (b) ½ of the peak values of the forces, (c) peak values of the forces, and (d) post-failure stage, CLSPH SIMSAND model.

In the following and based on the previous satisfactory validation results, the CLSPH-SIMSAND approach is adopted to numerically reproduce the *H-M-V* failure envelope of a caisson foundation for different soil properties and foundation geometries.

4.3 Numerical study of the failure envelope in *H-M* plane

4.3.1 Loading procedure

In order to identify the failure envelope of a foundation, Gottardi et al. (1999) proposed to follow two loading control paths : (1) *Swipe tests* in which a vertical displacement is first applied to the foundation up to a certain level of vertical force, and then an increasing horizontal displacement under a constant vertical displacement; (2) *Radial displacement tests* in which the ratio between the applied displacements or the combined rotation-displacement increments is kept constant.

In the following, numerical radial displacement tests are adopted as the main loading control. The sign conventions for the loads (horizontal force, vertical force and bending moment) applied on the Loading Reference Point (LRP) of the caisson foundation are presented in Figure 4.11. The foundation model has an outer diameter (D) of 2m, a skirt length (L) of 2m, and a lid and skirt thickness (t) of 12mm. The main goal of this study being the evaluation of the bearing capacity of the

caisson foundation, the possible upper structures (e.g. wind turbine and superstructure) are not discretized.

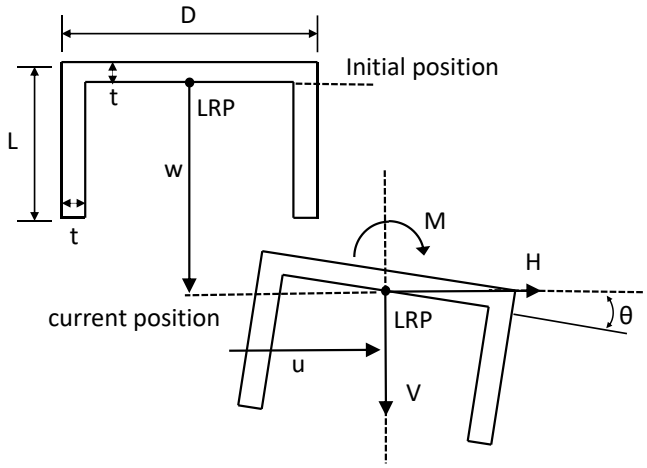

Figure 4.11 Loading and displacement conventions for a caisson foundation

Offshore Wind Turbine caisson foundations are relatively light, with a typical mass of 600t (vertical deadload 6MN) (Houlsby et al. 2005). The horizontal and overturning moment bearing capacities are therefore important for the design. To investigate the form of the failure surface in the *H-M* plane, different loading paths are applied hereafter on the LRP of the caisson. As shown in Figure 4.12, a constant vertical load is imposed up to a specified value $\chi = V_i/V_0$ (V_0 being the maximum load). Then, radial displacement loadings are applied considering a constant ratio between the combined rotation-displacement increments. The value of the displacement is large enough to ensure that the maximum strength is reached. In the following $\chi = 0$ refers to an actual load factor of $\chi \leq 0.01$(only the caisson self-weight is considered).

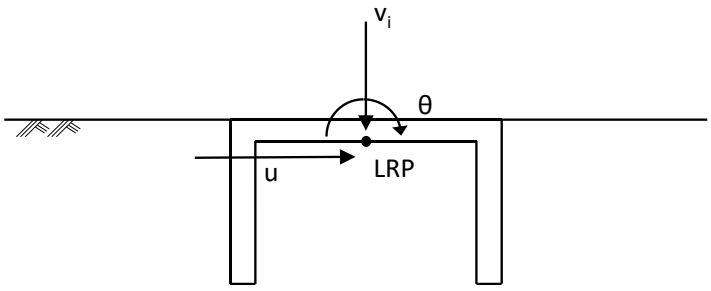

Figure 4.12 Schematic plot of radial displacement control

Figure 4.13 illustrates the way chosen to determine the bearing capacity; the ultimate bearing capacity is defined by the ends of loading paths.

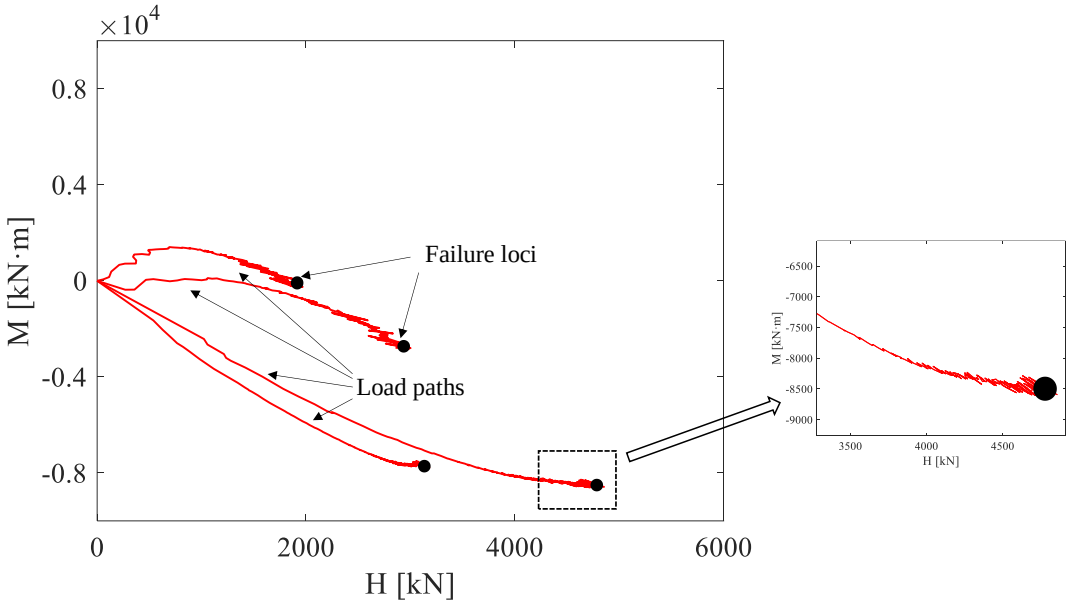

Figure 4.13 Determination of a failure point (the ends of loading paths)

Examples of load paths in the *H-M* plane from the numerical radial displacement tests are shown in Figure 4.14. The ratio between the increments of the rotation θ and the horizontal displacement u is constant ($\delta\theta/\delta u \equiv$ constant), which implies a straight loading path (Figure 4.14(a)). By connecting the values at the end of the different load paths, the complete failure envelope is obtained, as shown in Figure 4.14(b) and for different vertical load levels Figure 4.15.

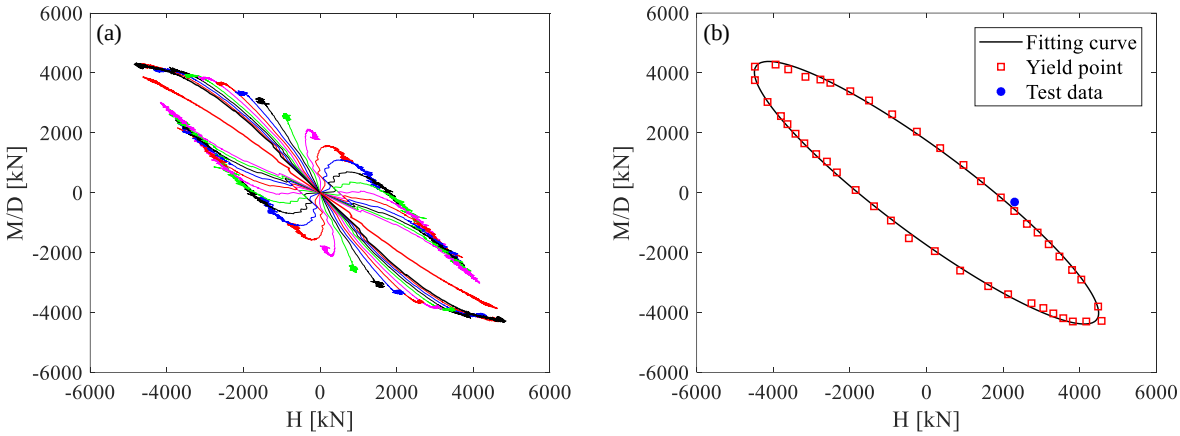

Figure 4.14 Numerical results of radial displacement control tests in the *H-M* plane: (a) load paths, and (b) failure surface, CLSPH SIMSAND model

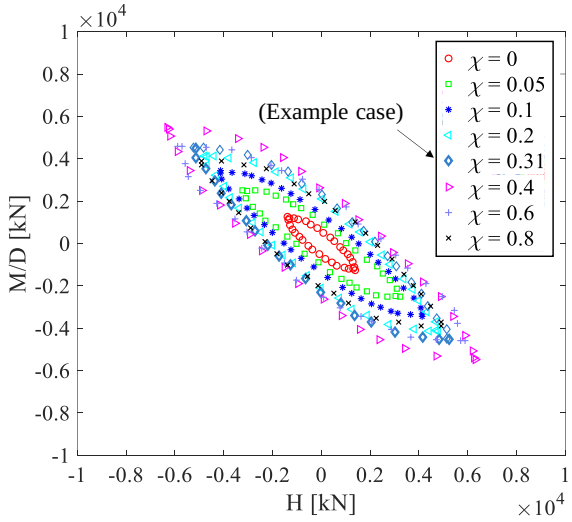

Figure 4.15 Failure envelopes at different vertical load levels in the *H-M* plane, CLSPH SIMSAND model

Some general results are summarized below:

(1) the failure envelopes of caisson foundations in sand are of inclined elliptical shape;

(2) the presence of bending moment has a significant influence on the horizontal bearing capacity depending on the loading direction.

4.3.2 Influence of soil properties

The influence of various soil parameters - soil density, friction strength, soil stiffness and grain breakage - on the failure envelope of a caisson foundation in sand is studied hereafter.

Four initial void ratios (e_0 = **0.62**, 0.67, 0.73 and 0.80, corresponding to a relative density D_r = 80%, 60%, 40% and 20%), four critical state friction angles (ϕ_c = 25°, 30°, **35.1°**, 40°), four soil stiffness constants (k_p = 0.01, **0.0034**, 0.001, 0.0005; the bigger value represents the smaller stiffness) and four grain breakage constants (C_a & C_b = **0 & 0**, 2500 & 4, 7000 & 7, 12000 & 10) are adopted for the simulations. Note that the set e_0 = 0.62, ϕ_c = 35.1°, k_p = 0.0034, C_a = 0 and C_b = 0 corresponds to the Aalborg University Sand No 0 mentioned above. The grain breakage related constants "C_a & C_b = 2500 & 4, 7000 & 7, 12000 & 10", corresponds to different crushabilities of a hypothetical sand (Jin et al., 2018). Bold letters are used to identify the original parameter group values corresponding to the field test presented in section 4.2.3. In order to identify the influence of each property, only the related input parameters are changed for the numerical calculations while the other parameters are kept constant, see Table 4.1. Three characteristic measures are used to describe

the shape and size of the envelope in *H-M* space. The length of the long axis *a*, the short axis *b* and the rotation angle *Ø,* see Figure 4.16.

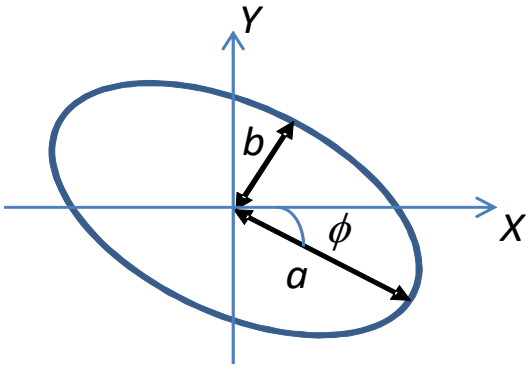

Figure 4.16 Schematic plot of the failure envelope and definitions of the characteristic measures *a*, *b* and *Ø*

Figure 4.17 presents the original form and the fitting curve of failure envelopes for varying soil densities in the *H-M* plane. It is worth noting that the obtained failure envelope excluded the field case simulated with the original parameter group (marked in bold). For increasing soil density, the size of the failure envelope expands. In other words, the horizontal and bending moment capacities improve with increasing soil density. A linear relationship can be observed in logarithmic scale between the parameter *a* and the soil relative density D_r, Figure 4.17(d).

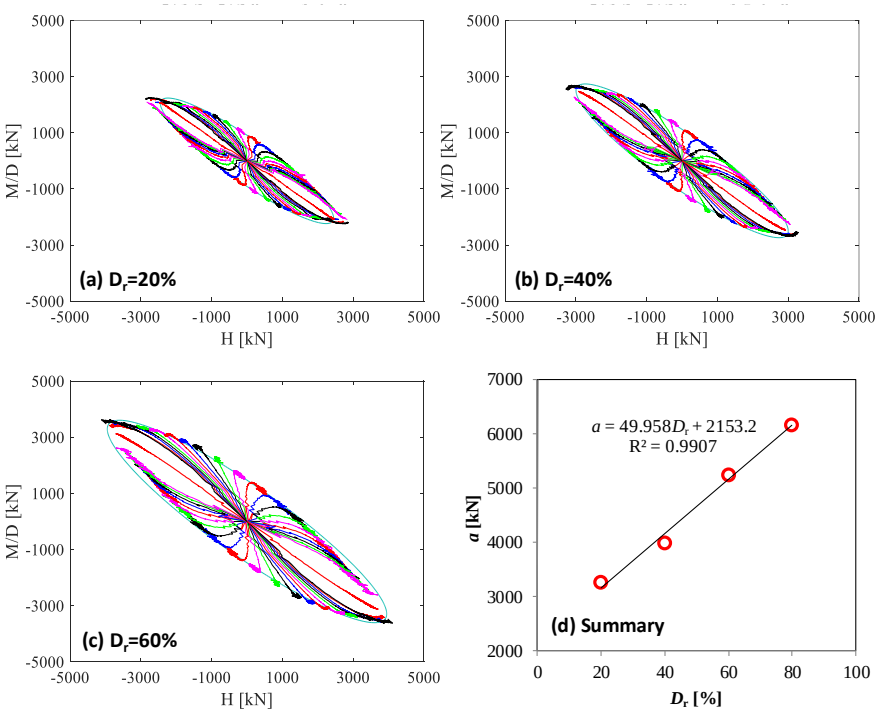

Figure 4.17 Failure envelopes in the *H-M* plane for different relative sand densities: (a) D_r = 20%, (b) D_r = 40%, (c) D_r = 60%, and (d) correlation between the ellipse size *a* and D_r, CLSPH SIMSAND model

A similar conclusion is obtained regarding the soil friction strength and the stiffness parameters, Figure 4.18 and Figure 4.19. With increasing critical friction angle and soil stiffness, the size of the failure envelope increases. The corresponding asymptotic equations are again linear, implying that the bearing capacity of a caisson foundation improves linearly in logarithmic scale with increasing soil friction strength and soil stiffness.

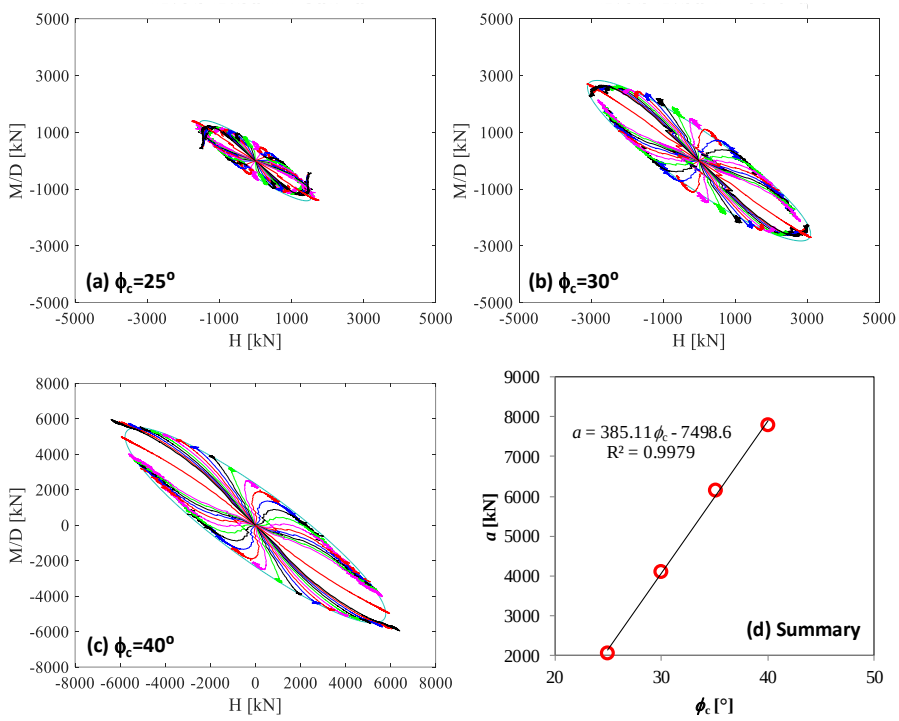

Figure 4.18 Failure envelopes in the *H-M* plane for different sand critical friction angles: (a) ϕ_c = 25°, (b) ϕ_c = 30°, (c) ϕ_c = 40°, and (d) correlation between the ellipse size a and ϕ_c, CLSPH SIMSAND model

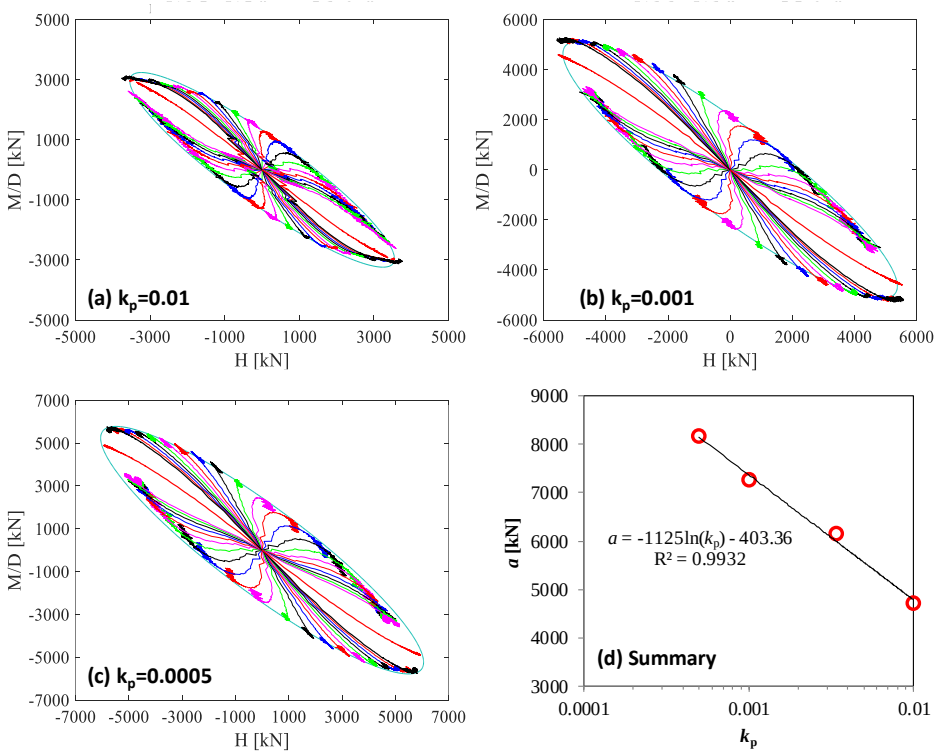

Figure 4.19 Failure envelopes in the *H-M* plane for different relative sand densities: (a) D_r = 20%, (b) D_r = 40%, (c) D_r = 60%, and (d) correlation between the ellipse size *a* and D_r, CLSPH SIMSAND model

The horizontal and bending moment bearing capacities decrease when considering grain breakage (see Figure 4.20). The most significant attenuation occurs for very easily crushable sand (e.g. parameters of Dog's bay sand by Jin et al., 2018). Finally, it should be noted that the short axis *b* presents a similar linear trend for different soil properties. On the other hand, the influence of the soil properties on the inclination $\emptyset$ of the bearing capacity diagrams is negligible ($\emptyset$ remains constant and equal to 42°).

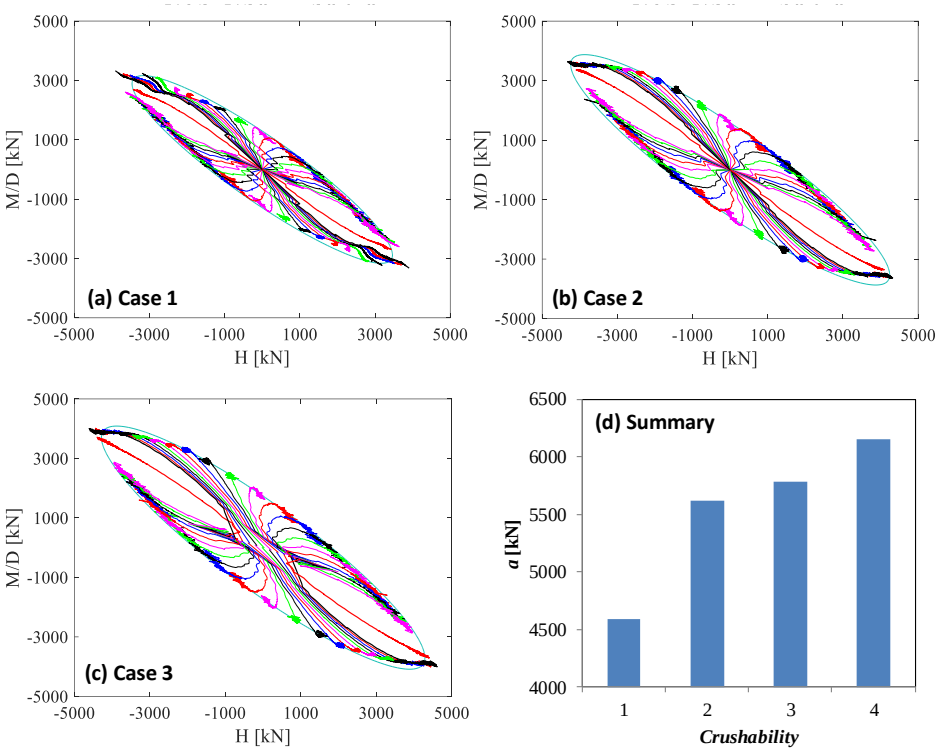

Figure 4.20 Failure envelopes in the *H-M* plane for different sand grain crushabilities: (a) easy crushing, (b) medium crushing, (c) hard crushing, and (d) ellipse size *a* versus crushability, CLSPH SIMSAND model

4.3.3 Influence of the caisson foundation size for the same aspect ratio L/D

Previous research works on the failure envelope of caisson foundations mainly focused on model tests on a small scale (Byrne 2000; Houlsby 2005; Villalobos Jara 2006; Ibsen et al. 2013; Foglia et al. 2015). In order to identify the failure envelopes for a full range of caisson sizes, four conventional caisson size aspect ratios (L/D = 0.5, 0.75, 1.0, 2.0) are selected for the simulations presented hereafter. L and D range from 1m to 20m, details are listed in Table 4.2. The simulation marked in bold (2×2m) is the field case simulated in the section 4.2.3.

Table 4.2 Geometry size configurations

L/D = 0.5	L/D = 0.75	L/D = 1.0	L/D = 2.0
1×2m	1.5×2m	**2×2m**	2×1m
2×4m	3×4m	4×4m	4×2m
4×8m	6×8m	8×8m	8×4m
8×16m	12×16m	16×16m	16×8m
10×20m	15×20m	20×20m	20×10m

The failure envelopes for different caisson sizes *L/D* in the *H-M* plane are summarized in Figure 4.21(a)-(c), the simulation results of the case *L/D* = 0.75 are presented later on (in the section 4.3.5). As the variations of the horizontal bearing capacity and the bending moment strength are of the order of four to five, a normalized presentation is adopted in the figures.

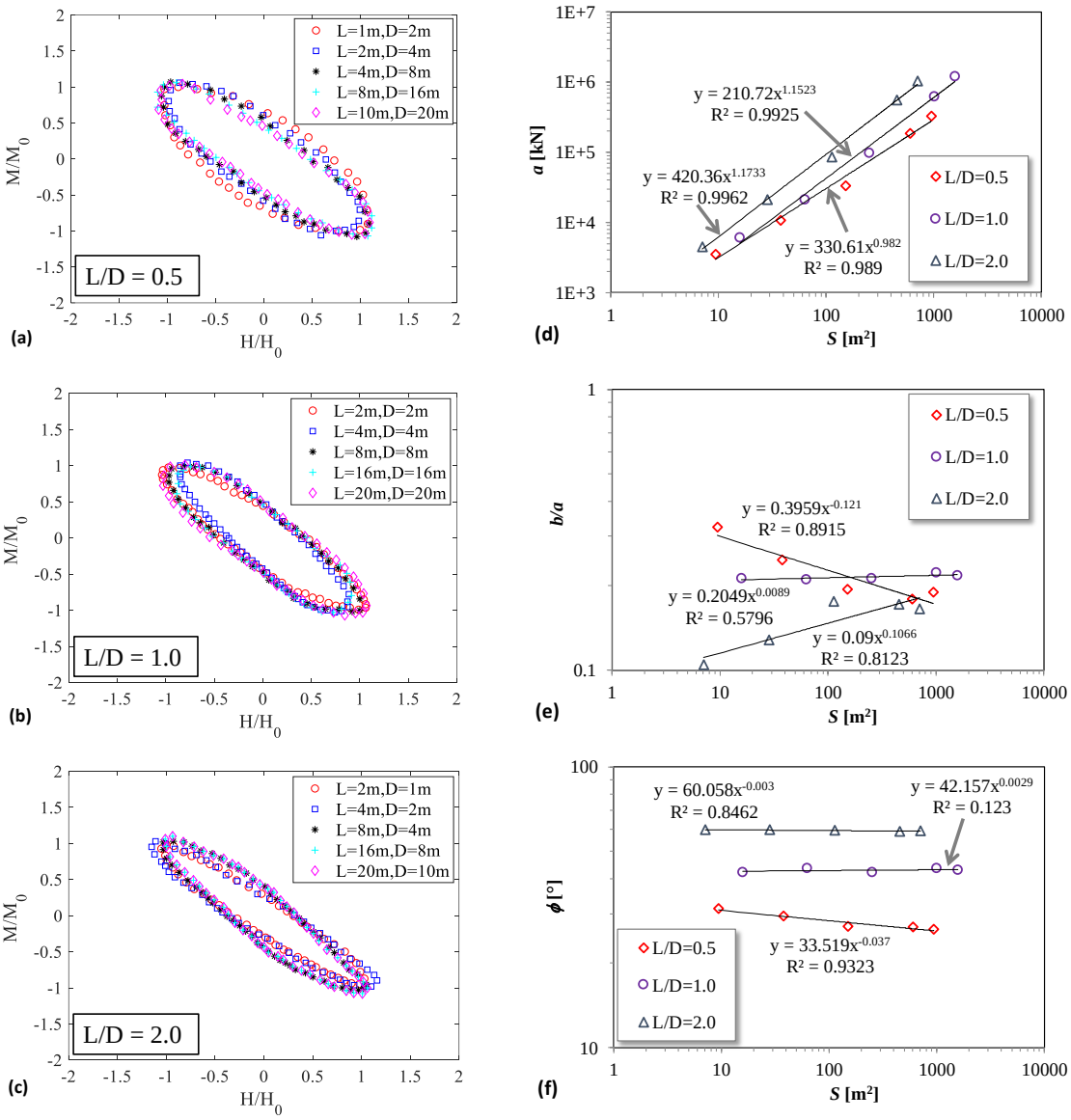

Figure 4.21 Normalized failure envelopes in the *H-M* plane for different geometry sizes: (a) *L/D* = 0.5, (b) *L/D* = 1.0, (c) *L/D* =2.0 and plot of the failure envelope characteristic measures versus the contact surface area *S* (d) ellipse size *a*, (e) ratio *b/a*, and (f) inclination angle *Ø*, CLSPH SIMSAND model

The main results are:

(1) For all conventional caisson sizes *L/D* the failure envelopes present a similar inclined elliptical shape.

(2) When $L/D < 1$, the failure envelopes present a slight tendency to contract with increasing caisson size; for $L/D = 1$, the failure envelopes are equivalent. When $L/D > 1$, the failure envelopes present a slight tendency to expand.

(3) With increasing caisson size *L/D*, the failure envelope exhibits a tendency to contract inward; for the same level of bending moment a smaller horizontal bearing capacity is obtained for larger aspect ratios. Yielding (horizontal) or even failure is more likely to occur on a caisson foundation with a larger aspect ratio. On the contrary and for the same level of horizontal force, a greater bending moment strength occurs for large aspect ratio i.e. an offshore wind turbine with a bigger caisson size aspect ratio has a stronger overturning resistance.

Following a similar analysis, the influence of the caisson size characteristics on the failure envelope is presented in Figure 4.21(d)-(f). Here, *S* is the total contact surface area between the caisson and the soil decomposed in two parts: the surface area of the bottom of the caisson and the surface area of the skirt. The values of the long axis *a* for different geometric sizes show a linear increase in logarithmic coordinates; the horizontal bearing capacity and overturning resistance are higher with increasing caisson size. For a specified contact surface area, the bearing capacity of the caisson improves slightly with increasing aspect ratio, Figure 4.21(d). The *b/a* ratio (*b* the short and *a* the long axis) versus the total contact surface area *S* is plotted in Figure 4.21(e). For increasing caisson sizes, *b/a* decreases when $L/D < 1$, stays constant for $L/D = 1$ and increases for $L/D > 1$. The inclination angle remains however unchanged, Figure 4.21(f). The influence of the caisson size aspect ratios on the inclination of the bearing capacity diagrams is therefore negligible.

4.3.4 Influence of the aspect ratio L/D for the same soil-structure contact surface area

A number of studies on caisson foundations were carried out to investigate the influence of the aspect ratio *L/D,* experimental (Houlsby et al. 2005; Cassidy et al. 2006; Zhang et al. 2007; Ibsen et al. 2013; Zhu et al. 2014; Ibsen et al. 2015; Tran and Kim 2017) and numerical (Cassidy et al. 2006; Gerolymos et al. 2012; Liu et al. 2014; Li et al. 2015; Cheng et al. 2016; Zafeirakos and Gerolymos 2016). In these studies, the L was changed while D was kept constant (or vice versa) and therefore the contact surface area was different.

In the following, the impact of the aspect ratio *L/D* on the failure envelope is studied for the same soil-structure contact surface area (implying thus the same cost of construction materials). Three groups of aspect ratio combinations are designed with original geometries equal to 2×2m,

4×4m, and 8×8m, details are given in Table 4.3. The corresponding numerically simulated failure envelopes are shown in Figure 4.22(a)-(c)). Due to the similar sizes, results are not normalized.

The main conclusions are:

(1) The failure envelopes present different degree inclined elliptical shapes.

(2) With increasing *L/D* ratio, the failure envelope axis rotates clockwise. During the rotation, the envelope gradually retracts along the short axis and stretches along the long axis direction.

(3) With increasing *L/D* ratio, the bearing capacity gradually transforms from horizontal force dominated failure to bending moment failure. For $L/D < 1$, the failure envelopes display a horizontal bearing capacity dominated trend; for $L/D = 1$, the bearing horizontal force and bending moment capacities are essentially the same; for $L/D > 1$, the bending moment bearing capacity is predominant.

During the design phase of caisson foundations for offshore wind turbines an adequate aspect ratio should be therefore selected according to the actual service environment. The relation between the aspect ratio *L/D* (for the same soil-structure contact surface area) and the failure envelope is quantified and presented in Figure 4.22. It can be seen that *a* and *Ø* increase with increasing aspect ratio, while in the contrary the ratio *b/a* decreases.

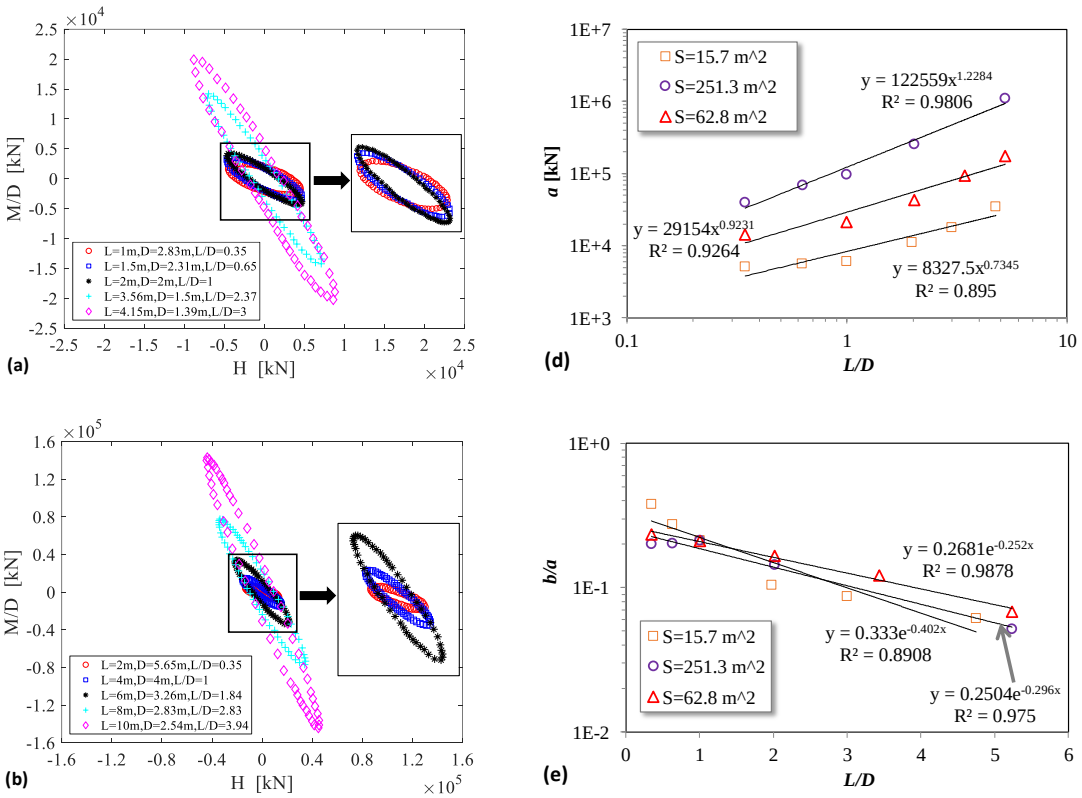

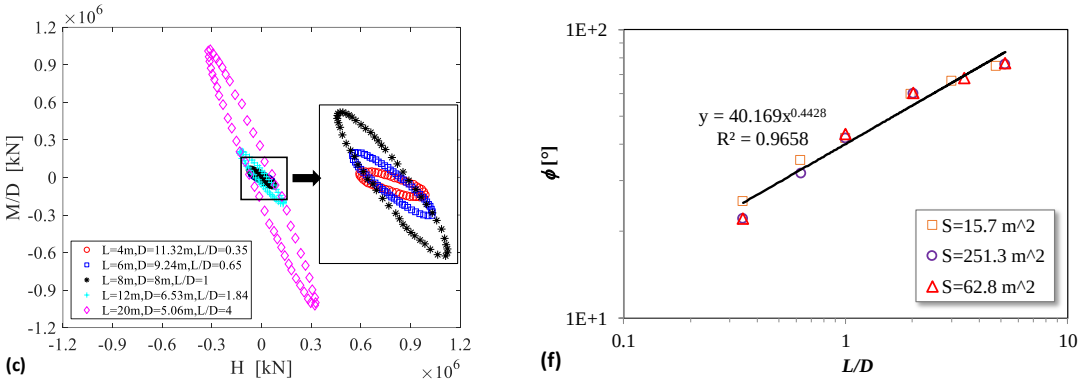

Figure 4.22 Failure envelopes in the *H-M* plane for different geometry sizes: (a) 2×2m, (b) 4×4m, (c) 8×8m, and plot of the failure envelope characteristic measures versus the aspect ratio *L/D*: (d) ellipse size *a*, (e) ratio *b/a*, and (f) inclination angle *Ø*, CLSPH SIMSAND model

Table 4.3 Geometry size configurations for a constant surface contact area

S = 15.7 m^2			S = 62.8 m^2			S = 251.3 m^2		
L (m)	D (m)	L/D	L (m)	D (m)	L/D	L (m)	D (m)	L/D
1	2.83	0.35	2	5.8	0.34	4	11.6	0.34
1.5	2.31	0.65	**4**	**4**	**1**	6	9.55	0.63
2	**2**	**1**	6	2.97	2.02	**8**	**8**	**1**
3.56	1.5	2.37	8	2.33	3.43	12	5.94	2.02
4.15	1.39	3	10	1.91	5.23	20	3.82	5.23

4.3.5 Combined effect of the soil-structure contact surface and the aspect ratio

In the previous sections, the influence of the caisson foundation size (*L/D*) and the aspect ratio *L/D* for the same soil-structure contact surface area on the shape and size of the failure envelope in the *H-M* space has been presented in detail. A formula is proposed hereafter to describe the coupling effect of the soil-structure contact surface area and the aspect ratio on the failure envelope:

$$\ln(x) = a_1 + a_2 \ln(S) + a_3 \ln(L/D) + a_4 \ln(S)\ln(L/D) \tag{4-1}$$

where x represents the failure envelope characteristic measures (a, b/a and $Ø$); S is the soil-structure total contact surface area; L/D is the aspect ratio and a_1, a_2, a_3 and a_4 are four constants used for fitting. Based on the previous numerical results (sections 4.3.3 and 4.3.4), the four constants are calibrated using the Least-Squares Fitting Method in MATLAB. Figure 4.23 displays the comparison between the numerical and the analytical formula estimated values for the three characteristic

measures (*a*, *b/a* and *Ø)* of the failure envelope. A strong correlation is observed that proves that the proposed formula is applicable for design purposes and the development of simplified modelling strategies such as the macroelement approach.

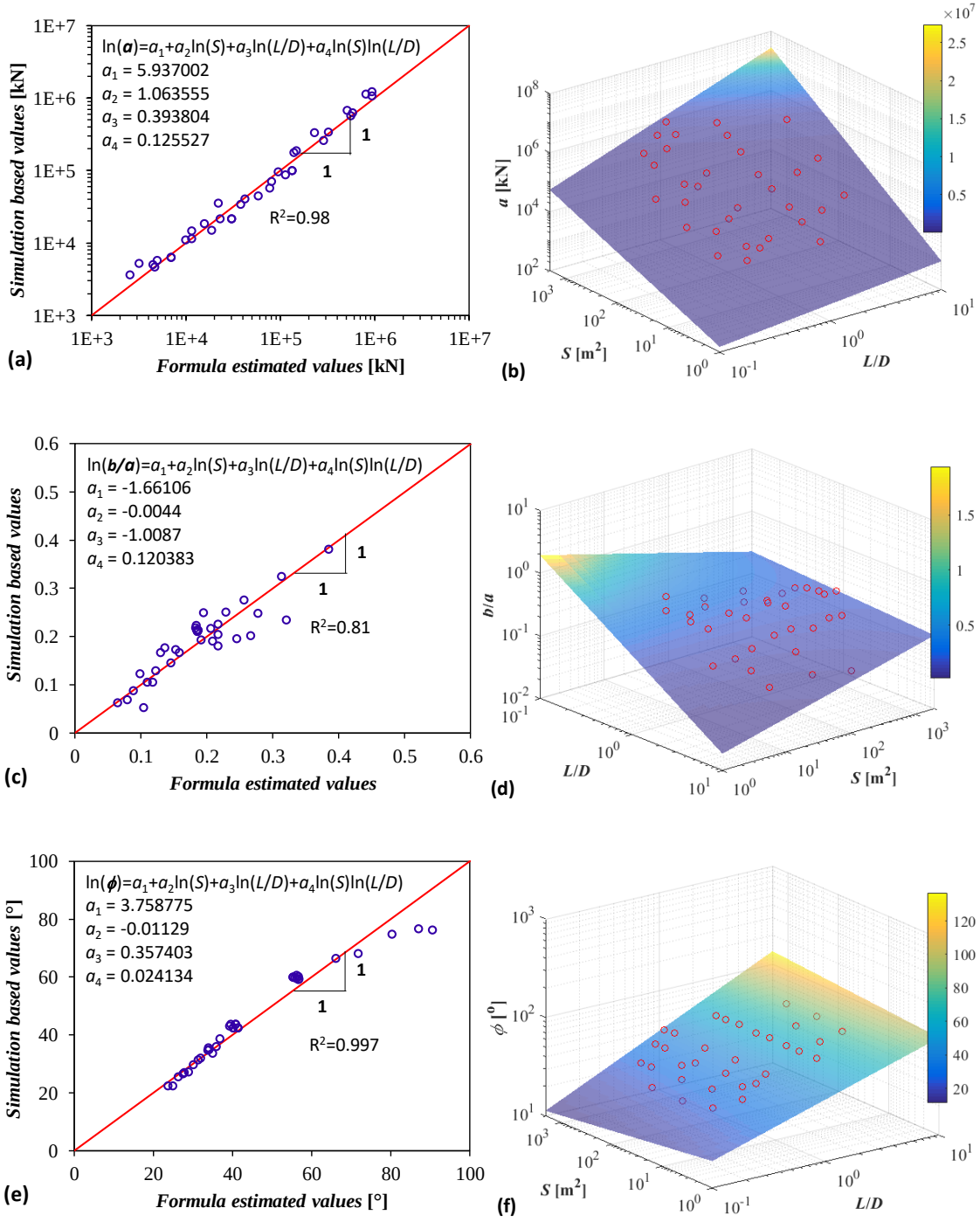

Figure 4.23 Comparison between numerically obtained characteristic measures and formula estimated values for: (a) size of ellipse *a* (b) 3D plot of *a* versus *S* and *L/D*, (c) *b/a* with (d) 3D plot of *b/a* versus *S* and *L/D*, and (e) inclination angle *Ø* with (f) 3D plot of *Ø* versus *S* and *L/D*, CLSPH SIMSAND model

4.4 Numerical estimation of V_0 for the *H-M-V* failure envelope

4.4.1 Influence of V_0 on the H-M failure envelope

The horizontal and overturning moment bearing capacities of caisson foundations vary significantly with the vertical load. In order to quantify this effect, a similar procedure as in section 4.3 is followed hereafter. More specifically, radial displacement numerical simulation tests are carried out for various levels of vertical load. The failure envelopes for different vertical load levels are presented in Figure 4.15. The field case shown in Figure 4.14 is also added (χ = 0.31). It can be concluded that:

(1) the influence of the vertical load on the inclination of the bearing capacity diagrams is negligible.

(2) the size of the bearing capacity diagram first increases with increasing vertical load and then displays a decreasing trend. This observation agrees with the experimental studies (Villalobos et al. 2009).

4.4.2 Numerical failure envelope in the H-V plane

Numerical radial displacement tests are hereafter performed to identify the failure envelope in the *H-V* plane. A displacement vector is applied on the LRP of the caisson foundation (see Figure 4.12) with an angle varying from 0~180°. The principle of the maximum load (see section 4.3.1) is again adopted to identify the points of the failure locus, see Figure 4.13. The obtained failure envelope is similar to the experimental data from Meyerhof (1953), Hansen (1970), DNV (2014) and Ibsen et al. (2014). Due to the high non-linearity the failure points form however an unsmoothed curve. The main results are summarized hereafter:

(1) The failure envelopes are symmetric about the H/V_0 axis.

(2) A strong interaction is observed between the vertical and the horizontal loads. The horizontal bearing capacity first increases and then decreases. As shown in Figure 4.24, a peak value is obtained for a vertical load equal to 0.4~0.5 of the vertical bearing capacity. This agrees with Figure 4.15 on the *H-M* plane. It can be also observed that the horizontal force is non-zero for null vertical loading because of the existence of the skirt.

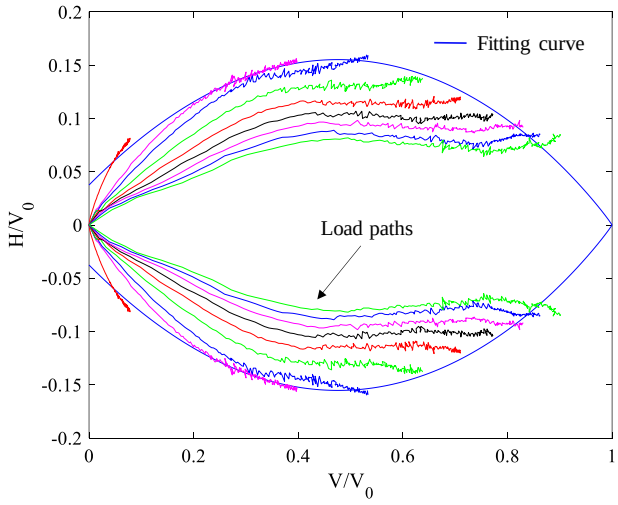

Figure 4.24 Numerical results for various load paths and approximate failure envelope in *H-V* plane, CLSPH SIMSAND model

4.4.3 Numerical failure envelope in the H-M-V 3D space

By combining the results in the *H-M* plane for different vertical levels (Figure 4.14(b) and Figure 4.15) and in the *H-V* plane (Figure 4.24), the *H-M-V* 3D space envelope is plotted in Figure 4.25. It has inclined elliptical cross-sections along the vertical force axis and its size is controlled by the value of the vertical load.

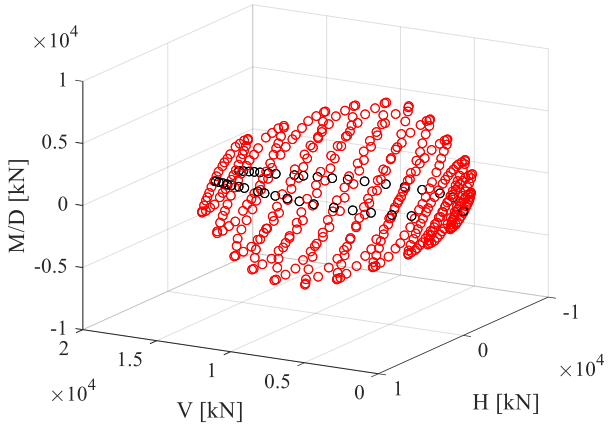

Figure 4.25 Failure envelope in the three-dimensional *H-M-V* space (numerical simulations, CLSPH SIMSAND model)

4.4.4 Influence of the soil properties and the caisson dimensions

The influence of the soil relative density D_r, the soil stiffness k_p, the friction angle ϕ_c, the grain breakage and the caisson dimensions (soil-structure contact surface area, aspect ratio) on the vertical bearing capacity V_0 are studied hereafter.

A strong linear tendency can be observed between V_0 and D_r, ϕ_c and k_p, see Figure 4.26. The vertical bearing capacity decreases for higher sand crushability. The most significant attenuation occurred with the Dog's bay sand, which is the most crushable sand.

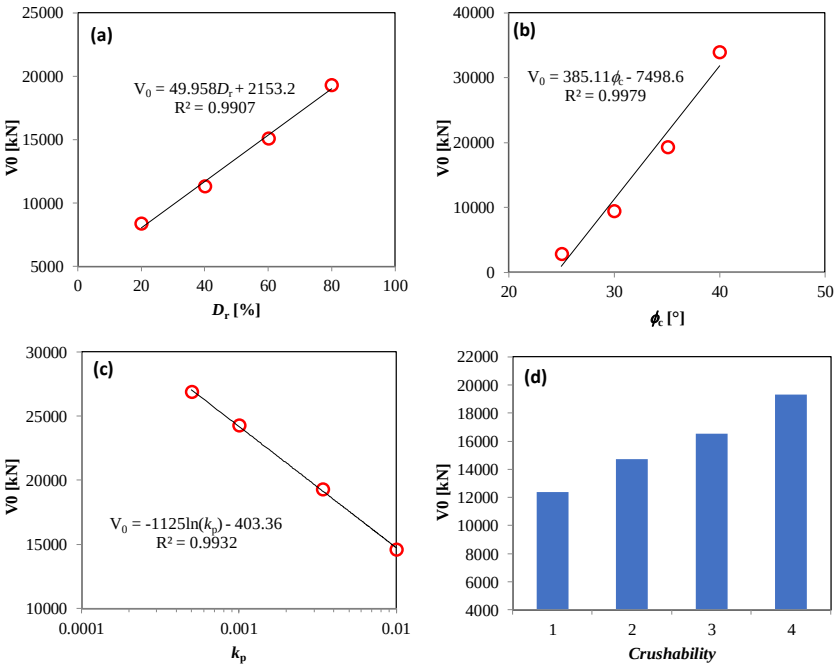

Figure 4.26 Relationship between vertical bearing capacity V_0 and related soil properties: (a) relative density, (b) critical friction angle, (c) plastic stiffness and (d) sand grain crushability, CLSPH SIMSAND model

The influence of the caisson foundation geometry on V_0 is presented in Table 4.2 (a similar simulation configuration as in section 4.3.3 is made). Figure 4.27 displays the relation between the vertical bearing capacity and the soil-structure contact surface area for three conventional aspect ratios. V_0 and S present a linear relation in logarithmic coordinates. It is worth noting that for different aspect ratios, the vertical peak-bearing capacity is found the same for similar contact surface areas. In other words, the vertical bearing capacity is mainly controlled by the contact surface area between the soil and the caisson, regardless of the aspect ratio.

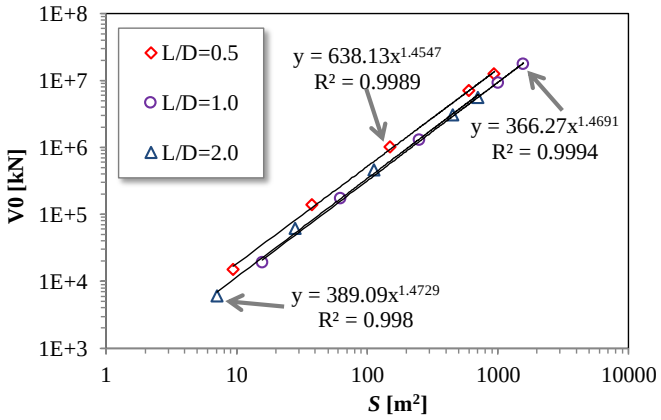

Figure 4.27 Vertical bearing capacity V_0 versus contact surface area S for different aspect ratios L/D, CLSPH SIMSAND model

To estimate the influence of the aspect ratio, the same soil-structure contact surface is maintained while simultaneously changing the values of L and D. The relation between the aspect ratio and the vertical bearing capacity for three geometry levels is shown in Figure 4.28. V_0 and L/D present a linear negative correlation in logarithmic coordinates; for the same surface contact area a bigger L/D implies smaller contact area between the bottom of the caisson and the soil. Furthermore, for the same aspect ratio the vertical bearing capacity increases with an increase in the caisson's geometry because of the contact area increase at the bottom of the caisson.

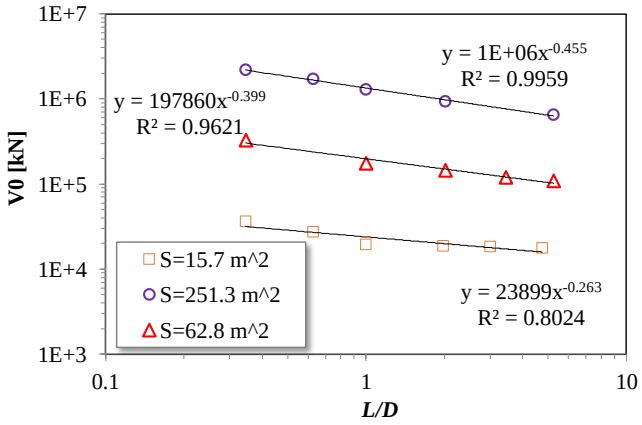

Figure 4.28 Vertical bearing capacity V_0 versus aspect ratio L/D, CLSPH SIMSAND model

The same analytical equation as in section 4.3.5 is adopted to describe the coupling between geometry, aspect ratio and vertical bearing capacity. Figure 4.29 illustrates the comparison between the simulation-based values and the formula-estimated values for a given vertical bearing capacity. The proposed analytical formula successfully reproduces the simulation results.

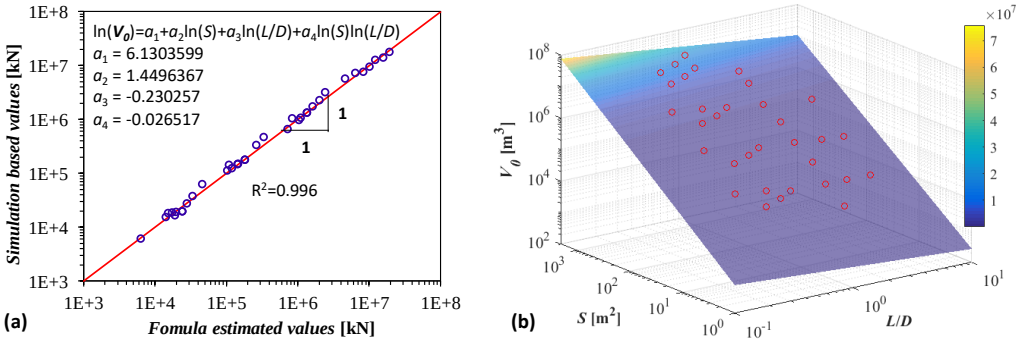

Figure 4.29 (a) Comparison between the vertical bearing capacity V_0 and the formula estimated V_0, and (b) 3D plot of the correlation between V_0, the contact surface area S and the aspect ratio L/D, CLSPH SIMSAND model

4.5 Analytical equations for the failure envelope

4.5.1 Analytical equations for failure envelope in the H-M plane

As shown in Section 4.3.1, the failure envelope in the *H-M* plane has an inclined elliptical shape. Following Villalobos et al. (2009), a similar formula is introduced to reproduce the inclined failure envelope of a caisson foundation in sand:

$$y = \left(\frac{H}{h_i V_0}\right)^2 + \left(\frac{M}{D m_i V_0}\right)^2 + 2e\frac{H}{h_i V_0}\frac{M}{D m_i V_0} - 1 = 0 \tag{4-2}$$

The general shape of the surface is determined by the parameters h_i, m_i, and e. The fitting parameters h_i and m_i represent the intersection of each ellipse with the H/V_0 and M/DV_0 axes respectively, e being the eccentricity of each ellipse. Using this equation, the yield points simulated in the previous sections can be fitted using a least-squares regression.

Eq. (4-2) satisfies the implicit equation of an ellipse, also referred to as the general equation:

$$A_1 X^2 + A_2 XY + A_3 Y^2 + A_4 X + A_5 Y + A_6 = 0 \tag{4-3}$$

The general equation's coefficients can be obtained from the semi-major axis a, the semi-minor axis b, the centre coordinates (x_c, y_c) and the rotation angle $\emptyset$ of the failure envelope using the following formulae:

$$\begin{cases} A_1 = a^2(\sin\phi)^2 + b^2(\cos\phi)^2 \\ A_2 = 2(b^2 - a^2)\sin\phi\cos\phi \\ A_3 = a^2(\cos\phi)^2 + b^2(\sin\phi)^2 \\ A_4 = -2A_1x_c - A_2y_c \\ A_5 = -A_2x_c - 2A_3y_c \\ A_6 = A_1x_c^2 + A_2x_cy_c + A_3y_c^2 - a^2b^2 \end{cases} \tag{4-4}$$

The center coordinates of the failure envelope in the *H-M* plane coincide with the origin. A_4, A_5 and A_6 therefore become:

$$\begin{cases} A_4 = 0 \\ A_5 = 0 \\ A_6 = -a^2b^2 \end{cases} \tag{4-5}$$

Here, only three parameters, *a*, *b* and $\emptyset$ describe the shape and size of the failure envelope in the *H-M* plane. By comparing Eq. (4-2) and Eq. (4-3), h_i, m_i and *e* are expressed as follows:

$$\begin{cases} h_i = \dfrac{ab}{V_0\sqrt{a^2\sin^2\phi + b^2\cos^2\phi}} \\ m_i = \dfrac{ab}{V_0\sqrt{a^2\cos^2\phi + b^2\sin^2\phi}} \\ e = \dfrac{\sin\phi\cos\phi\left(a^2 - b^2\right)}{\sqrt{\left(a^2\sin^2\phi + b^2\cos^2\phi\right)\left(a^2\cos^2\phi + b^2\sin^2\phi\right)}} \end{cases} \tag{4-6}$$

It must be pointed out that the values of *a* and *b* are related to the current vertical loading level χ. The coupling relationships among the characteristic measures of the failure envelope, soil-structure contact surface area and aspect ratio have been comprehensively analysed and quantified through Eq. (4-1). For a given caisson geometry, the failure envelope in the *H-M* space for a given soil can be therefore obtained using Eq. (4-1), Eq. (4-2) and Eq. (4-6).

Using Eq. (4-6), the fitted parameters h_i, m_i and *e* of the first group of aspect ratio combinations studied in section 4.3.4 are displayed in Table 4.4, in which the original geometry (field test) equals 2×2m. Figure 4.30 shows the comparison of Eq. (4-2) with the numerical results for the normalized failure envelope in the *H-M* plane. It is observed that the proposed equation fits well the different yield points.

Table 4.4 Intersection and eccentricity parameters: h_i, m_i and e

L (m)	D (m)	L/D	V/V_0	a	b	$\varnothing$(°)	h_i	m_i	e
1	2.83	0.35	0.18	4793	1820	25.4	0.1005	0.0601	0.657
1.5	2.31	0.65	0.26	5655	1518	36.4	0.1054	0.0808	0.871
2	2	1	0.31	6155	1308	42.1	0.0982	0.0896	0.913
3.56	1.5	2.37	0.26	15855	1557	63.9	0.0760	0.1521	0.970
4.15	1.39	3	0.28	21546	1878	66.3	0.0962	0.2151	0.973

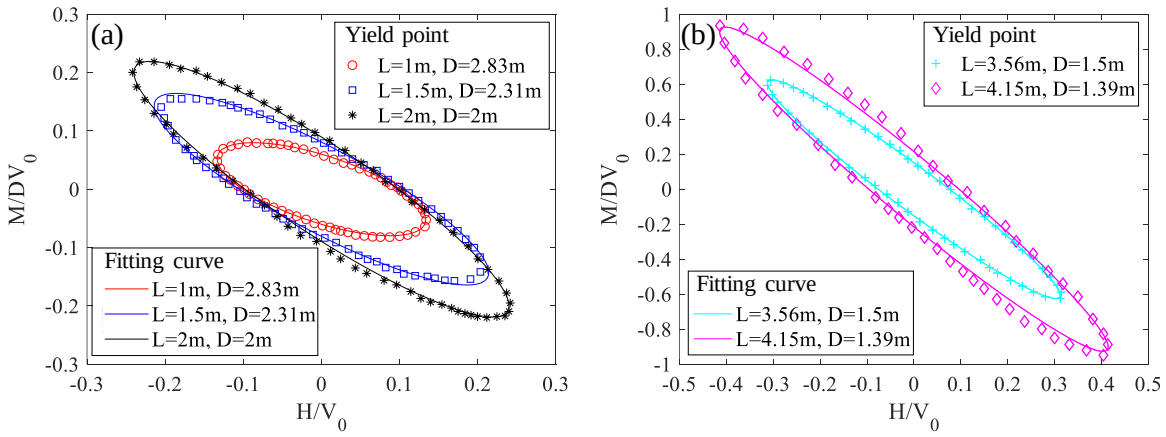

Figure 4.30 Comparison of fitted curves by the analytical equation and numerical results for different aspect ratios: (a) L/D=0.35, 0.65 and 1, (b) L/D=2.37 and 3, CLSPH SIMSAND model

4.5.2 Analytical equation for the failure envelope in the H-M-V 3D space

Figure 4.31 shows how h_i and m_i vary with the normalized load V/V_0. Note that the apex of the failure surface at low vertical loads is not at the origin but at a negative value because of the tension capacity of the caisson foundation. The tension capacity needs to be considered in order to obtain a more reasonable expression for the 3D failure surface.

The proposed formula is similar to that proposed by Villalobos et al. (2009) but in a more concise form.

$$h_i = \frac{H_i}{V_0} = h_0 \left(\frac{\beta_1^{\beta_1} + \beta_2^{\beta_2}}{t_0 + 1} \right)^{\left(\frac{\beta_1+\beta_2}{\beta_1\beta_2}\right)} \left(\frac{V}{V_0} + t_0 \right)^{\beta_1} \left(1 - \frac{V}{V_0} \right)^{\beta_2} \tag{4-7}$$

$$m_i = \frac{M_i}{V_0} = m_0 \left(\frac{\beta_1^{\beta_1} + \beta_2^{\beta_2}}{t_0 + 1} \right)^{\left(\frac{\beta_1+\beta_2}{\beta_1\beta_2}\right)} \left(\frac{V}{V_0} + t_0 \right)^{\beta_1} \left(1 - \frac{V}{V_0} \right)^{\beta_2} \tag{4-8}$$

The two parameters β_1 and β_2 are shaping parameters that allow to best fit the data and are generally close to unity (lager values will make the failure envelope concave (Ibsen et al. 2013)). h_0 and m_0 are the maximum values of h_i and m_i over the full range of V/V_0. t_0 controls the tension loading that the caisson foundation can sustain. It can be obtained by using a function of the skirt thickness t relative to the diameter of the caisson (Villalobos et al. 2004, 2005).

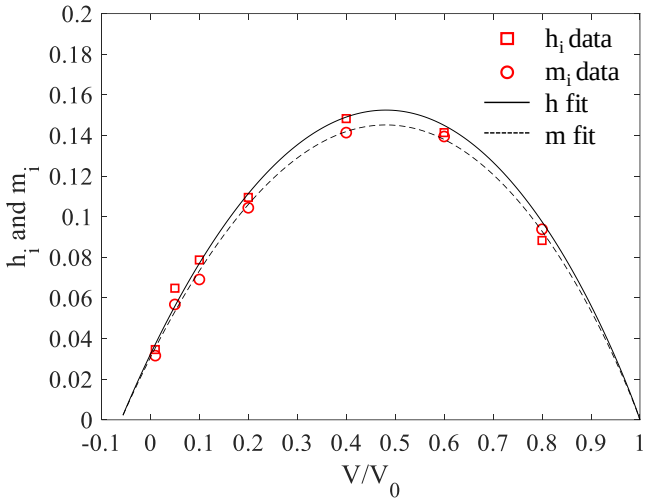

Figure 4.31 Intersection points h_i and m_i as a function of the normalized vertical load V/V_0

Eq. (4-2), (4-7) and (4-8) can be combined to represent an inclined parabolic ellipsoid in the 3D *H*-*M*-*V* plane as follows:

$$y=\left(\frac{H}{h_0V_0}\right)^2+\left(\frac{M}{Dm_0V_0}\right)^2+2e\frac{H}{h_0V_0}\frac{M}{Dm_0V_0}-F(V,V_t,V_0)=0 \tag{4-9}$$

Where

$$F(V,V_t,V_0)=\beta_{12}^2\left(\frac{V}{V_0}+t_0\right)^{2\beta_1}\left(1-\frac{V}{V_0}\right)^{2\beta_2},\ \beta_{12}=\left(\frac{\beta_1^{\beta_1}+\beta_2^{\beta_2}}{t_0+1}\right)^{\left(\frac{\beta_1+\beta_2}{\beta_1\beta_2}\right)} \tag{4-10}$$

Here V_t is the tension capacity of the caisson foundation. An example of the complete three-dimensional shape of the rotated failure surface is shown in Figure 4.32.

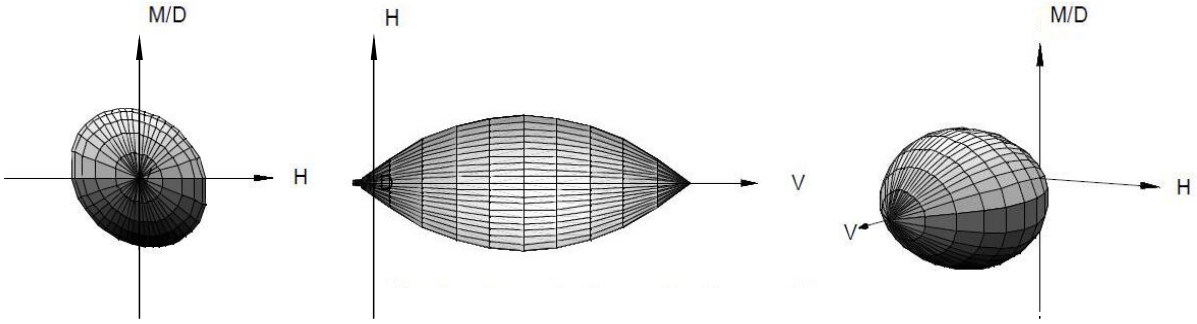

Figure 4.32 Illustration of the failure surface shaped as a parabola and inclined ellipse in the (*V, M/D, H*) load space

The parameters obtained from the best curve fitting with the numerical results are presented in Table 4.5. The 3D failure envelope for a caisson foundation in sand according to Eq. (4-9) is plotted in Figure 4.33(a). The expressions proposed by Gottardi et al. (1999), Byrne and Houlsby (1999) and Villalobos et al. (2009) are also plotted in Figure 4.33(b), Figure 4.33(c) and Figure 4.33(d). The correlation factor R^2 is estimated as 0.88, 0.67, 0.79 and 0.82, respectively indicating that Eq. (4-9) is more suitable to reproduce the 3D failure envelope of the caisson foundation.

Table 4.5 Parameters of the proposed failure surface for the 2×2 m caisson foundation

Parameter	**Name**	**Value**
V_0	Vertical bearing capacity: kN	19330
t_0	Tension factor	0.06
e	Eccentricity of failure surface	0.913
h_0	Dimension of failure surface (horizontal)	0.145
m_0	Dimension of failure surface (moment)	0.138
β_1	Shaping factor of failure surface	0.99
β_2	Shaping factor of failure surface	0.95

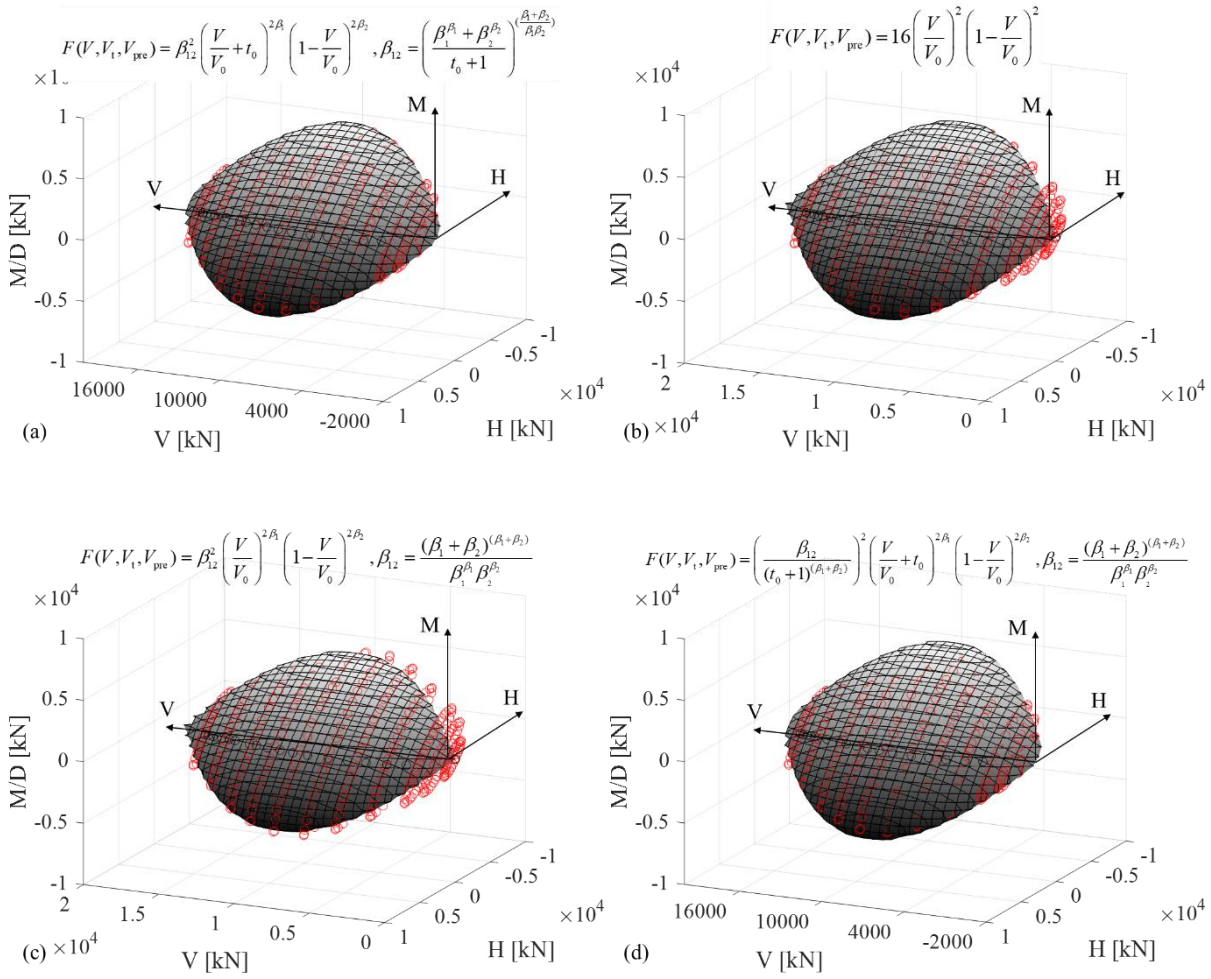

Figure 4.33 Numerical yield points fitted by the three-dimensional failure envelopes based on (a) Eq. (4-9), (b) Gottardi et al. (1999), (c) Byrne and Houlsby (1999) and (d) Villalobos et al. (2009)

4.6 Conclusions

A numerical study combining the Lagrangian-SPH method (CLSPH) and the elastoplasticity constitutive law SIMSAND is presented to identify the failure envelope of caisson foundation in sand. The soil parameters of the SIMSAND model were first calibrated from a series of triaxial tests on Baskarp sand. A simulation of a cone penetration test was then conducted to validate the CLSPH-SIMSAND modelling strategy. A series of model tests and a field test of a caisson foundation were also selected and simulated. Results demonstrated that the CLSPH-SIMSAND approach was able to reproduce the response of caisson foundation in sand with the calibrated soil parameters.

Then, a large number of finite element numerical calculations were carried out to investigate the behavior of a caisson foundation subjected to different load combinations. The radial displacement

method was adopted for the simulations. A series of factors including soil density, friction strength, soil stiffness, grain crushability, caisson geometry and aspect ratio, were considered to study the failure envelope. Finally, an analytical formula was proposed to describe the 3D failure envelope in the *H-M-V* space that can be used for the design and the development of simplified modelling strategies as the macroelement approach, seen in the next chapter.

Chapter 5 A hypoplastic macroelement for a caisson foundation in sand

5.1 Introduction

Caisson foundations are traditionally used for offshore structures such as oil and gas platforms, tension leg platforms or floating platforms (Randolph et al. 2011). During the last decade, the increasing application of caisson foundations for offshore wind turbines has proven to be a cost-effective alternative to gravity-based foundations and monopiles. Caisson foundations are made of steel and are usually subjected to vertical and long-duration monotonic or cyclic horizontal loads and moments that are transferred to the foundation through the footing beneath the structure (Byrne and Houlsby 2003; Ibsen 2008; Lesny 2010). For an optimum design, understanding the performance of caisson foundations under combined (multidirectional) loading is therefore necessary.

The finite element method is widely adopted to analyze the nonlinear behaviour of caisson foundations (Gourvenec 2008; Bransby and Yun 2009; Liu et al. 2014; Gerolymos et al. 2015; Ntritsos et al. 2015). Nevertheless, nonlinear finite element analyses are time-consuming and require considerable skill. A high-efficient and convenient practical strategy to reproduce the nonlinear behavior of foundations under combined loadings is the so-called macroelement approach introduced in geotechnical engineering by Nova and Montrasio (1991). In this approach, the nonlinear behavior of the soil - foundation system is expressed in terms of generalized forces and displacements through a reference point (Gottardi et al. 1999). The 2D or 3D stress resultant constitutive law is expressed following the plasticity or the hypoplasticity theory.

The first developments of the macroelement approach were for shallow footings under monotonic loading conditions (Montrasio and Nova 1997; Gottardi et al. 1999; Le Pape and Sieffert 2001; Martin and Houlsby 2001; Cassidy et al. 2002). More recently, the attention has been focused on the simulation of the cyclic/dynamic response of shallow footings for seismic analysis. Paolucci (1997) adopted an elastic-perfectly plastic macroelement with a non-associated flow rule. Crémer et al. (2001; 2002) developed an isotropic/kinematic hardening macroelement for cyclic/dynamic loading conditions and Grange et al. (2009) proposed a multi-mechanism, isotropic/kinematic hardening model considering the overturning mechanism and uplift. Further contributions in this field can be for example found in (Gajan 2006; Shirato et al. 2008; Chatzigogos et al. 2009; Gajan and Kutter 2009; Figini et al. 2012). Recent developments concern the spudcan behavior for jack-ups

(Martin and Houlsby 2001; Zhang et al. 2014) and caissons on clay (Cassidy et al. 2006) or on sand (Ibsen et al. 2014). Chatzigogos et al. (2011) conceived a bounding surface hyperplastic model for shallow foundation and Nguyen-Sy (2005), Nguyen-Sy and Houlsby (2005) proposed a hyperplastic model for the cyclic and seismic response of caisson foundations on sand. All the aforementioned macroelement models were developed within the framework of the classical (isotropic or anisotropic) theory of plasticity. Alternatively, macroelement models considering the rate-type constitutive equations of hypoplasticity (Kolymbas 1991; Tamagnini et al. 2000; Niemunis 2003) have been developed for shallow (Salciarini and Tamagnini (2009), Tamagnini et al. (2013)) and pile foundations (Li et al. (2016), Li et al. (2018)).

The aim of this chapter is to study the response of a caisson foundation in sand under static monotonic and cyclic loadings with a novel macroelement developed under the framework of hypoplasticity. First, a brief description of the macroelement's mathematical formulation is presented. An enhanced failure surface is introduced and the macroelement parameters are calibrated using one monotonic and one cyclic indoor model tests. Finally, further model tests are used to evaluate the predictive performance of the model.

5.2 Hypoplastic macroelement model

5.2.1 General framework

The hypoplasticity macroelement for shallow foundations and deep foundations introduced by Salciarini and Tamagnini (2009) and Li et al. (2016), Li et al. (2018) is used as a starting point to develop a hypoplastic macroelement for a caisson foundation in sand for static monotonic and cyclic loadings. The general framework is briefly given hereafter. The following definitions are adopted hereafter: bold letters define tensors, $\|\cdot\|$ the norm of a tensor and $(\cdot)$ the derivative with respect to time.

The mechanical response of the caisson foundation is described by means of a generalized load vector $\boldsymbol{t}$ and a generalized displacement vector $\boldsymbol{u}$ defined as:

$$\boldsymbol{t} := \{V, H, M/D\}^T \tag{5-1}$$

$$\boldsymbol{u} := \{w, u, D\theta\}^T \tag{5-2}$$

where *H*, *V* and *M* are the horizontal forces, the vertical force and the moment applied to the caisson, *w*, *u* and θ the vertical displacements, the horizontal displacements and the rotations respectively. The characteristic length *D* is the caisson diameter used to homogenize the dimensions of the components of $\boldsymbol{t}$ and $\boldsymbol{u}$. The generalized velocity vector $\boldsymbol{d}$ is defined as:

$$\boldsymbol{d} := \dot{\boldsymbol{u}} \tag{5-3}$$

The hypoplastic macroelement formulation in rate-form for monotonic loading conditions reads:

$$\dot{\boldsymbol{t}} = \mathcal{K}(\boldsymbol{t}, \boldsymbol{q}, \boldsymbol{d})\boldsymbol{d} \tag{5-4a}$$

$$\mathcal{K} = \boldsymbol{\mathcal{L}}(\boldsymbol{t}, \boldsymbol{q}) + \boldsymbol{N}(\boldsymbol{t}, \boldsymbol{q})\boldsymbol{\eta}^T \tag{5-4b}$$

$$\boldsymbol{\eta} = \frac{\boldsymbol{d}}{\|\boldsymbol{d}\|} \tag{5-4c}$$

where $\boldsymbol{q}$ is a pseudo-vector of internal variables accounting for the effects of the previous loading history.

The tangent stiffness $\mathcal{K}(\boldsymbol{t}, \boldsymbol{q}, \boldsymbol{d})$ differs from the classical elasto-plastic tangent stiffness in that it varies continuously with the direction $\boldsymbol{\eta}$ of the generalized velocity, a property known as incremental nonlinearity. It has two components, a "linear" term $\boldsymbol{\mathcal{L}}(\boldsymbol{t}, \boldsymbol{q})$ and a "nonlinear" term $\boldsymbol{N}(\boldsymbol{t}, \boldsymbol{q})$. The "linear" term describes the initial linear constitutive relationship of the macroelement. With the variation of the stress state however, the "linear" behavior is continuously modified by $\boldsymbol{N}(\boldsymbol{t}, \boldsymbol{q})$.

In order to consider cyclic loadings, the "internal displacement" $\boldsymbol{\delta}$ is introduced as internal variable, as proposed by Niemunis and Herle (1997) and Salciarini and Tamagnini (2009). The constitutive equation of the hypoplastic model is thus modified as follows:

$$\dot{\boldsymbol{t}} = \mathcal{K}(\boldsymbol{t}, \boldsymbol{q}, \boldsymbol{d}, \boldsymbol{\delta})\boldsymbol{d} \tag{5-5}$$

$$\mathcal{K} = \left[\rho^{\chi} m_T + (1 - \rho^{\chi}) m_R \right] \boldsymbol{\mathcal{L}} + \begin{cases} \rho^{\chi}(1 - m_T)(\boldsymbol{\mathcal{L}}\boldsymbol{\eta}_{\delta})\boldsymbol{\eta}_{\delta}^T + \rho^{\chi}\boldsymbol{N}\boldsymbol{\eta}_{\delta}^T & (\boldsymbol{\eta}_{\delta} \cdot \boldsymbol{\eta} > 0) \\ \rho^{\chi}(m_R - m_T)(\boldsymbol{\mathcal{L}}\boldsymbol{\eta}_{\delta})\boldsymbol{\eta}_{\delta}^T & (\boldsymbol{\eta}_{\delta} \cdot \boldsymbol{\eta} \leq 0) \end{cases} \tag{5-6}$$

where χ, m_T, and m_R are constants.

The evolution rate of the internal displacement is defined as:

$$\dot{\boldsymbol{\delta}} = \begin{cases} (\mathcal{I} - \rho^{\beta_r} \boldsymbol{\eta}_\delta \boldsymbol{\eta}_\delta^T)\boldsymbol{d} & (\boldsymbol{\eta}_\delta \cdot \boldsymbol{\eta} > 0) \\ \boldsymbol{d} & (\boldsymbol{\eta}_\delta \cdot \boldsymbol{\eta} \le 0) \end{cases} \tag{5-7}$$

where $\mathcal{I}$ is the identity matrix, the scalar $0 \le \rho \le 1$ is the normalized magnitude of $\boldsymbol{\eta}_\delta$, $\rho = \left(\frac{\|\boldsymbol{\eta}_\delta\|}{R} \right)$, β_r and R are two constants and:

$$\boldsymbol{\eta}_\delta = \begin{cases} \boldsymbol{\delta} / \|\boldsymbol{\delta}\| & (\delta \neq 0) \\ 0 & (\delta = 0) \end{cases} \tag{5-8}$$

By comparing Eqs. (5-4), (5-5) and (5-6) it can be observed that both the "linear" and "nonlinear" terms of the constitutive relationship are modified to reproduce cyclic loadings. The matrix $\boldsymbol{\mathcal{L}}$, which accounts for the stiffness at a load reversal point, is defined as:

$$\boldsymbol{\mathcal{L}} = \frac{1}{m_R} \boldsymbol{\mathcal{K}}^e \tag{5-9}$$

$$\boldsymbol{\mathcal{K}}^e := \begin{bmatrix} k_{vv} & 0 & 0 \\ 0 & k_{hh} & k_{hm} \\ 0 & k_{hm} & k_{mm} \end{bmatrix} \tag{5-10}$$

where $\boldsymbol{\mathcal{K}}^e$ is the elastic stiffness matrix and k_{vv}, k_{hh}, k_{mm} and k_{hm} define the vertical, horizontal, rotational and coupled horizontal-rotational stiffness of the foundation system respectively. As was the case for pile foundations (Li et al. (2016), Li et al. (2018)), the coupled effect between horizontal forces and moment must be considered for the caisson foundation because of the skirt.

The nonlinear function $\boldsymbol{N}$ can be expressed as:

$$\boldsymbol{N}(\boldsymbol{t}) = -Y(\boldsymbol{t})\boldsymbol{\mathcal{L}}\boldsymbol{m}(\boldsymbol{t}) \tag{5-11}$$

where $Y(\boldsymbol{t})$ is the scalar function which controls the degree of nonlinearity; and $\boldsymbol{m}(\boldsymbol{t})$ is the unit gradient which describes the plastic flow direction. In order to correctly define these two items in the hypoplasticity constitutive equation (eq. (5-11)), we need to introduce two important surfaces, i.e. the ultimate failure surface $F(\boldsymbol{t})$ and the loading surface $f(\mathbf{t})$.

In order to establish the ultimate failure (capacity) surface $F(\boldsymbol{t})$ for caisson foundation, in this study, numerical investigation is adopted to find the 3D failure surface and the details are as following. It is worth noting that a comprehensive investigation has been discussed in chapter 4 and a quick review is presented here. Different loading paths were numerically chosen to investigate the form of the failure surface in the *H-M* plane (Jin et al. 2018). As shown in Figure 5.1, a constant vertical load was first applied to the LRP (Loading Reference Point) of the caisson foundation up to a specified value. Then, radial displacement loadings were imposed (constant ratio of the rotation-displacements increments) to reach the ultimate strength. The failure loci points were defined as the final loading points of the different loading paths, Figure 5.2. The experimental model test results of Foglia et al. (2015) were also used to validate and complete the approach.

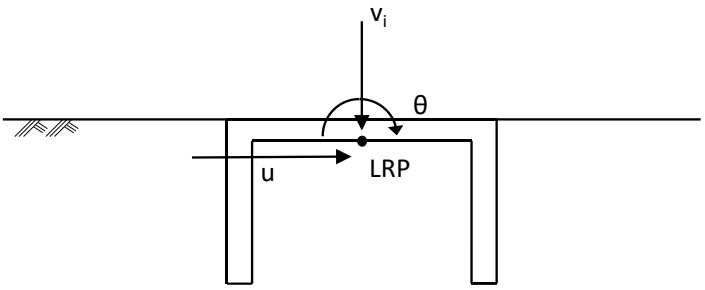

Figure 5.1 Caisson foundation, LRP (Loading Reference Point), vertical force and radial displacement loading in the *H-M* plane

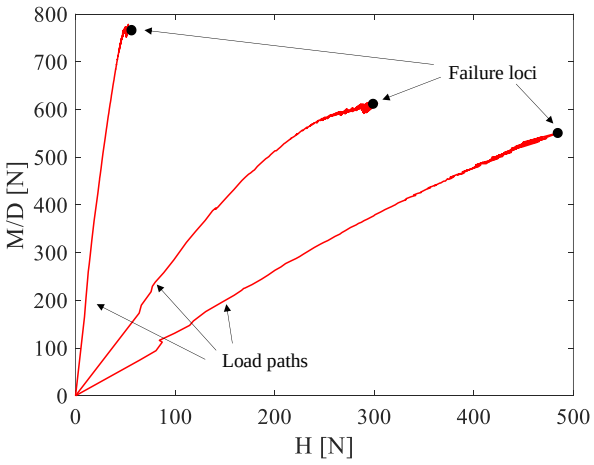

Figure 5.2 Determination of the failure loci for different load paths

A mathematical formula is presented hereafter to describe the failure surface in the *H:M/D* loading plane. Inspired by the work of Villalobos et al. (2009), the inclined failure envelope is given as:

$$F = \left(\frac{H}{h_i V_0}\right)^2 + \left(\frac{M}{Dm_i V_0}\right)^2 + 2e\frac{H}{h_i V_0}\frac{M}{Dm_i V_0} - 1 = 0 \tag{5-12}$$

where V_0 is the vertical bearing capacity of the foundation, the fitting parameters h_i and m_i represent the intersection of each ellipse with the H/V_0 and $M/(DV_0)$ axes respectively and e is the eccentricity of the ellipse. Using a least-squares regression, Eq.(5-12) is calibrated to fit the failure loci points obtained from simulations under different loading combinations (Jin et al. 2018) and monotonic model tests (Foglia et al. 2015), see Figure 5.3.

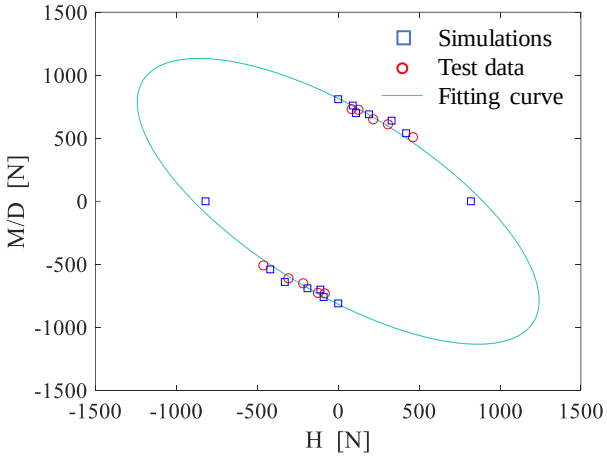

Figure 5.3 Failure envelope in the H:M/D loading plane: fitting curve based on model tests data and numerical simulation results

More specifically, Figure 5.4 shows the calibrated values of h_i and m_i as a function of the normalised vertical load V/V_0. The apex of the failure surface for low vertical loads has a negative value because of the tension capacity of the caisson foundation. Eqs. (5-13) and (5-14) provide the fitting functions, similar but simpler than the formulas proposed by Villalobos et al. (2009):

$$h_i = \frac{H_i}{V_0} = h_0\left(\frac{\beta_1^{\beta_1} + \beta_2^{\beta_2}}{t_0 + 1}\right)^{\left(\frac{\beta_1+\beta_2}{\beta_1\beta_2}\right)}\left(\frac{V}{V_0} + t_0\right)^{\beta_1}\left(1 - \frac{V}{V_0}\right)^{\beta_2} \tag{5-13}$$

$$m_i = \frac{M_i}{V_0} = m_0\left(\frac{\beta_1^{\beta_1} + \beta_2^{\beta_2}}{t_0 + 1}\right)^{\left(\frac{\beta_1+\beta_2}{\beta_1\beta_2}\right)}\left(\frac{V}{V_0} + t_0\right)^{\beta_1}\left(1 - \frac{V}{V_0}\right)^{\beta_2} \tag{5-14}$$

where β_1 and β_2 are shaping factors, generally close to unity, determined using a trial-error procedure. The upper limit of β_1 and β_2 is 1 as larger values make the failure envelope concave (Ibsen et al. 2013). V_0 can be determined numerically, by applying a pure vertical load up to failure. h_0 and m_0 are the maximum values of h_i and m_i over the full range of V/V_0. They are found approximately for $V/V_0 = 0.4$~0.5. The dimensionless quantity t_0 controls the tension loading that the caisson foundation can sustain (tension capacity) and can be obtained as a function of the skirt thickness to the caisson diameter (Villalobos et al. 2004; Villalobos et al. 2005). The two shaping factors β_1 and β_2 are hereafter determined using a trial-error procedure from the model tests conducted by Foglia et al. (2015). Note that Eqs. (5-13) and (5-14) can be used for different vertical load levels. All the macroelement constants are listed in Table 5.1.

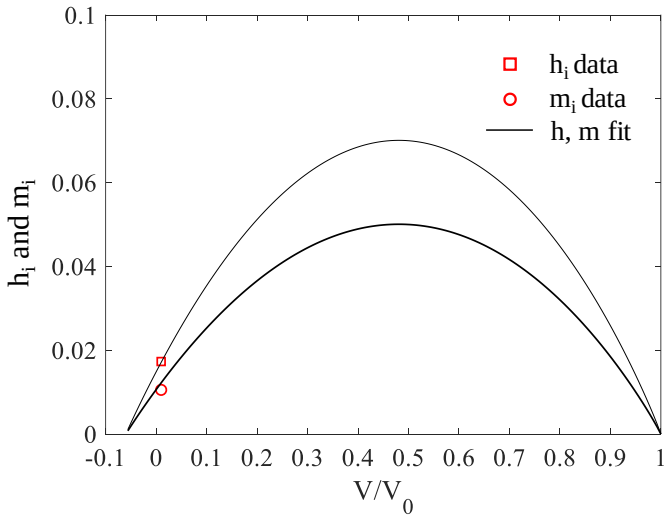

Figure 5.4 Shaping factors h_i and m_i as functions of the normalized vertical load V/V_0

Eqs. (5-12), (5-13) and (5-14) can be combined to represent an inclined parabolic ellipsoid in the 3D *H*-*M*-*V* space (see Figure 5.5), as follows:

$$F = \left(\frac{H}{h_0 V_0}\right)^2 + \left(\frac{M}{D m_0 V_0}\right)^2 + 2e\frac{H}{h_0 V_0}\frac{M}{D m_0 V_0} - F_V(V, V_t, V_0) = 0 \tag{5-15}$$

where

$$F_V(V, V_t, V_0) = \beta_{12}^2 \left(\frac{V}{V_0} + t_0\right)^{2\beta_1} \left(1 - \frac{V}{V_0}\right)^{2\beta_2}, \qquad \beta_{12} = \left(\frac{\beta_1^{\beta_1} + \beta_2^{\beta_2}}{t_0 + 1}\right)^{\left(\frac{\beta_1+\beta_2}{\beta_1\beta_2}\right)} \tag{5-16}$$

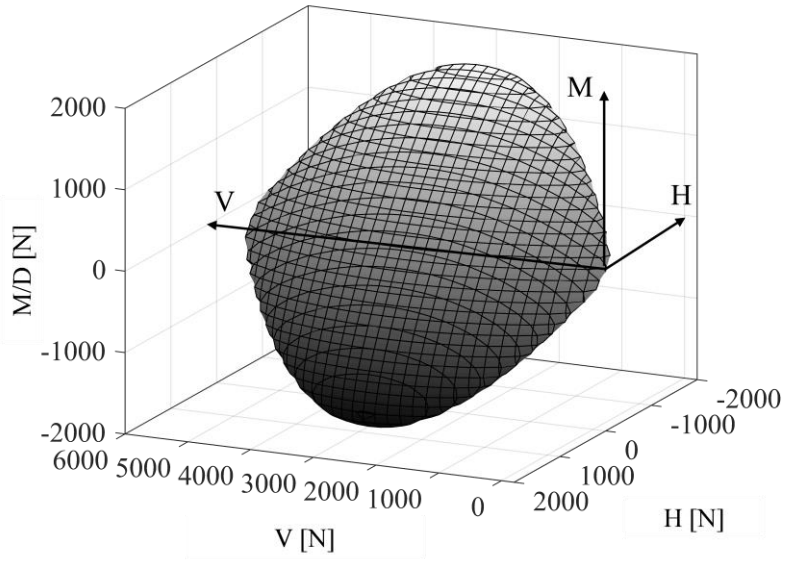

Figure 5.5 Failure surface in the 3D *H-M-V* space

In the framework of hypoplasticity, $F(\boldsymbol{t})$ is the bound of bearing capacity for caisson foundation which functions as a bounding surface. When the stress state approaches the bounding surface, plasticity is developing and at the bounding surface the full plastic state is reached. It is assumed that the current stress state lies on a so-called loading surface, $f(\boldsymbol{t})$, which has the same shape as the bounding surface but with a smaller size, see Figure 5.6.

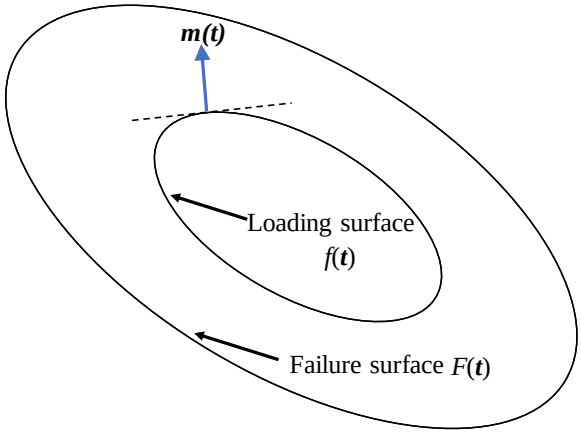

Figure 5.6 The unit gradient of the loading surface: ***m(t)***

With the development of plasticity, the loading surface will expand as isotropic as the bounding surface. The degree of nonlinearity is measured by the scalar function $Y(\boldsymbol{t})$ defined as:

$$Y(\boldsymbol{t}) = \xi^{\kappa} \tag{5-17}$$

where κ is a material constant that controls the evolution of the loading function; and $\xi \in [0,1]$, measures the distance between the loading surface $f(\boldsymbol{t})$ and failure surface $F(\boldsymbol{t})$.

From a geometric point of view as shown in Figure 5.6, the loading surface $f(\boldsymbol{t})$ which has a coincident shape compared to the failure surface $F(\boldsymbol{t})$ but of smaller size can be described as:

$$f = \left(\frac{H}{h_0 V_0^*}\right)^2 + \left(\frac{M}{D m_0 V_0^*}\right)^2 + 2e\frac{H}{h_0 V_0^*}\frac{M}{D m_0 V_0^*} - \beta_{12}^2 \left(\frac{V}{V_0^*} + t_0\right)^{2\beta_1} \left(1 - \frac{V}{V_0^*}\right)^{2\beta_2} = 0 \tag{5-18}$$

with:

$$V_0^* = \xi V_0 \le V_0 \tag{5-19}$$

The current stress state (H, M, V) must lie on the loading surface with $\xi \in [0,1]$. By substituting current stress state (H, M, V) to eq. (5-18), we can have a nonlinear function with respect to variable ξ. The root value of $\xi \in [0,1]$ can be determined by numerical approaches such as Newton-Raphson or bisection algorithm. In this study, the bisection method was adopted to calculate ξ.

$\boldsymbol{m}(\boldsymbol{t})$ is the normalized plastic flow direction taken as the normalized gradient of the loading function at the current loading state (see in Figure 5.6). An associative plastic flow rule is adopted and $\boldsymbol{m}(\boldsymbol{t})$ is given by:

$$\boldsymbol{m}(\boldsymbol{t}) = \frac{\partial f / \partial \boldsymbol{t}}{\left\| \partial f / \partial \boldsymbol{t} \right\|} \tag{5-20}$$

Where f is the above-mentioned loading function homothetic to $F = 0$ and passing through $\boldsymbol{t}$.

5.2.2 Synthesis of the macroelement parameters

The macroelement constants can be divided into four groups, see Table 5.1. Six of them describe the failure surface; four stiffness coefficients define the pseudo-elastic behaviour; one hardening constant controls the stiffness decay of the macroelement response for monotonic loadings; and five constants control the response for cyclic loadings.

Table 5.1 Parameters of hypoplastic macroelement model

Group	Parameters	Description	Value
Failure surface	V_0 (kN)	Vertical bearing capacity	90
	t_0 (-)	Tension factor	0.06
	e (-)	Eccentricity of failure surface	0.91
	h_0 (-)	Dimension of failure surface (horizontal)	0.068
	m_0 (-)	Dimension of failure surface (moment)	0.045
	β_1, β_2 (-)	Shaping factor of failure surface	0.96, 0.97
Pseudo-elastic stiffness	k_{vv} (kN/m)	Vertical stiffness	3100
	k_{hh} (kN/m)	Horizontal stiffness	3200
	k_{mm} (kN/m)	Rotational stiffness	1800
	k_{hm} , k_{mh} (kN/m)	Coupled translation-rotation stiffness	2500
Hardening parameter	κ (-)	Loading function constant	1.1
Cyclic behaviour (internal displacement)	m_R (-)	Stiffness at load reversal point	10
	m_T (-)	Stiffness when neutral loading	2
	R (-)	Range of linearity	0.006
	β^r (-)	Rate of evolution of internal displacement	0.5
	χ (-)	Transition of stiffness	0.5

5.3 Calibration and validation

5.3.1 Model tests

The hypoplastic macroelement for caisson foundations in sand is implemented into the MATLAB based finite element toolbox FEDEASLab (Filippou and Constantinides 2004). Numerical simulations and the model tests conducted by Foglia et al. (2015) are compared to identify and calibrate the macroelement parameters.

The experimental set-up by Foglia et al. (2015) consisted of a sandbox (1600 mm × 1600 mm × 1150 mm), a loading frame and a hinged beam. A system of steel cables and pulleys has been used to

apply loads to the foundation through an electric motor drive positioned on the hinged beam. The load, set by means of three weight hangers, was transferred to the foundation through a vertical beam bolted onto the caisson lid. The foundation was instrumented with three LVDTs (Linear Variable Differential Transformer) and two load cells. The caisson foundation was constructed of steel, with an outer diameter of 300 mm, a lid thickness of 11.5 mm, a skirt length of 300 mm and a skirt thickness of 1.5 mm. Various tests under different loading combinations have been carried out.

In the following, five dimensionally homogeneous monotonic moment-to-horizontal load ratios tests and two cyclic model tests at constant vertical load have been simulated numerically to identify and calibrate the macroelement constants and then to validate its performance.

5.3.2 Identification and calibration of the macroelement parameters

The pseudo-elastic stiffness coefficients of the macroelement are identified using adequate loading conditions and numerical simulations, see Figure 5.7, Li et al. (2016) and Jin et al. (2018). For example, the coupling stiffness k_{mh} is obtained by applying a small horizontal displacement at the LRP while the rotation is kept fixed. Results are summarized in Table 5.1.

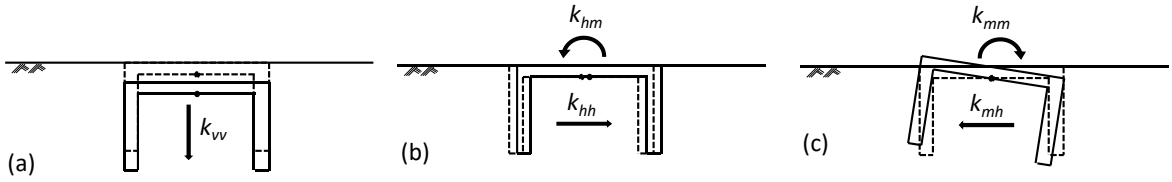

Figure 5.7 Loading conditions adopted to determine the stiffness coefficients of macroelement model

The model test with the monotonic loading combination M/DH = 3.01 of Foglia et al. (2015) is chosen to calibrate the hardening parameter κ. Additional macroelement simulations for different values of κ and for the same loading path were also been performed. Results are given in the H:u plane in Figure 5.8. Based on the comparison between the experimental and the simulation results, κ = 1.1 has been adopted for the loading function constant.

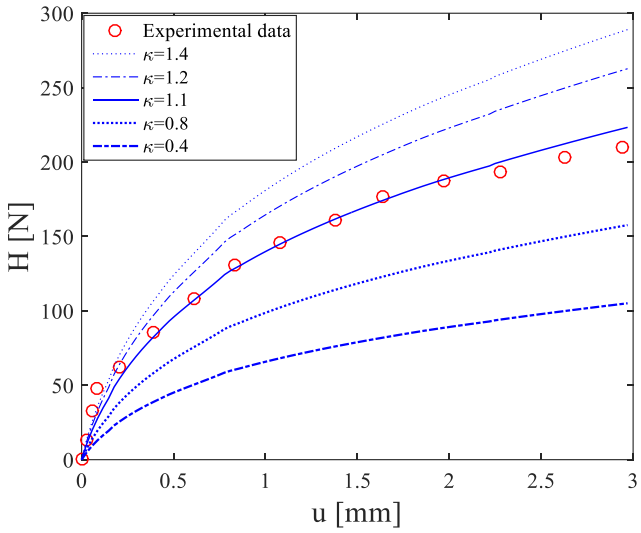

Figure 5.8 Loading conditions adopted to determine the hardening parameter of macroelement model

The cyclic response macroelement constants have been calibrated by trial and error using model test with the cyclic loading combination M/DH = 1.987 of Foglia et al. (2015). The loading frequency is f = 0.1Hz and the number of cycles (N) 5×10^4. Calibration is facilitated by the fact that the macroelement model response is not so sensitive to the constants β^r and χ. The size of the pseudo-elastic domain R can be guessed from the length of the quasi-linear portion of the load-displacement curves upon unloading or reloading, while the parameters m_R and m_T affect the ratio between the system stiffness under reverse or tangential loading and continued loading conditions. The calibrated values of the five cyclic constants are summarized in Table 5.1. Comparison between the experimental results and the macroelement simulations is shown in Figure 5.9(a) and Figure 5.9(c), where only the first 100 cycles are presented. Numerical simulations performed by Foglia et al. (2015) are also plotted in Figure 5.9(b). Here, The macroelement model presented in Foglia et al. (2015) originated from an existing model (Nova and Montrasio 1991) within the framework of work-hardening plasticity. The numerical results adequately describe the observed response of the system in the combined horizontal-moment cyclic loading test, indicating that the calibrated values of the macroelement constants controlling the cyclic response are reasonable.

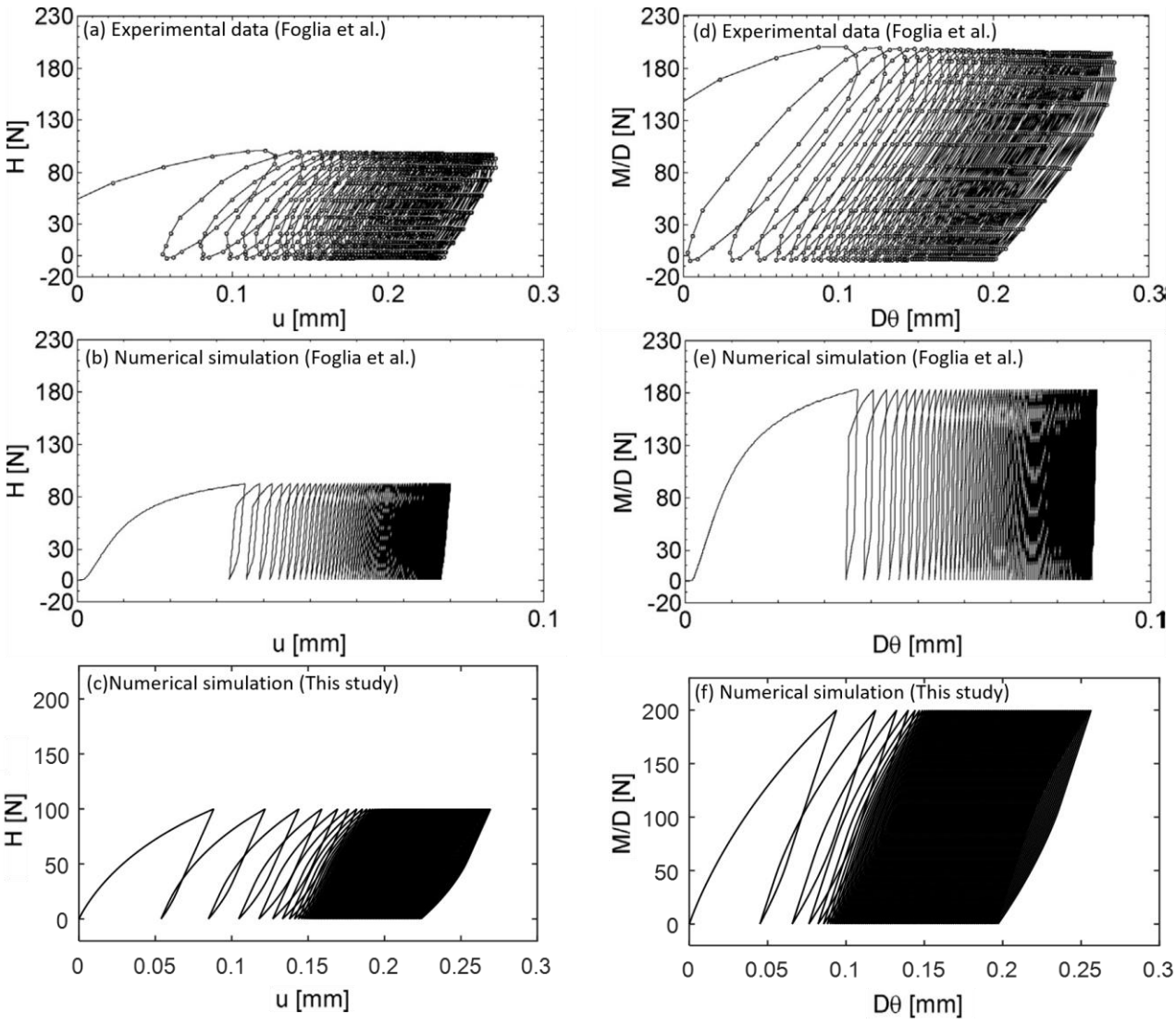

Figure 5.9 Horizontal displacement (u) versus horizontal load (H) for (a) experimental results, (b) simulated results by Foglia et al. (2015), (c) Macroelement prediction of this study; and rotational displacement ($D\theta$) versus dimensionally homogeneous moment (M/D) for (d) experimental results, (e) simulated results by Foglia et al. (2015), (f) Macroelement simulation of this study

5.3.3 Validation of the macroelement

Five monotonic tests and one cyclic test of Foglia et al. (2015) are adopted hereafter to evaluate the predictive capabilities of the macroelement. The monotonic tests were conducted at five different dimensionally homogeneous moment-to-horizontal load ratios (M/DH = 1.1, 1.987, 3.01, 5.82, 8.748). The cyclic test was carried out for M/DH = 1.987, M_{min} = -5N·m, M_{max} = 75N·m, H_{min} = -10N and H_{max} = 125N. The loading frequency was f = 0.1Hz and the number of cycles N= 5×10^4. The parameters of Table 5.1 are adopted in the macroelement simulations. Only the first 100 cycles are simulated and compared with the experimental response.

Figure 5.10 shows the comparison between the experimental model test results and the macroelement predictions for the monotonic tests. A fairly good agreement is observed for all the five moment-to-horizontal load ratios. Figure 5.11, illustrates the comparison between the experimental model test results and the macroelement predictions for the horizontal-rotational cyclic loading test. The macroelement prediction results are satisfactory, presenting even a better agreement in terms of accumulated permanent displacements that the numerical simulations of Foglia et al. (2015).

Overall, the coupling between the horizontal and rotational responses is well reproduced by the macroelement for both monotonic and cyclic loading conditions.

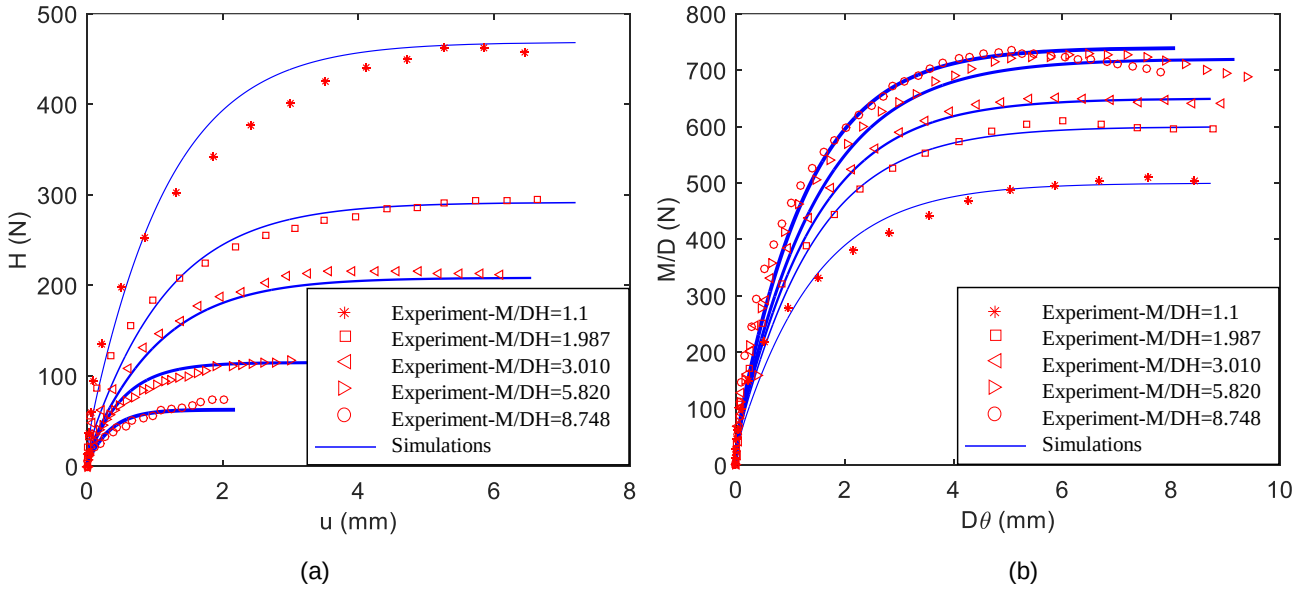

Figure 5.10 Comparison between experimental results and macroelement predictions for model tests under combined loadings of *M/DH*: curves of (a) *H-u* and (b) *M/D-Dθ*

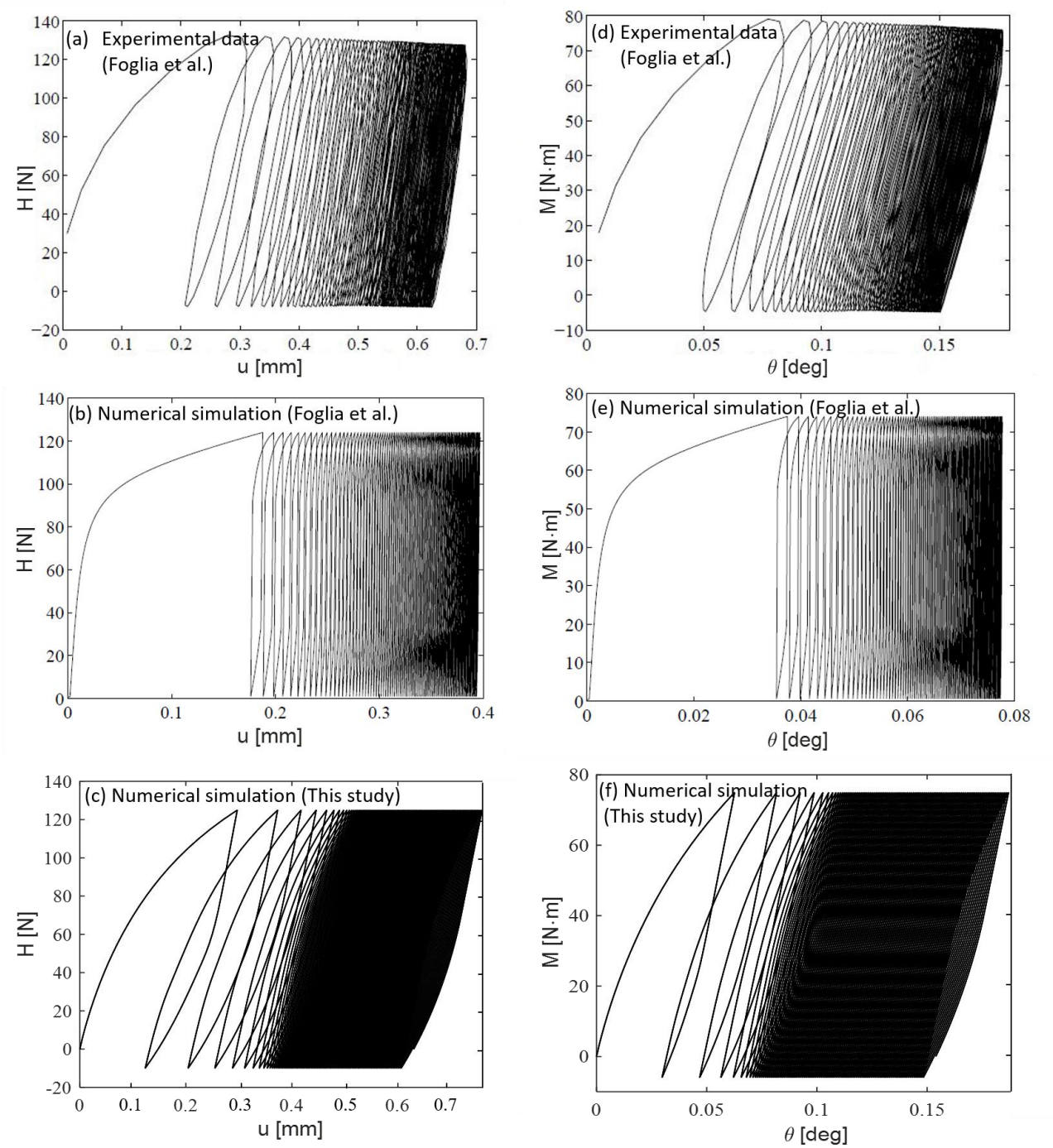

Figure 5.11 Horizontal displacement (u) versus horizontal load (H) for (a) experimental results, (b) simulated results by Foglia et al. (2015), (c) Macroelement prediction of this study; and rotational angle (θ) versus moment (M) for (d) experimental results, (e) simulated results by Foglia et al. (2015), (f) Macroelement prediction of this study

5.4 Conclusions

In this chapter, a novel macroelement for caisson foundations in sand is proposed within the framework of the theory of hypoplasticity. The incremental nonlinear constitutive equations are

defined in terms of generalized forces, displacements and rotations and the “internal displacement” concept is incorporated to take into account the effects of precious loading history under cyclic loading. An enhanced function has been proposed for the failure surface, in order to take into account multiple directional couplings.

A series of well-documented laboratorial reduced-scale 1g model tests have been used to calibrate the macroelement constants and to assess its performance. Comparisons between predictions and experimental results demonstrate that the proposed macroelement is capable of reproducing the behaviour of caisson foundations in sand subjected to monotonic and cyclic loadings.

It is worth noting that the efficiency of the macroelement is much higher than that of conventional nonlinear 3D finite element simulations in terms of computational costs. This advantage is of particular importance for practical applications where the caisson foundation is subjected to a large number of cycles caused by environmental loadings, such as the ocean current and waves. The proposed macroelement is a useful tool for the design of caisson foundations in sand subjected to combined monotonic or cyclic loadings.

Chapter 6 General conclusions and perspectives

6.1 General conclusions

In this PhD, the behavior of caisson foundations in sand under combined monotonic and cyclic loadings is investigated by finite element numerical simulations and the development of a novel macroelement. The new numerical tools are validated with experimental results available in the literature. The main contributions and conclusions of the work are summarized as follows:

(1) A review of the existing experimental and numerical studies on the response of caisson foundations subjected to combined loadings is first presented. The limitations of the current approaches are highlighted; a method that can accurately reproduce large deformations during extreme loading conditions (such as during the installation phase) is required. Furthermore, an advanced constitutive model and a fast and robust numerical tool are necessary to correctly simulate the nonlinear behaviour of the foundation under combined loadings.

(2) The evolving failure of a caisson foundation in sand submitted to complex loading combinations is first simulated using a Combined Lagrangian - Smoothed Particle Hydrodynamics (CLSPH) method and the Mohr-Coulomb constitutive model. The performances and limitations of the approach are discussed.

(3) In order to improve the modeling strategy, a modern critical state soil constitutive law (SIMSAND) is introduced. The model is combined with the CLSPH method to simulate large deformations and the approach is validated using experimental data from rectangular channel and two-dimensional column collapse tests. All comparisons show that the adopted numerical strategy is able to reproduce qualitatively and quantitatively the main behaviour of granular column collapse, i.e. free surface, failure line, deformed profile, run-out distance and deposit height.

(4) The CLSPH - SIMSAND approach is then adopted to reproduce the nonlinear behavior of a caisson foundation in sand subjected to different load combinations. After several validations using experimental results, the 3D bearing capacity of the foundation is investigated considering several factors including soil density, friction strength, soil stiffness, grain crushability, geometry

size and aspect ratio. An analytical formula is proposed to describe the 3D failure envelope. Once the caisson geometry determined, the value of vertical bearing capacity and the shape and size of the failure envelope can be directly obtained. The pivotal parameters for the analytical formula can be found by simple numerical simulations, empirical equations or experimental results.

(5) A novel macroelement for a caisson foundation in sand is finally introduced, based on the framework of hypoplasticity. Comparison between the macroelement predictions and the observed response indicates that the macroelement is capable of reproducing the caisson-soil system nonlinear behavior for combined monotonic and cyclic loadings. The required calculation time is much smaller than that of a classical finite element model and therefore the macroelement is a very useful tool for structural design in the offshore engineering field.

6.2 Perspectives

Several perspectives are possible:

(1) In practice, caisson foundations are used in two configurations to support offshore wind turbines. The first is a mono-caisson supporting a mono-tower, the research object of this thesis. The second configuration is three or four caissons supporting a jacket structure. In this last configuration, the pullout resistance is a key design factor and the suction force must be considered to obtain the accurate response in the vertical direction. The installation phase considering suction effect needs also to be numerically investigated.

(2) This research mainly focused on the bearing capacity characteristics of a caisson foundation in sand. A similar procedure should be also adopted for clays. Numerical simulations on soft clays need to reproduce the undrained characteristics of the saturated porous media.

(3) The macroelement developed in this PhD considers three degrees of freedom, i.e. vertical (V), horizontal (H) and rotational (M). Further investigations should extend it to six degrees of freedom, i.e. Vertical (V), horizontal (H_x, H_y), rotational (M_x, M_y) and torsional (T) loading.

Appendixes

(I) Basic equations of the Mohr-Coulomb model

The basic equations of the Mohr-Coulomb model are presented hereafter:

Yield function:

$$F = R_{mc} q - p \tan\varphi - c = 0 \tag{A.I-1}$$

$$R_{mc}\left(\Theta,\varphi\right) = \frac{1}{\sqrt{3}\cos\varphi}\sin\left(\Theta + \frac{\pi}{3}\right) + \frac{1}{3}\cos\left(\Theta + \frac{\pi}{3}\right)\tan\varphi$$

$$\text{with}\ \ \cos\left(3\Theta\right) = \left(\frac{J_3}{q}\right)^3 \tag{A.I-2}$$

Potential function:

$$G = \sqrt{\left(\varepsilon c_0 \tan\psi\right)^2 + \left(R_{mw} q\right)^2} - p\tan\psi \tag{A.I-3}$$

$$R_{mw} = \frac{4\left(1-e^2\right)\cos^2\Theta + \left(2e-1\right)^2}{2\left(1-e^2\right)\cos\Theta + \left(2e-1\right)\sqrt{4\left(1-e^2\right)\left(\cos\Theta\right)^2 + 5e^2 - 4e}} R_{mc}\left(\frac{\pi}{3},\varphi\right)$$

$$\text{with}\ \ e = \frac{3-\sin\varphi}{3+\sin\varphi} \tag{A.I-4}$$

where F yield function, q deviatoric stress, p mean stress, φ friction angle, c cohesion, J_3 the third invariant of the deviatoric strain tensor, G potential function, ψ dilatancy angle, c_0 initial value of cohesion, $\varepsilon = 0.1$ (default value in ABAQUS).

(II) Basic equations for a plasticity model for shallow foundations in sand (Byrne and Houlsby 1999; Cassidy 1999; Gottardi et al. 1999; Villalobos et al. 2005)

Gottardi and Houlsby (1995) were among the first authors to investigate the full behavior of circular footings on sand in the laboratory under combined loads through a macro-model approach. The tests were performed on dense dry sand (D_r = 75%). Gottardi et al. (1999) interpreted the experiments and suggested an expression of F (V, V_t, V_{pre}), which is given in Table A.II.1.

Table A.II.1 Yield Surface Expressions Reported in Literature

Models	F (V, V_t, V_{pre})	Foundation type
Gottardi et al. (1999)	$16\left(\frac{V}{V_0}\right)^2\left(1-\frac{V}{V_0}\right)^2$	Circular surface footings
Cassidy (1999) Byrne and Houlsby (1999)	$\beta_{12}^2\left(\frac{V}{V_0}\right)^{2\beta_1}\left(1-\frac{V}{V_0}\right)^{2\beta_2}, \beta_{12}=\frac{(\beta_1+\beta_2)^{(\beta_1+\beta_2)}}{\beta_1^{\beta_1}\beta_2^{\beta_2}}$	Circular surface and caisson foundations
Villalobos et al. (2005)	$\left[\frac{\beta_{12}}{(t_0+1)^{(\beta_1+\beta_2)}}\right]^2\left(\frac{V}{V_0}+t_0\right)^{2\beta_1}\left(1-\frac{V}{V_0}\right)^{2\beta_2}$	Caisson foundations

Yield surface

The shape of the yield surfaces presented in the following sections can be expressed by the following general empirical equation:

$$f=\left(\frac{H}{h_0V_{pre}}\right)^2+\left(\frac{M}{m_0DV_{pre}}\right)^2-2a\left(\frac{H}{h_0V_{pre}}\right)\left(\frac{M}{m_0DV_{pre}}\right)-F\left(V,V_t,V_{pre}\right)=0 \qquad \text{(A.II-1)}$$

where f describes the yield surface function; and V_t = tension capacity of the shallow foundation. The general shape of the surface is determined by three parameters, h_0, m_0, and a, in the radial planes. The parameters h_0 and m_0 determine the size of the yield surface at the widest section of the surface along the V-axis by $H_{M=0}/V_{pre}$ and $M_{H=0}/DV_{pre}$, respectively, where $H_{M=0}$ is the value of H at the intersection with the M = 0 axis, and $M_{H=0}$ is the corresponding value for M. The terms $H_{M=0}$ and $M_{H=0}$ are also denoted H_{peak} and M_{peak}, respectively.

Byrne and Houlsby (1999) evaluated a large set of combined loading tests on bucket foundations in very dense sand (D_r = 95%). For such a case, they also found that the shape of the yield surface could be approximated by rotated ellipses in the radial planes. The rotation of the yield surface as well as the shape was found to change with the embedment ratio.

Adopting the yield surface expression suggested by Gottardi et al. (1999) results in a change in the parameters with the embedment ratio. The presented yield surface functions clearly have one drawback relative to the behavior of bucket foundations. The apex of the yield surface at low vertical loads for bucket foundations is not located at the origin but at a negative value due to the tension capacity in contrast to surface foundations. Villalobos et al. (2004,2005) also noticed this. They suggested a modified yield function by introducing a dimensionless constant, t_0 (see Table A.II.1). The constant t_0 is proposed to be a function of the skirt thickness t relative to the diameter of the bucket. The apex of the yield surface at low vertical loads is of especially great importance for wind turbine foundations because of the small self-weight of the structure. The yield surface expression by Villalobos et al. (2005) is based on experiments on bucket foundations with a single embedment ratio equal to 0.5 on saturated medium dense sand. The findings presented by Villalobos et al. (2004) are also based on observations from tests on bucket foundations with two different embedment ratios (0.5 and 1) on loose (*Dr* = 30%) dry sand.

The choice between β_1 and β_2 determines the value of $v = \beta_1 / (\beta_1 + \beta_2)$, i.e., the location of the peak of the parabola along the V-axis, as well as the slope of the ends of the parabola. The values of β_1 and β_2 are generally found to be close to unity; however, values of β_1 and β_2 less than unity reduce the sharp angles of the yield surface at the intersections with the V-axis. The values of β_i are limited by a value equal to 1.0 because the failure surface for larger values becomes concave. For $\beta_1 = \beta_2 = 1$, the yield surface is seen to coincide with the expression from Gottardi et al. (1999), and the widest section in the radial plane is located at $v = 0.5$. The value of v in the literature is generally found to be between 0.45 and 0.5 for surface footings, i.e., $\beta_1 < \beta_2$. For surface footings, Houlsby and Cassidy (2002) simplified the expression from Martin (1994) by choosing $a = 0$ and $\beta_1 = \beta_2 = 1$, which corresponds to observations from Butterfield (1979).

Elastic behavior

The elastic behavior of a circular foundation subjected to planar loading can be described by the following yield surface elastic matrix:

$$\begin{bmatrix} V/GR^2 \\ H/GR^2 \\ M/GR^2 \end{bmatrix} = DG \begin{bmatrix} k_{VV}^0 & 0 & 0 \\ 0 & k_{HH}^0 & k_{HM}^0 \\ 0 & k_{HM}^0 & k_{MM}^0 \end{bmatrix} + \begin{bmatrix} dw_p \\ d\theta_p \\ du_p \end{bmatrix} \qquad \text{(A.II-2)}$$

where R = radius of the foundation; G = shear modulus of the soil; and k_{ij}^0 = nondimensional static stiffness components. The static stiffness components for surface, embedded, and bucket foundations have been investigated theoretically, e.g., by Spence (1968), Poulos and Davis (1974),Bell (1991), Ngo-Tran (1996),Doherty and Deeks (2003),and Liingaard (2006).The static stiffness components are found to be dependent on Poisson's ratio, the shear modulus, the embedment ratio, i.e., *d/D*, the stiffness of the foundations relative to the stiffness of the soil, and the base roughness.

Hardening law

During loading of the foundation, the hardening law proposes the size of the yield surface for a given load state. Within the micromodel approach, the size is assumed to be controlled by the vertical preload of the foundation, i.e., the upper apex of the yield surface. The type of hardening law presently used is the strain-hardening type, where the relation between the vertical plastic settlement and the vertical preload is used.

A linear relation proposed by Byrne and Houlsby (1999) is given by the following equation:

$$V = k_p w_p \tag{A.II-3}$$

where k_p = plastic stiffness, which is assumed to be constant; and w_p = plastic component of the vertical settlement. This relation is not practically useful for soils.

Based on the results from vertical loading tests on circular surface footings on medium dense (*Dr* = 75%) and dry yellow Leighton Buzzard sand, Gottardi et al. (1999) fitted the following empirical expression:

$$V = \frac{kw_p}{1+\left(\frac{kw_{pm}}{V_{peak}}-2\right)\left(\frac{w_p}{w_{pm}}\right)+\left(\frac{w_p}{w_{pm}}\right)^2} \tag{A.II-4}$$

where w_{pm} = size of the vertical plastic settlement at failure.

Additionally, Cassidy et al. (2002) found that the following relatively simple relation fits the results from vertical loading tests of circular footings on loose carbonate sand:

$$V = \frac{cw_p + k_2 w_p^2}{k_1 + w_p} \tag{A.II-5}$$

where c, k_1, and k_2 are constants.

Flow rule

During loading of a foundation when yielding occurs, the hardening rule determines the stiffness of the response, whereas the ratios between the plastic displacement components are determined by the flow rule. The plastic displacements including rotation are determined from a potential function by the flow rule given in the following formula:

$$\begin{bmatrix} dw_p \\ d\theta_p \\ du_p \end{bmatrix}_p = \lambda \begin{bmatrix} \frac{\partial g}{\partial V} \\ \frac{\partial g}{\partial H} \\ \frac{\partial g}{\partial M} \end{bmatrix} \qquad \text{(A.II-6)}$$

where g = 0 is a potential function; and λ is a positive scalar that defines the magnitude of the plastic displacements, which is determined from the hardening law. The potential function is defined as a function that forms a potential surface in the load space on which the direction of the incremental plastic displacements is perpendicular. If the potential function is chosen to be identical to the yield function, then this is denoted as associated flow and is non-associated flow otherwise.

The same behavior is observed for embedded and bucket foundations(Gottardi et al. 1999; Villalobos et al. 2004). Because associated flow is only observed in the radial plane, the potential surface must differ from the yield surface in all terms containing vertical load. Houlsby and Cassidy (2002) suggested a non-associated potential function, described as a modification of the yield function, by introducing an association parameter, α_v, in the following way:

$$g = \left(\frac{H}{V'h_0}\right)^2 + \left(\frac{M}{V'm_0D}\right)^2 - 2a\left(\frac{H}{V'h_0}\right)\left(\frac{M}{V'm_0D}\right) - \alpha_v^2\beta_{34}\left(\frac{V}{V'}\right)^{2\beta_3}\left(\frac{V}{V'}\right)^{2\beta_4} = 0 \qquad \text{(A.II-7)}$$

$$\text{where} \quad \beta_{34} = \left[\frac{\left(\beta_3+\beta_4\right)^{(\beta_3+\beta_4)}}{\beta_3^{\beta_3}\beta_4^{\beta_4}}\right]^2$$

where V' = intersection of the plastic potential with the V-axis determined by g = 0. The value of the β factors can be chosen independently of the corresponding factors in the yield surface expression. It is noted that associated flow is obtained if $\alpha_v = 1; \beta_1 = \beta_3$; and $\beta_2 = \beta_4$.

The association parameter av has two purposes:

1. It controls the relative magnitude of the vertical displacement;

2. It controls the position of the parallel point, defined by Tan (1990), which is the peak of the potential surface. For α_v less than unity, the parallel point is moved to a lower value of V/V_{peak}.

(III) Basic equations for a plasticity model for shallow foundations in clay (Cassidy et al. 2006)

A single surface strain hardening plasticity model is proposed. It contains four components:(i) a yield surface in combined V-M-H load space that defines the boundary of elastic an plastic response, (ii) a description of elastic behaviour for any incremental changes of load within the yield surface, (iii) a hardening law that describes the change in yield surface size with embedment, and (iv) a flow rule to describe the irreversible footing displacements during the elsto-plastic event.

Yield surface

Based on finite element results, Taiebat and Carter (2000) suggested the three-dimensional failure surface of a shallow circular footing lying on the surface of homogeneous undrained soil could be described as

$$\left(\frac{V}{V_u}\right)^2+\left[\left(\frac{M}{M_u}\right)\left(1-\alpha_1\frac{HM}{H_u|M|}\right)\right]^2+\left|\left(\frac{H}{H_u}\right)^3\right|-1=0 \qquad \text{(A.III-1)}$$

where V_u, M_u and H_u are the ultimate capacities of the footing under purely vertical, moment and horizontal loads respectively, and α_1 is a shape-factor-defining eccentricity in the moment-horizontal load plane. For application to a caisson, the size of the surface under pure horizontal load (H_u) and pure moment load (M_u) can be determined using the upper-bound mechanisms of Murff and Hamilton (1993) and Randolph et al. (1998).

For that case a caisson of (scaled prototype) diameter D = 6 m and skirt length L = 3 m was tested in normally consolidated kaolin clay with increasing strength with depth of ρ≈1.25 kPa/m. The non-dimensional upper-bound value for the pure rotation case ($H=0$) was $M_u/DAs_u=0.754$ and for the horizontal translation ($M=0$) was $H_u/As_u=2.97$. Therefore, Eq. (A.III-1) can be written in a form consistent with previous force-resultant models for spudcans as:

$$(\frac{V}{V_0})^2+\left[\left(\frac{M}{m_0DAs_u}\right)\left(1-\alpha_1\frac{HM}{h_0As_u|M|}\right)\right]^2+\left|\left(\frac{H}{h_0As_u}\right)^3\right|-1=0 \qquad \text{(A.III-2)}$$

where m_0 and h_0 are dimensionless size parameters (0.754 and 2.97 respectively for the case outlined above), D and A are the caisson diameter and area, and V_0 represents the value of pure vertical bearing capacity for the current vertical penetration.

Elastic behaviour

The elastic relationship between the increments of load (*dV*, *dM*, *dH*) and the corresponding elastic displacements ($dw_e, \mathrm{d}\theta_e, du_e$) is:

$$\begin{bmatrix} dV \\ dM/D \\ dH \end{bmatrix} = DG \begin{bmatrix} k_v & 0 & 0 \\ 0 & k_m & k_c \\ 0 & k_c & k_h \end{bmatrix} \begin{bmatrix} dw_e \\ Dd\theta_e \\ du_e \end{bmatrix} \quad \text{(A.III-3)}$$

where G is a representative shear modulus and k_v, k_m, k_h, k_c are dimensionless constants. The values of these constants may be derived using, for instance, finite element analysis of a footing.

Hardening law

Traditional bearing capacity theory is used to determine the hardening law, with the vertical load–displacement relationship determined by the capacity of the footing for each level of vertical penetration. All of the penetration resistances are estimated using an undrained shear strength (s_u) profile.

There is little penetration resistance whilst the skirts are penetrating the soil (down to 3 m in this case). Therefore, before the base-plate has made contact with the soil surface ($w < h_i$), the vertical resistance is calculated as the sum of the internal and external frictional resistance plus the bearing capacity of the annulus of the skirt and is given by:

$$V = (\alpha_i D_i + \alpha_0 D_0) s_{u1} \pi w + (N_c s_{u2} + \gamma' w) \pi D_{ave} t \quad \text{(A.III-4)}$$

with α an adhesion factor (typically taken as the inverse of the soil sensitivity), h the location of the base of the skirt from the mudline, t the wall thickness, N_c a bearing capacity factor for a buried strip footing, s_{u1} the average shear strength along the skirt, s_{u2} the shear strength at the base and γ' the effective unit weight.

Once the caisson's base-plate has made contact with the soil surface (at $w = h_i$) and the installation valve closed, two type of behaviour can occur, as shown in Fig. 4. With continued installation into the seabed, failure progresses to a strain level where a bearing-capacity mechanism acting over the whole base area is reached. For this case an estimate of vertical load could be determined by:

$$V = \alpha_0 D_0 \pi L s_{u1} + N_c^* s_{u2} \frac{\pi D_0^2}{4} \quad \text{(A.III-5)}$$

where N_c^* is a bearing capacity factor for the axisymmetric case, with Randolph et al. (2004) reviewing appropriate methods to evaluate this for circular footings with varying strength profiles, roughness values and embedment. Lower bound plasticity solutions of Martin(2001, 2003) and Houlsby and Martin (2003) provide the most readily accessible values. For these factors the shear strength s_{u2} should be taken at the base of the skirts.

Eq. (A.III-5) can be used to calculate the initial bearing capacity load, but also the load once the footing penetrates plastically further into the ground. However, the use of Eq. (A.III-4) and (A.III-5) creates a stress discontinuity at the position of the baseplate touching the surface ($w = h_i$). It does not reflect the experimental evidence of the transition of load that occurs. A simple inverted parabolic transition is used to develop the full capacity after touchdown, with only the normalized initial stiffness and displacement at the point of the fully developed load requiring definition.

The other behaviour is the pullout resistance with reversal of loading once the caisson's skirts have been installed and the caisson sealed. There is initially an extremely stiff response, which can be modelled by the elastic stiffness matrix. However, once the loading reverts into tension a substantial softening of the load displacement occurs. The combination of skin friction and "reverse" end bearing on the annulus of the skirt and the base-plate must be considered (remembering the assumption of a sealed caisson). That is, the ideal vertical load–penetration curve would be:

$$V = -\alpha_0 D_0 \pi w s_{u1} - N_c^* s_{u2} \frac{\pi D_0^2}{4} \tag{A.III-6}$$

Flow rule

When the load state touches and expands (or possibly contracts) the yield surface, plastic displacements occur. Though the stiffness of the response is determined by this expansion (or contraction) through the hardening law, the ratios of the plastic displacements are determined by the flow rule. The simplest form is associated flow, where the yield surface also acts as the plastic potential, and the ratios of the plastic displacement components are determined by

$$dw_p = \lambda \frac{\partial f}{\partial V}, \quad du_p = \lambda \frac{\partial f}{\partial H}, \quad d\theta_p = \lambda \frac{\partial f}{\partial M / D} \tag{A.III-7}$$

where λ is a non-negative multiplier that can be determined from the requirement that an elastic–plastic load step must remain on the yield surface. Associated flow was observed on a caisson during a series of constant vertical-load probe tests conducted in a geotechnical centrifuge from Watson et al. (1998, 1999, 2000).

(IV) Basic equations for a hyperplasticity model focused on shallow foundations (Villalobos Jara 2006)

The present study is intended to provide experimental information to construct hyperplasticity models by means of determining for instance the yield surface and a flow rule. In order to obtain practical results hyperplastic models necessitate accurate values of the model parameters. Thus, the determination of these parameters from laboratory tests was an important objective of this investigation. The advance in theoretical modelling necessitates of advances in physical modelling as well to make possible that a mathematical theory has useful applications in geotechnical engineering.

Elasticity

In hyperplasticity theory the elastic behaviour occurs inside and on the yield surface as assumed traditionally in plasticity. An elastic load-displacement relationship can be presented in a displacement controlled form as follows:

$$\begin{bmatrix} V' \\ M \\ H \end{bmatrix} = DG \begin{bmatrix} K_V & 0 & 0 \\ 0 & K_M & K_{MH} \\ 0 & K_{MH} & K_H \end{bmatrix} \begin{bmatrix} w \\ \theta \\ u \end{bmatrix} \tag{A.IV-1}$$

where K_V , K_M , K_H and K_{MH} are the stiffness coefficients given by:

$$\begin{aligned} &K_V = 2GRk_v; \quad K_M = GR^3k_m - 8GR^2dk_{mh} + 2GRd^2k_h; \\ &K_H = 2GRk_h; \quad K_{MH} = 4GR^2k_{mh} - 2GRk_h \end{aligned} \tag{A.IV-2}$$

R is the footing radius, *d* is the distance between the assumed LRP and the point where the combined loads are applied. w, θ and u are the elastic vertical, rotational and horizontal displacements.

Yield surface

Recently, an expression of the yield surface for caisson footings has been proposed by Nguyen-Sy and Houlsby (2005). This new formulation differs from the yield function used by Cassidy (1999) since it includes the possibility for tensile vertical loads. The yield function can be expressed in a reduced form as follows:

$$y = t^2 - \beta_{12}^2 (v_1 + t_0)^{2\beta_1} (1 - v_2)^{2\beta_2} = 0 \tag{A.IV-3}$$

The horizontal and moment loads are expressed through *t* in the form of an eccentric ellipse, where for the planar case *t* is given by:

$$t = \sqrt{h^2 + m^2 - 2emh} \tag{A.IV-4}$$

where *e* is the eccentricity of the ellipse. Considering the isotropic hardening case, the dimensionless horizontal and moment loads are given by the following expressions:

$$h = \frac{a_H \chi_H + (1 - \mathrm{a_H})\,\mathrm{H}}{h_0 V_0} \quad m = \frac{a_M \chi_M + (1 - \mathrm{a}_M) M}{2Rm_0 V_0} \tag{A.IV-5}$$

The dimensionless vertical loads v_1 and v_2 are given by:

$$v_1 = \frac{a_{V_1}\chi_V + (1-a_{V_1})V'}{V_0} \quad v_2 = \frac{a_{V_2}\chi_V + (1-a_{V_2})V'}{V_0} \tag{A.IV-6}$$

χ_V , χ_M and χ_H are the dissipative generalized vertical, moment and horizontal loads, which are related to the dissipation function *d* by means of the partial derivative $\chi_i = \frac{\partial d}{\partial \dot{\alpha}_i}$ where *i* are internal variables that represent irreversible behaviour and play the role of plastic displacements under certain conditions .

Yield surface

In hyperplasticity theory the dissipation function gives origin to the yield function and the flow rule (Collins and Houlsby 1997). Therefore, there is no need to define a plastic potential function. This is a significant difference with the work hardening plasticity theory implemented for instance in Model B and Model C. The flow rule defines the direction of the irreversible displacement increments. The traditional division between elastic and plastic as reversible and irreversible is not necessarily true because of the dependency of stiffness on the internal variable in coupled materials. However, an associated flow rule in generalized load space holds always and plastic displacement increments are obtained according to:

$$\partial\dot{\alpha}_i = \lambda \frac{\partial y}{\partial \chi_i} \tag{A.IV-7}$$

where λ is a positive scalar multiplier that accounts for the magnitude of the velocity vectors. The α_i components are known generically as internal state variables and are related with irreversible processes, for this reason they are related with χ_i by means of the dissipation function.

The non-associated flow rule can be expressed in hyperplasticity as:

$$\begin{Bmatrix} \dot{\alpha}_V \\ \dot{\alpha}_M \\ \dot{\alpha}_H \end{Bmatrix} = \lambda \begin{Bmatrix} \frac{\partial y}{\partial \chi_V} \\ \frac{\partial y}{\partial \chi_M} \\ \frac{\partial y}{\partial \chi_H} \end{Bmatrix} \tag{A.IV-8}$$

Once the derivatives are obtained in true load space the internal variable increments have the following expressions:

$$\begin{aligned} \dot{\alpha}_V &= \lambda \frac{\partial y}{\partial \chi_V} = \lambda \frac{2\beta_{12}^2}{V_0}(v_1 + t_0)^{2\beta_1}(1-v_2)^{2\beta_2}\left\{\frac{\beta_2 a v_2}{1-v_2} - \frac{\beta_1 a v_1}{v_1 + t_0}\right\} \\ \dot{\alpha}_M &= \lambda \frac{\partial y}{\partial \chi_M} = \lambda \frac{2a_M}{2Rm_0V_0}(m - eh) \\ \dot{\alpha}_H &= \lambda \frac{\partial y}{\partial \chi_H} = \lambda \frac{2a_H}{h_0V_0}(h - em) \end{aligned} \tag{A.IV-9}$$

(V) Basic equations for a plasticity model for caisson foundations under general monotonic and cyclic loading (Foglia et al. 2015)

The original model consists of five elements: yield surface, plastic potential, hardening law, flow rule and an elastic matrix. These elements are combined to form the flexibility matrix which relates the vector of normalized incremental displacements, $d\mathbf{q}$, to the vector of normalized incremental forces, $d\mathbf{Q}$, both referring to the load reference.

Variables **q** and **Q** are defined as follows:

$$\boldsymbol{q} = \begin{pmatrix} \eta \\ \varepsilon \\ \zeta \end{pmatrix} = V_M \begin{pmatrix} w \\ u\mu \\ \psi D\theta \end{pmatrix} \tag{A.V-1}$$

$$\boldsymbol{Q} = \begin{pmatrix} \xi \\ h \\ m \end{pmatrix} = \frac{1}{V_M} \begin{pmatrix} V \\ H/\mu \\ M/(D\psi) \end{pmatrix} \tag{A.V-2}$$

In Eqs. (A.V-1) and (A.V-2), w is the vertical displacement, u is the horizontal displacement, θ is the rotation while μ and ψ are constitutive, dimensionless, parameters of the model. In the following subsections the sole equations used in this study are provided and readers are invited to refer to Nova and Montrasio (1991) for details on the original model.

Yield surface

The equation of the yield surface is as follows:

$$f = h^2 + m^2 - (\xi + t_s\rho_c)^2 \left(1 - \frac{\xi}{\rho_c}\right)^{2\beta} \tag{A.V-3}$$

where ρ_c is the hardening parameter, and β is a parameter which was introduced to improve the fit of the equation to the available experimental data. The parameter t_s, introduced to account for the skirt about the foundation perimeter, enhances the deviatoric load capacity of the foundation at low value of vertical load and allow for vertical tensile loads to be sustained by the soil-foundation system. The equation is similar to that proposed in Villalobos et al. (2009) for caisson foundation on sand.

Hardening law

The hardening law is the rule which governs the evolution of the hardening parameter, $d\rho_c$ as a function of plastic displacement and is given by the following equation:

$$d\rho_c = (1 - \rho_c)\frac{R_0}{V_M}\left(d\eta + \frac{\alpha|d\varepsilon|}{\mu} + \frac{\gamma|d\zeta|}{\psi}\right) \tag{A.V-4}$$

where α and γ are constitutive dimensionless parameters. According to the original model, parameter R_0 coincides with the initial stiffness on the vertical displacement and vertical load curve.

Flow rule

The plastic potential is based on the original model, suitably adjusted to allow for the inclusion of parameter t_s and is defined as follows:

$$g = (\mathrm{h}\,\lambda)^2 + (\mathrm{m}\,\chi)^2 - (\xi + \mathrm{t_s}\,\rho_\mathrm{g})^2 (1 - \frac{\xi}{\rho_\mathrm{g}})^{2\beta} \qquad \text{(A.V-5)}$$

where ρ_g is a fictitious variable and λ as well as χ are constitutive dimensionless parameters.

When the conditions $f = 0$ and $df = 0$ are fulfilled, the incremental plastic displacements is expressed by the equation:

$$dq_p = \Lambda \frac{\partial g}{\partial Q} \qquad \text{(A.V-6)}$$

where Λ is the plastic multiplier.

(VI) Basic equations for a plasticity model for caisson foundations under general monotonic and cyclic loading (Skau et al. 2018)

The elastic stiffness matrix

The elastic stiffness matrix is defined as a 3×3 matrix:

$$D = \begin{bmatrix} k_v^e & 0 & 0 \\ 0 & k_h^e & 0 \\ 0 & 0 & k_\theta^e \end{bmatrix} \tag{A.VI-1}$$

The stiffness coefficients k_v^e, k_h^e and k_θ^e refer to the elastic stiffness in the vertical direction, horizontal direction and rotation around the out of plane axis. The coupling terms are set to zero since the LRP is located below mudline and implicitly includes parts of the coupling between the horizontal load and moment applied at seabed. This is an approximation, and it will be shown later that z_{LRP} varies as function of the mobilization level.

Yield function and flow rule

The yield function and the flow rule are formulated based on the FEA results as those shown earlier in the paper. As stated initially, it is an aim to formulate the macroelement mathematically transparent and simple. The macroelement is intended for OWT foundations, where low and moderate mobilization levels are most relevant. An elliptic surface is therefore taken as the potential function, g. It was also chosen to use these surfaces as yield surfaces. The yield function *f* is then given by the same function imposing associated flow, for all surfaces *i* :

$$\frac{\partial g_i}{\partial F} = \frac{\partial f_i}{\partial F} \tag{A.VI-2}$$

where f_i is an ellipsoid:

$$f_i = \left(\frac{V - \alpha_{i,V}}{V_{i,\max}} \right)^2 + \left(\frac{H - \alpha_{i,H}}{H_{i,\max}} \right)^2 + \left(\frac{M - \alpha_{i,M}}{M_{i,\max}} \right)^2 - 1 \tag{A.VI-3}$$

The denominators $V_{i,\max}$, $H_{i,\max}$ and $M_{i,\max}$ are the axis crossings for the surface i. $\alpha_{i,V}$, $\alpha_{i,H}$, $\alpha_{i,M}$ are the coordinates of the origin (initially equal zero) of surface *i*. Compared to other yield surface formulations (Byrne and Cassidy 2002; Bienen et al. 2006; Cassidy et al. 2006), the function cannot describe rotated ellipses. However, this is accounted for by keeping the depth of the load

reference point (z_{LRP}) as an input. This will effectively describe the same response at seabed. The values of $V_{i,\max}$, $H_{i,\max}$ and $M_{i,\max}$ will determine the shape of the ellipses, thus the flow direction. The values should therefore be determined based on the development of plastic work along the three axes.

Hardening rule

The hardening is a multilinear approximation. This means that each surface, *i* has a constant "plastic stiffness". The total plastic displacement is taken as sum of all plastic displacement contributions using the Koiter (1953):

$$du^p = \sum_{i=1}^{k} du_i^p = \sum_{i=1}^{k} d\lambda_i \cdot \partial g_i / \partial F \tag{A.VI-4}$$

where *k* is the outermost surface being violated. Since the foundation response is anisotropic by nature, an anisotropic hardening formulation has been adapted. The hardening is based on the load – displacement response in the three uniaxial directions. The approach of using the three uniaxial responses as basis for describing general response to any load path, was illustrated in Skau et al. (2017). In this formulation, the hardening for a combined load path is approximated by weighting the plastic stiffness in the three uniaxial directions by the flow direction for the current load state. The formulation, also used for modelling clay in Ref Grimstad et al. (2014), can be expressed for any surface *i* as:

$$\partial \alpha_i / \partial \lambda_i = D_i^p \cdot \partial g_i / \partial F \tag{A.VI-5}$$

where $\partial g_i / \partial F$ is the plastic flow direction vector, and D_i^p is the "plastic stiffness matrix" for surface, *i* :

$$D_i^p = \begin{bmatrix} k_{i,v}^p & 0 & 0 \\ 0 & k_{i,h}^P & 0 \\ 0 & 0 & k_{i,u\theta}^p \end{bmatrix} \tag{A.VI-6}$$

$k_{i,v}^p$, $k_{i,h}^p$, $k_{i,u\theta}^p$ refer to the plastic stiffness in the vertical direction, horizontal direction and rotation around the out of plane axis. Note that the plastic stiffness, D_i^p, is only associated with the translation of surface *i*. This means that e.g. the vertical tangential stiffness $k_{k,v}^p$, for loading between

$V_{k,\max}$ and $V_{k+1,\max}$ is the combined stiffness from all surfaces being translated. This is analogue to the total stiffness of 1D-springs coupled in series:

$$\frac{1}{k_{k,v}^{p}} = \sum_{i+1}^{k} \frac{1}{k_{i,v}^{p}} \tag{A.VI-7}$$

Macroelement input

The input has been limited to ensure simplicity for users. With the exception of numerical parameters such as tolerance and number of substeps, the input is limited to:

- The depth of the load reference point, z_{LRP}. The depth where negligible horizontal displacement evolves when a moment load is applied to the foundation.
- The uniaxial response – for loads applied in the load reference point. In total three curves V – u_v, H – u_h, M - u_θ, as tabulated data.
- Number of surfaces, N

References

ABAQUS, I. (2014). "Abaqus documentation." Version **6**: 5-1.

Achmus, M., C. T. Akdag and K. Thieken (2013). "Load-bearing behavior of suction bucket foundations in sand." Applied Ocean Research **43**: 157-165.

Allersma, H., A. Kirstein, R. Brinkgreve and T. Simon (1999). "Centrifuge and numerical modelling of horizontally loaded suction piles." The Ninth International Offshore and Polar Engineering Conference, International Society of Offshore and Polar Engineers **1**: 711-717.

Allersma, H., F. Plenevaux and J.-F. Wintgens (1997). "Simulation of suction pile installation in sand in a geocentrifuge." The Seventh International Offshore and Polar Engineering Conference, International Society of Offshore and Polar Engineers: 761-766.

Andersen, K. H., H. P. Jostad and R. Dyvik (2008). "Penetration resistance of offshore skirted foundations and anchors in dense sand." Journal of geotechnical and geoenvironmental engineering **134**(1): 106-116.

Bagheri, P., S. W. Son and J. M. Kim (2017). "Investigation of the load-bearing capacity of suction caissons used for offshore wind turbines." Applied Ocean Research **67**: 148-161.

Balmforth, N. and R. Kerswell (2005). "Granular collapse in two dimensions." Journal of Fluid Mechanics **538**: 399-428.

Barari, A. and L. B. Ibsen (2012). "Undrained response of bucket foundations to moment loading." Applied Ocean Research **36**: 12-21.

Bell, R. W. (1991). "The analysis of offshore foundations subjected to combined loading." M. SC, Thesis, University of Oxford.

Benz, T. (2007). "Small-strain stiffness of soils and its numerical consequences", PhD Thesis, Univ. Stuttgart, Inst. f. Geotechnik Stuttgart.

Bienen, B., B. Byrne, G. Houlsby and M. Cassidy (2006). "Investigating six-degree-of-freedom loading of shallow foundations on sand." Géotechnique **56**(6): 367-380.

Bojanowski, C. (2014). "Numerical modeling of large deformations in soil structure interaction problems using FE, EFG, SPH, and MM-ALE formulations." Archive of Applied Mechanics **84**: 743-755.

Bransby, M. and G.-J. Yun (2009). "The undrained capacity of skirted strip foundations under combined loading." Géotechnique **59**(2): 115-125.

Bui, H. H., R. Fukagawa, K. Sako and S. Ohno (2008). "Lagrangian meshfree particles method (SPH) for large deformation and failure flows of geomaterial using elastic–plastic soil constitutive model." International Journal for Numerical and Analytical Methods in Geomechanics **32**(12): 1537-1570.

Buscarnera, G., R. Nova, M. Vecchiotti, C. Tamagnini and D. Salciarini (2010). "Settlement analysis of wind turbines." Soil-Foundation-Structure Interaction. CRC Press.

Butterfield, R. (1979). "The use of physical models in design." Proc. 7th European Regional Conf. on SMFE **4**: 318-323.

Byrne, B. and M. Cassidy (2002). "Investigating the response of offshore foundations in soft clay soils." ASME 2002 21st International Conference on Offshore Mechanics and Arctic Engineering, American Society of Mechanical Engineers. OMAE2002-28057.

Byrne, B. and G. Houlsby (1999). "Drained behaviour of suction caisson foundations on very dense sand." Offshore Technology Conference, Houston, paper 10994.

Byrne, B. and G. Houlsby (2001). "Observations of footing behaviour on loose carbonate sands." Géotechnique **51**(5): 463-466.

Byrne, B. and G. Houlsby (2003). "Foundations for offshore wind turbines." Philosophical Transactions of the Royal Society of London A: Mathematical, Physical and Engineering Sciences **361**(1813): 2909-2930.

Byrne, B. W. (2000). "Investigations of suction caissons in dense sand", Ph. D thesis, University of Oxford Oxford, UK.

Cao, J. (2003). "Centrifuge modeling and numerical analysis of the behaviour of suction caissons in clay", PhD Thesis, Memorial University of Newfoundland.

Cassidy, M., B. Byrne and G. Houlsby (2002). "Modelling the behaviour of circular footings under combined loading on loose carbonate sand." Géotechnique **52**(10): 705-712.

Cassidy, M., B. Byrne and M. Randolph (2004). "A comparison of the combined load behaviour of spudcan and caisson foundations on soft normally consolidated clay." Géotechnique **54**(2): 91-106.

Cassidy, M., M. Randolph and B. Byrne (2006). "A plasticity model describing caisson behaviour in clay." Applied Ocean Research **28**(5): 345-358.

Cassidy, M. J. (1999). "Non-linear analysis of jack-up structures subjected to random waves." Ph. D thesis, Oxford University.

Cerfontaine, B., R. Charlier and F. Collin (2016). "Transient behaviour of a suction caisson in sand: axisymmetric numerical modelling." Report-Liège University.

Cerfontaine, B., F. Collin, R. Charlier, I. Nowadays and E. Union (2015). "Numerical modelling of transient cyclic vertical loading of suction caissons in sand." Géotechnique **66**(2): 121-136.

Chatzigogos, C., R. Figini, A. Pecker and J. Salençon (2011). "A macroelement formulation for shallow foundations on cohesive and frictional soils." International Journal for Numerical and Analytical Methods in Geomechanics **35**(8): 902-931.

Chatzigogos, C., A. Pecker and J. Salencon (2009). "Macroelement modeling of shallow foundations." Soil Dynamics and Earthquake Engineering **29**(5): 765-781.

Cheng, X., J. Wang and Z. Wang (2016). "Incremental elastoplastic FEM for simulating the deformation process of suction caissons subjected to cyclic loads in soft clays." Applied Ocean Research **59**: 274-285.

Clukey, E., M. Morrison, J. Gamier and J. Corté (1995). "The response of suction caissons in normally consolidated TLP loading conditions." Offshore Technology Conference, Houston, paper OTC 7796.

Clukey, E. C. and M. J. Morrison (1993). "A centrifuge and analytical study to evaluate suction caissons for TLP applications in the Gulf of Mexico." Design and performance of deep foundations: Piles and piers in soil and soft rock, ASCE **38**: 141-156.

Collins, I. and G. Houlsby (1997). "Application of thermomechanical principles to the modelling of geotechnical materials." Proceedings of the royal society of London A: Mathematical, physical and engineering sciences, The Royal Society **453**.

Cox, J. A., S. Bhattacharya, D. Lombardi and D. M. Wood Muir Wood (2013). "Dynamics of offshore wind turbines supported on two foundations." Proceedings of the ICE - Geotechnical Engineering **166**: 159-169.

Cremer, C., A. Pecker and L. Davenne (2001). "Cyclic macro‐element for soil–structure interaction: material and geometrical non‐linearities." International Journal for Numerical and Analytical Methods in Geomechanics **25**(13): 1257-1284.

Cremer, C., A. Pecker and L. Davenne (2002). "Modelling of nonlinear dynamic behaviour of a shallow strip foundation with macro-element." Journal of Earthquake Engineering **6**(02): 175-211.

Crosta, G., S. Imposimato and D. Roddeman (2009). "Numerical modeling of 2 - D granular step collapse on erodible and nonerodible surface." Journal of Geophysical Research: Earth Surface **114**(F3).

Daerr, A. and S. Douady (1999). "Sensitivity of granular surface flows to preparation." EPL (Europhysics Letters) **47**(3): 324-330.

Deng, W. and J. Carter (2002). "A theoretical study of the vertical uplift capacity of suction caissons." International Journal of Offshore and Polar Engineering **12**(02): 342-349.

di Prisco, C., M. R. Massimino, M. Maugeri, M. Nicolosi and R. Nova (2006). "Cyclic numerical analyses of Noto Cathedral: soil-structure interaction modelling." Rivista Italiana di Geotecnica **48**: 49-64.

di Prisco, C., R. Nova, F. Perotti and A. Sibilia (2004). "Analysis of soil-foundation interaction of tower structures under cyclic loading." In Geotechnical analysis of the Seismic Vulnerability of Historical Monuments. Maugeri, M., Nova, R., Eds. Pàtron: 123-136.

di Prisco, C., R. Nova and A. Sibilia (2003). "Shallow footings under cyclic loading: experimental behaviour and constitutive modelling." In Geotechnical analysis of the Seismic Vulnerability of Historical Monuments. Maugei M, Nova R, Eds. Pàton, 2003: 99-121.

DNV, D. N. V. (2013). "Design of offshore wind turbine structures." Standard DNV-OSJ101, Det Norske Veritas AS (DNV).

Doherty, J. and A. Deeks (2003). "Elastic response of circular footings embedded in a non-homogeneous half-space." Géotechnique **53**(8): 703-714.

El-Gharbawy, S. and R. Olson (2000). "Modeling of suction caisson foundations." The Tenth International Offshore and Polar Engineering Conference, International Society of Offshore and Polar Engineers. Seattle, Washington, USA.

Erbrich, C. T. and T. I. Tjelta (1999). "Installation of bucket foundations and suction caissons in sand-geotechnical performance." Offshore technology conference, Houston, paper OTC 10990.

Figini, R., R. Paolucci and C. Chatzigogos (2012). "A macro - element model for non - linear soil – shallow foundation – structure interaction under seismic loads: theoretical development and experimental validation on large scale tests." Earthquake Engineering & Structural Dynamics **41**(3): 475-493.

Filippou, F. C. and M. Constantinides (2004). "FEDEASLab getting started guide and simulation examples." NEESgrid Report **22**: 2004-2005.

Foglia, A., G. Gottardi, L. Govoni and L. B. Ibsen (2015). "Modelling the drained response of bucket foundations for offshore wind turbines under general monotonic and cyclic loading." Applied Ocean Research **52**: 80-91.

Foglia, A. and L. B. Ibsen (2013). "A Similitude Theory for Bucket Foundations Under Monotonic Horizontal Load in Dense Sand." Geotechnical and Geological Engineering **31**: 133-142.

Frederick, C. O. and P. Armstrong (2007). "A mathematical representation of the multiaxial Bauschinger effect." Materials at High Temperatures **24**(1): 1-26.

Fuglsang, L. and J. Steensen-Bach (1991). "Breakout resistance of suction piles in clay." Proceedings of the international conference: centrifuge. Rotterdam, The Netherlands. 153-159.

Gajan, S. (2006). "Physical and numerical modeling of nonlinear cyclic load-deformation behavior of shallow foundations supporting rocking shear walls", PhD Thesis, University of California, Davis.

Gajan, S. and B. L. Kutter (2009). "Contact interface model for shallow foundations subjected to combined cyclic loading." Journal of Geotechnical and Geoenvironmental Engineering **135**(3): 407-419.

Gerolymos, N., A. Zafeirakos and K. Karapiperis (2015). "Generalized failure envelope for caisson foundations in cohesive soil: static and dynamic loading." Soil Dynamics and Earthquake Engineering **78**: 154-174.

Gerolymos, N., A. Zafeirakos and C. Souliotis (2012). "Insight to failure mechanisms of caisson foundations under combined loading: A macro-element approach." Proc. 2nd Int. Conf. on Performance-based design in Earthquake Geotechnical Engineering, Taormina, Italy.

Giannakos, S., N. Gerolymos and G. Gazetas (2012). "Cyclic lateral response of piles in dry sand: Finite element modeling and validation." Computers and Geotechnics **44**: 116-131.

Gingold, R. A. and J. J. Monaghan (1977). "Smoothed particle hydrodynamics: theory and application to non-spherical stars." Monthly Notices of the Royal Astronomical Society **181**: 375-389.

Girolami, L., V. Hergault, G. Vinay and A. Wachs (2012). "A three-dimensional discrete-grain model for the simulation of dam-break rectangular collapses: comparison between numerical results and experiments." Granular Matter **14**(3): 381-392.

Gottardi, G. and R. Butterfield (1993). "On the bearing capacity of surface footings on sand under general planar loads." Soils and Foundations **33**(3): 68-79.

Gottardi, G. and G. Houlsby (1995). "Model tests of circular footings on sand subjected to combined loads." Report-University of Oxford Department of Engineering Science.

Gottardi, G., G. Houlsby and R. Butterfield (1999). "Plastic response of circular footings on sand under general planar loading." Géotechnique **49**(4): 453-470.

Gourvenec, S. (2008). "Effect of embedment on the undrained capacity of shallow foundations under general loading." Géotechnique **58**(3): 177-186.

Gourvenec, S. and S. Barnett (2011). "Undrained failure envelope for skirted foundations under general loading." Géotechnique **61**(3): 263-270.

Gourvenec, S. and M. Randolph (2003). "Effect of strength non-homogeneity on the shape of failure envelopes for combined loading of strip and circular foundations on clay." Géotechnique **53**(6): 575-586.

Grange, S., P. Kotronis and J. Mazars (2008). "A macro ‐ element for a circular foundation to simulate 3D soil–structure interaction." International Journal for Numerical and Analytical Methods in Geomechanics **32**(10): 1205-1227.

Grange, S., P. Kotronis and J. Mazars (2009). "A macro-element to simulate 3D soil–structure interaction considering plasticity and uplift." International Journal of Solids and Structures **46**(20): 3651-3663.

Grimstad, G., L. Andresen and H. P. Jostad (2012). "NGI ‐ ADP: Anisotropic shear strength model for clay." International Journal for Numerical and Analytical Methods in Geomechanics **36**(4): 483-497.

Grimstad, G., J. Rønningen and H. Nøst (2014). "Use of IWAN models for modelling anisotropic and cyclic behavior of clays." Numer Meth Geotech Eng **1**: 49-55.

Hansen, J. B. (1970). "A revised and extended formula for bearing capacity." Copenhagen: Danish Geotechnical Institute **28**: 5-11.

Harireche, O., M. Mehravar and A. M. Alani (2013). "Suction caisson installation in sand with isotropic permeability varying with depth." Applied Ocean Research **43**: 256-263.

Hibbitt, Karlsson and Sorensen (2001). ABAQUS/Explicit: User's Manual, Hibbitt, Karlsson and Sorenson Incorporated.

Hogervorst, J. R. (1980). "Field trails with large diameter suction piles. " Offshore Technology Conference, Houston, paper 3817, 217-224.

Houlsby, G. (2005). "The theoretical modelling of circular shallow foundation for offshore wind turbines", Ph. D thesis, University of Oxford.

Houlsby, G. and B. Byrne (2004). "Calculation procedures for installation of suction caissons." Report No. OUEL2268/04, University of Oxford.

Houlsby, G. and M. Cassidy (2002). "A plasticity model for the behaviour of footings on sand under combined loading." Géotechnique **52**(2): 117-129.

Houlsby, G. and C. Martin (2003). "Undrained bearing capacity factors for conical footings on clay." Géotechnique **53**(5): 513-520.

Houlsby, G. T., L. B. Ibsen and B. W. Byrne (2005). "Suction caissons for wind turbines." Frontiers in Offshore Geotechnics: ISFOG, Perth, WA, Australia: 75-93.

Houlsby, G. T., R. B. Kelly, J. Huxtable and B. W. Byrne (2005). "Field trials of suction caissons in clay for offshore wind turbine foundations." Géotechnique **55**: 287-296.

Houlsby, G. T., R. B. Kelly, J. Huxtable and B. W. Byrne (2006). "Field trials of suction caissons in sand for offshore wind turbine foundations." Géotechnique **56**: 3-10.

Houlsby, G. T. and A. M. Puzrin (2007). "Principles of hyperplasticity: an approach to plasticity theory based on thermodynamic principles", Springer Science & Business Media.

Ibsen, L. B. (2008). "Implementation of a new foundations concept for offshore wind farms." Nordisk Geoteknikermøte, Norsk Geoteknisk Forening: 19-33.

Ibsen, L. B., A. Barari and K. A. Larsen (2013). "Adaptive plasticity model for bucket foundations." Journal of Engineering Mechanics **140**(2): 361-373.

Ibsen, L. B., A. Barari and K. A. Larsen (2015). "Effect of Embedment on the Plastic Behavior of Bucket Foundations." Journal of Waterway, Port, Coastal & Ocean Engineering **141**: 1-9.

Ibsen, L. B., M. Hanson, T. Hjort and M. Thaarup (2009). "Mc-parameter calibration of baskarp sand no. 15", Technical report No. 62, Department of Civil Engineering, Aalborg University.

Ibsen, L. B., K. a. Larsen and a. Barari (2014). "Calibration of Failure Criteria for Bucket Foundations on Drained Sand under General Loading." Journal of Geotechnical and Geoenvironmental Engineering **140**(7): 04014033.

Ibsen, L. B., S. Liingaard and S. A. Nielsen (2005). "Bucket Foundation, a status." Proceedings of the Copenhagen Offshore Wind, 26-28 Octorber, Copenhagan DK.

Iskander, M., S. El-Gharbawy and R. Olson (2002). "Performance of suction caissons in sand and clay." Canadian Geotechnical Journal **39**: 576-584.

Jin, Y.-F., Z.-X. Wu, Z.-Y. Yin and J. S. Shen (2017). "Estimation of critical state-related formula in advanced constitutive modeling of granular material." Acta Geotechnica: 1-23.

Jin, Y.-F., Z.-Y. Yin, S.-L. Shen and P.-Y. Hicher (2016). "Investigation into MOGA for identifying parameters of a critical-state-based sand model and parameters correlation by factor analysis." Acta Geotechnica **11**(5): 1131-1145.

Jin, Y.-F., Z.-Y. Yin, S.-L. Shen and P.-Y. Hicher (2016). "Selection of sand models and identification of parameters using an enhanced genetic algorithm." International Journal for Numerical and Analytical Methods in Geomechanics **40**: 1219-1240.

Jin, Y.-F., Z.-Y. Yin, S.-L. Shen and D.-M. Zhang (2017). "A new hybrid real-coded genetic algorithm and its application to parameters identification of soils." Inverse Problems in Science and Engineering **25**(9): 1343-1366.

Jin, Y.-F., Z.-Y. Yin, Z.-X. Wu and W.-H. Zhou (2018). "Identifying parameters of easily crushable sand and application to offshore pile driving." Ocean Engineering **154**: 416-429.

Jin, Y. F., Z. Y. Yin, S. L. Shen and P. Y. Hicher (2016). "Selection of sand models and identification of parameters using an enhanced genetic algorithm." International Journal for Numerical and Analytical Methods in Geomechanics **40**(8): 1219-1240.

Jin, Z., Z.-Y. Yin, P. Kotronis and Y.-F. Jin (2018). "Numerical investigation on evolving failure of caisson foundation in sand using the combined Lagrangian-SPH method." Marine Georesources & Geotechnology: 1-13.

Kafle, B. and F. Wuttke (2013). "Cyclic macroelement for shallow footing over unsaturated soil." Advances in unsaturated soils, Taylor and Francis: 521-526.

Kelly, R., G. Houlsby and B. Byrne (2006). "A comparison of field and laboratory tests of caisson foundations in sand and clay." Géotechnique **56**(9):617-626.

Kermani, E., T. Qiu and T. Li (2015). "Simulation of collapse of granular columns using the discrete element method." International Journal of Geomechanics **15**(6): 04015004.

Kim, D.-J., Y. W. Choo, J.-H. Kim, S. Kim and D.-S. Kim (2014). "Investigation of monotonic and cyclic behavior of tripod suction bucket foundations for offshore wind towers using centrifuge modeling." Journal of Geotechnical and Geoenvironmental Engineering **140**(5): 04014008.

Kim, Y., K. Kim, Y. Cho, S. Bang and K. Jones (2005). "Centrifuge model tests on embedded suction anchors." The Fifteenth International Offshore and Polar Engineering Conference, International Society of Offshore and Polar Engineers, Seoul, Korea: 431-435.

Koiter, W. T. (1953). "Stress-strain relations, uniqueness and variational theorems for elastic-plastic materials with a singular yield surface." Quarterly of applied mathematics **11**(3): 350-354.

Kolymbas, D. (1991). "An outline of hypoplasticity." Archive of applied mechanics **61**(3): 143-151.

Lacaze, L., J. C. Phillips and R. R. Kerswell (2008). "Planar collapse of a granular column: Experiments and discrete element simulations." Physics of Fluids **20**(6): 063302.

Lajeunesse, E., A. Mangeney-Castelnau and J. Vilotte (2004). "Spreading of a granular mass on a horizontal plane." Physics of Fluids **16**(7): 2371-2381.

Lajeunesse, E., J. Monnier and G. Homsy (2005). "Granular slumping on a horizontal surface." Physics of fluids **17**(10): 103302.

Larsen, K. A., L. B. Ibsen and A. Barari (2013). "Modified expression for the failure criterion of bucket foundations subjected to combined loading." Canadian Geotechnical Journal **50**(12): 1250-1259.

Le Pape, Y. and J. G. Sieffert (2001). "Application of thermodynamics to the global modelling of shallow foundations on frictional material." International Journal for Numerical and Analytical Methods in Geomechanics **25**(14): 1377-1408.

Lesny, K. (2010). "Foundations for offshore wind turbines: tools for planning and design", VGE Verlag GmbH.

Li, D., Y. Zhang, L. Feng and Y. Gao (2015). "Capacity of modified suction caissons in marine sand under static horizontal loading." Ocean Engineering **102**: 1-16.

Li, S. and W. K. Liu (2002). "Meshfree and particle methods and their applications." Applied Mechanics Reviews **55**: 1-34.

Li, Z., P. Kotronis and S. Escoffier (2014). "Numerical study of the 3D failure envelope of a single pile in sand." Computers and Geotechnics **62**.

Li, Z., P. Kotronis, S. Escoffier and C. Tamagnini (2016). "A hypoplastic macroelement for single vertical piles in sand subject to three-dimensional loading conditions." Acta Geotechnica **11**(2): 373-390.

Li, Z., P. Kotronis, S. Escoffier and C. Tamagnini (2018). "A hypoplastic macroelement formulation for single batter piles in sand." International Journal for Numerical and Analytical Methods in Geomechanics **42**(12): 1346-1365.

Liingaard, M. (2006). "Dynamic behaviour of suction caissons", Aalborg University, Department of Civil Engineering, Division of Water and Soil.

Liu, M., M. Yang and H. Wang (2014). "Bearing behavior of wide-shallow bucket foundation for offshore wind turbines in drained silty sand." Ocean Engineering **82**: 169-179.

Lu, X., Y. Wu, B. Jiao and S. Wang (2007). "Centrifugal experimental study of suction bucket foundations under dynamic loading." Acta Mechanica Sinica **23**(6): 689-698.

Lube, G., H. E. Huppert, R. S. J. Sparks and A. Freundt (2005). "Collapses of two-dimensional granular columns." Physical Review E **72**(4): 041301.

Lube, G., H. E. Huppert, R. S. J. Sparks and A. Freundt (2007). "Static and flowing regions in granular collapses down channels." Physics of Fluids **19**(4): 043301.

Lube, G., H. E. Huppert, R. S. J. Sparks and M. A. Hallworth (2004). "Axisymmetric collapses of granular columns." Journal of Fluid Mechanics **508**: 175-199.

Martin, C. (2003). "New software for rigorous bearing capacity calculations." Proc. British Geotech. Assoc. Int. Conf. on Foundations, Dundee: 581-592.

Martin, C. and G. Houlsby (2000). "Combined loading of spudcan foundations on clay: laboratory tests." Géotechnique **50**(4): 325-338.

Martin, C. and G. Houlsby (2001). "Combined loading of spudcan foundations on clay: numerical modelling." Géotechnique **51**(8): 687-699.

Martin, C. and X. ICSMGE (2001). "Vertical bearing capacity of skirted circular foundations on Tresca soil." Proceeding 15th International Conference of Soil Mechanics and geotechnical engineering **1**: 743-746.

Martin, C. M. (1994). "Physical and numerical modelling of offshore foundations under combined loads", Ph. D thesis, University of Oxford.

Meyerhof, G. t. (1953). "The bearing capacity of foundations under eccentric and inclined loads." Proc. of the 3rd Int. Conf. on SMFE (1): 440-445.

Montrasio, L. and R. Nova (1997). "Settlements of shallow foundations on sand: geometrical effects." Géotechnique **47**(1): 49-60.

Murff, J. D. and J. M. Hamilton (1993). "P-ultimate for undrained analysis of laterally loaded piles." Journal of Geotechnical Engineering **119**(1): 91-107.

Ngo-Tran, C. L. (1996). "The analysis of offshore foundations subjected to combined loading", Ph. D thesis, University of Oxford.

Nguyen-Sy, L. (2005). "The theoretical modelling of circular shallow foundation for offshore wind turbines", Ph. D thesis,University of Oxford.

Nguyen-Sy, L. and G. T. Houlsby (2005). "The theoretical modelling of a suction caisson foundation using hyperplasticity theory." Frontiers in Offshore Geotechnics II, Perth: 417.

Niemunis, A. (2003). "Extended hypoplastic models for soils", Habilitation Thesis, Inst. für Grundbau und Bodenmechanik.

Niemunis, A. and I. Herle (1997). "Hypoplastic model for cohesionless soils with elastic strain range." Mechanics of Cohesive‐frictional Materials: An International Journal on Experiments, Modelling and Computation of Materials and Structures **2**(4): 279-299.

Nova, R. and L. Montrasio (1991). "Settlements of shallow foundations on sand." Géotechnique **41**(2): 243-256.

Ntritsos, N., I. Anastasopoulos and G. Gazetas (2015). "Static and cyclic undrained response of square embedded foundations." Géotechnique **65**(10): 805-823.

Ortiz, M. and J. Simo (1986). "An analysis of a new class of integration algorithms for elastoplastic constitutive relations." International Journal for Numerical Methods in Engineering **23**(3): 353-366.

Paolucci, R. (1997). "Simplified evaluation of earthquake-induced permanent displacements of shallow foundations." Journal of Earthquake Engineering **1**(03): 563-579.

Park, J.-S., D. Park and J.-K. Yoo (2016). "Vertical bearing capacity of bucket foundations in sand." Ocean Engineering **121**: 453-461.

Poulos, H. G. and E. H. Davis (1974). "Elastic solutions for soil and rock mechanics", John Wiley, New York.

Qiu, G., S. Henke and J. Grabe (2009). "Applications of coupled Eulerian–Lagrangian method to geotechnical problems with large deformations." Proceeding of SIMULIA customer conference**:** 420-435.

Raines, R. D. and J. Garnier (2004). "Physical modeling of suction piles in clay." ASME 2004 23rd International Conference on Offshore Mechanics and Arctic Engineering, American Society of Mechanical Engineers: 1-11.

Randolph, M., S. Gourvenec, D. White and M. Cassidy (2011). "Offshore geotechnical engineering", Spon Press New York.

Randolph, M., M. Jamiolkowski and L. Zdravkovic (2004). "Load carrying capacity of foundations." Proc. Skempton Memorial Conf., London (1): 207-240.

Randolph, M., M. O'neill, D. Stewart and C. Erbrich (1998). "Performance of suction anchors in fine-grained calcareous soils." Offshore technology conference, Houston, OTC 8831.

Renzi, R., W. Maggioni, F. Smits and V. Manes (1991). "A centrifugal study on the behavior of suction piles." Proc. Int. Conf. on Centrifuge Modelling-Centrifuge, 169-176.

Salciarini, D. and C. Tamagnini (2009). "A hypoplastic macroelement model for shallow foundations under monotonic and cyclic loads." Acta Geotechnica **4**(3): 163-176.

Senders, M. (2009). "Suction caissons in sand as tripod foundations for offshore wind turbines", Ph. D thesis, University of Western Australia.

Senders, M. and M. Randolph (2009). "CPT-Based Method for the Installation of Suction Caissons in Sand." Journal of Geotechnical and Geoenvironmental Engineering **135**: 14-25.

Shen, S.-L., H.-N. Wu, Y.-J. Cui and Z.-Y. Yin (2014). "Long-term settlement behaviour of metro tunnels in the soft deposits of Shanghai." Tunnelling and Underground Space Technology **40**: 309-323.

Shen, S.-L., Y.-X. Wu and A. Misra (2017). "Calculation of head difference at two sides of a cut-off barrier during excavation dewatering." Computers and Geotechnics **91**: 192-202.

Sheng, D., S. Sloan and H. Yu (2000). "Aspects of finite element implementation of critical state models." Computational mechanics **26**(2): 185-196.

Shirato, M., R. Paolucci, T. Kouno, S. Nakatani, J. Fukui, R. Nova and C. Di Prisco (2008). "Numerical simulation of model tests of pier-shallow foundation systems subjected to earthquake loads using an elasto-uplift-plastic macro element." Soils and foundations **48**(5): 693-711.

Skau, K. S., Y. Chen and H. P. Jostad (2017). "A numerical study of capacity and stiffness of circular skirted foundations in clay subjected to combined static and cyclic general loading." Geotechnique:1-16.

Skau, K. S., G. Grimstad, A. M. Page, G. R. Eiksund and H. P. Jostad (2018). "A macro-element for integrated time domain analyses representing bucket foundations for offshore wind turbines." Marine Structures **59**: 158-178.

Sørensen, J. D. and J. N. Sørensen (2010). "Wind energy systems: Optimising design and construction for safe and reliable operation", Elsevier.

Soundararajan, K. K. (2015). "Multi-scale multiphase modelling of granular flows." Ph. D thesis, University of Cambridge.

Spence, D. (1968). "Self similar solutions to adhesive contact problems with incremental loading." Proc. R. Soc. Lond. A **305**(1480): 55-80.

Staron, L. and E. Hinch (2005). "Study of the collapse of granular columns using two-dimensional discrete-grain simulation." Journal of Fluid Mechanics **545**: 1-27.

Sukumaran, B., W. McCarron, P. Jeanjean and H. Abouseeda (1999). "Efficient finite element techniques for limit analysis of suction caissons under lateral loads." Computers and Geotechnics **24**(2): 89-107.

Taiebat, H. and J. Carter (2000). "Numerical studies of the bearing capacity of shallow foundations on cohesive soil subjected to combined loading." Géotechnique **50**(4): 409-418.

Tamagnini, C., D. Salciarini and R. Ragni (2013). "Implementation of 6–dof hypoplastic macroelement in a finite element code." Proceedings of third international symposium on computational geomechanics (ComGeo III), Springer, Berlin.

Tamagnini, C., G. Viggiani and R. Chambon (2000). "A review of two different approaches to hypoplasticity." Constitutive modelling of granular materials, Springer**:** 107-145.

Tan, F. S. C. (1990). "Centrifuge and theoretical modelling of conical footings on sand." Ph. D thesis, Cambridge Univ.

Tjelta, T.-l. (1994). "Geotechnical aspects of bucket foundations replacing piles for the Europipe 16/11-E jacket." Offshore Technology Conference, Houston, paper OTC 7379.

Tjelta, T. I. (1995). "Geotechnical experience from the installation of the Europipe jacket with bucket foundations." Offshore Technology Conference, Houston, paper OTC 7793.

Tjelta, T. I. (2001). "Suction piles: their position and application today." The Eleventh International Offshore and Polar Engineering Conference, International Society of Offshore and Polar Engineers.

Tjelta, T. I., T. R. Guttormsen and J. Hermstad (1986). "Large-scale penetration test at a deepwater site." Offshore Technology Conference, Houston, paper OTC 5103.

Tran, N. X. and S.-R. Kim (2017). "Evaluation of horizontal and moment bearing capacities of tripod bucket foundations in sand." Ocean Engineering **140**: 209-221.

Truty, A., K. Podleś, R. Obrzud, S. Commend and J. Sarf (2011). "ZSoil." PC 2011. User Manual.

Utili, S., T. Zhao and G. Houlsby (2015). "3D DEM investigation of granular column collapse: evaluation of debris motion and its destructive power." Engineering geology **186**: 3-16.

Villalobos, F., B. Byrne, G. Houlsby and C. Martin (2003). "Bearing capacity tests of scale suction caisson footings on sand: Experimental data." Data Rep. FOT005/1, Dept. of Engineering Science, Univ. of Oxford, Oxford, UK.

Villalobos, F. A., B. W. Byrne and G. T. Houlsby (2005). "Moment loading of caissons installed in saturated sand." Proceedings of international symposium on frontiers in Geotechnics, ISFOG. University of Western: 411-416.

Villalobos, F. A., B. W. Byrne and G. T. Houlsby (2009). "An experimental study of the drained capacity of suction caisson foundations under monotonic loading for offshore applications." Soils and foundations **49**(3): 477-488.

Villalobos, F. A., B. W. Byrne and G. T. Houlsby (2010). "Model testing of suction caissons in clay subjected to vertical loading." Applied Ocean Research **32**(4): 414-424.

Villalobos, F. A., G. T. Houlsby and B. W. Byrne (2004). "Suction caisson foundations for offshore wind turbines." Proc. 5th Chilean Conference of Geotechnics (Congreso Chileno de Geotecnia), Santiago.

Villalobos Jara, F. A. (2006). "Model testing of foundations for offshore wind turbines." Ph. D thesis, Oxford University.

Watson, P. and M. Randolph (1997). "Vertical capacity of caisson foundations in calcareous sediments." The Seventh International Offshore and Polar Engineering Conference, International Society of Offshore and Polar Engineers.

Watson, P. and M. Randolph (1998). "Failure envelopes for caisson foundations in calcareous sediments." Applied Ocean Research **20**(1-2): 83-94.

Watson, P., M. Randolph and M. Bransby (2000). "Combined lateral and vertical loading of caisson foundations." Offshore Technology Conference, Houston, paper OTC 12195.

Watson, P. G. (1999). "Performance of skirted foundations for offshore structures", Ph. D, thesis. University of Western Australia.

Wu, Y.-X., J. S. Shen, W.-C. Chen and T. Hino (2017). "Semi-analytical solution to pumping test data with barrier, wellbore storage, and partial penetration effects." Engineering Geology **226**: 44-51.

Wu, Y.-X., S.-L. Shen and D.-J. Yuan (2016). "Characteristics of dewatering induced drawdown curve under blocking effect of retaining wall in aquifer." Journal of Hydrology **539**: 554-566.

Wu, Z.-X., Z.-Y. Yin, Y.-F. Jin and X.-Y. Geng (2017). "A straightforward procedure of parameters determination for sand: a bridge from critical state based constitutive modelling to finite element analysis." European Journal of Environmental and Civil Engineering: 1-23.

Yao, Y., W. Hou and A. Zhou (2009). "UH model: three-dimensional unified hardening model for overconsolidated clays." Geotechnique **59**(5): 451-469.

Yao, Y., D. Lu, A. Zhou and B. Zou (2004). "Generalized non-linear strength theory and transformed stress space." Science in China Series E: Technological Sciences **47**(6): 691-709.

Yao, Y., D. Sun and H. Matsuoka (2008). "A unified constitutive model for both clay and sand with hardening parameter independent on stress path." Computers and Geotechnics **35**(2): 210-222.

Yin, Z.-Y., P.-Y. Hicher, C. Dano and Y.-F. Jin (2016). "Modeling mechanical behavior of very coarse granular materials." Journal of Engineering Mechanics **143**(1): C4016006.

Yin, Z.-Y., Y.-F. Jin, S.-L. Shen and H.-W. Huang (2016). "An efficient optimization method for identifying parameters of soft structured clay by an enhanced genetic algorithm and elastic–viscoplastic model." Acta Geotechnica: 1-19.

Yin, Z.-Y., Y.-F. Jin, S.-L. Shen and H.-W. Huang (2017). "An efficient optimization method for identifying parameters of soft structured clay by an enhanced genetic algorithm and elastic–viscoplastic model." Acta Geotechnica **12**: 849-867.

Yin, Z. Y., Y. F. Jin, J. S. Shen and P. Y. Hicher (2018). "Optimization techniques for identifying soil parameters in geotechnical engineering: Comparative study and enhancement." International Journal for Numerical and Analytical Methods in Geomechanics **42**(1): 70-94.

Yun, G. and M. Bransby (2003). "Centrifuge modeling of the horizontal capacity of skirted foundations on drained loose sand." BGA International Conference on Foundations: Innovations, observations, design and practice: Proceedings of the international conference organised by British Geotechnical Association and held in Dundee, Scotland on 2–5th September 2003, Thomas Telford Publishing.

Zafeirakos, A. and N. Gerolymos (2016). "Bearing strength surface for bridge caisson foundations in frictional soil under combined loading." Acta Geotechnica **11**(5): 1189-1208.

Zenit, R. (2005). "Computer simulations of the collapse of a granular column." Physics of Fluids **17**(3): 031703.

Zhang, J., D. Yan, G. Sun, W. Li and X. Lu (2003). "Development of a dynamic loading device for suction pile in centrifuge." BGA International Conference on Foundations: Innovations, observations, design and practice: Proceedings of the international conference organised by British Geotechnical Association and held in Dundee, Scotland on 2–5th September 2003, Thomas Telford Publishing.

Zhang, J. H., L. M. Zhang and X. B. Lu (2007). "Centrifuge modeling of suction bucket foundations for platforms under ice-sheet-induced cyclic lateral loadings." Ocean Engineering **34**: 1069-1079.

Zhang, P., H. Ding and C. Le (2013). "Installation and removal records of field trials for two mooring dolphin platforms with three suction caissons." Journal of waterway, port, coastal, and ocean engineering **139**(6): 502-517.

Zhang, Y., M. J. Cassidy and B. Bienen (2014). "A plasticity model for spudcan foundations in soft clay." Canadian Geotechnical Journal **51**(6): 629-646.

Zhu, B., B. W. Byrne and G. T. Houlsby (2013). "Long-Term Lateral Cyclic Response of Suction Caisson Foundations in Sand." Journal of Geotechnical and Geoenvironmental Engineering **139**: 73-83.

Zhu, B., W.-l. Zhang, P.-p. Ying and Y.-m. Chen (2014). "Deflection-Based Bearing Capacity of Suction Caisson Foundations of Offshore Wind Turbines." Journal of Geotechnical and Geoenvironmental Engineering **140**: 1-12.